Oxygen isotope study of the Asuka-881020 CH chondrite II: Porphyritic chondrules

Daisuke Nakashima[1,2,*], Takaaki Noguchi[3,4], Takayuki Ushikubo[2,5], Makoto Kimura[6,7],and Noriko Kita[2]

[1]Department of Earth Science, Tohoku University, Aoba, Sendai, Miyagi 980-8578, Japan

[2]Department of Geoscience, University of Wisconsin-Madison, Madison, WI 53706, USA

[3]Faculty of Arts and Science, Kyushu University, 744 Motooka, Nishi-ku, Fukuoka 819-0395, Japan

[4]Division of Earth and Planetary Sciences, Kyoto University, Kyoto 606-8502, Japan.

[5]Kochi Institute for Core Sample Research, JAMSTEC, Monobe-otsu 200, Nankoku, Kochi 783-8502, Japan

[6]Faculty of Science, Ibaraki University, Mito, Ibaraki, 310-8512, Japan

[7]National Institute of Polar Research, Tokyo 190-8518, Japan

*Corresponding author, Tel/Fax: +81-22-795-5903, Email: dnaka@tohoku.ac.jp

Submitted to Geochimica Cosmochimica et Acta

Keywords: CH chondrite, chondrules, oxygen isotopes

Abstract

Oxygen isotope ratios and elemental compositions of porphyritic chondrules and olivine and pyroxene fragments in the Asuka-881020 CH chondrite were analyzed. The oxygen isotope ratios inside individual porphyritic chondrules are homogeneous within the uncertainty, except for relict grains of olivine and low-Ca pyroxene that have distinct oxygen isotope ratios. The average oxygen isotope ratios of the individual chondrules plot along and above the primitive chondrule mineral (PCM) line with $\Delta^{17}O$ (= $\delta^{17}O - 0.52 \times \delta^{18}O$) values from –4.7‰ to +4.1‰. The olivine and pyroxene fragments, which have $\Delta^{17}O$ values ranging from –2.1‰ to +3.2‰, are likely to be fragments of the porphyritic chondrules.

Unlike the non-porphyritic chondrules in CH and CB chondrites and chondrules in other carbonaceous chondrites, the type I and II chondrules do not show a systematic difference in the $\Delta^{17}O$ values. Furthermore, the $\Delta^{17}O$ values of the type I chondrules increase from –4.7‰ to +4.1‰ with increasing Mg# (= molar [MgO]/[MgO+FeO]×100) from 96 to 99. We argue that the positive $\Delta^{17}O$-Mg# trend is explained by an addition of ^{16}O-poor carbon-rich organics as a reducing agent to the relatively ^{16}O-rich precursor silicate, which is a new environment for chondrule formation. This hypothesis is supported by the two lines of evidence observed in the present study. (1) The chondrules and fragments with higher $\Delta^{17}O$ values show larger deviations from the PCM line towards low $\delta^{18}O$, suggesting oxygen isotope mass fractionation between the chondrule melt and CO or CO_2. (2) Olivine phenocrysts in the chondrules with high $\Delta^{17}O$ values contain Ni-poor Fe-metal particles surrounded by silica-rich glass, which may be reduction products during the chondrule formation. Thus, it is suggested that the porphyritic chondrules in CH and CB chondrites have different origins from chondrules in any other chondrite types, even from the non-porphyritic chondrules in CH and CB chondrites.

1. Introduction

Chondrules are igneous spherules composed mainly of olivine, pyroxene, glass, and Fe-Ni metal and are observed in most chondritic meteorites (e.g., Gooding and Keil, 1981; Scott and Krot, 2003). Chondrules have formed by transient heating and rapid cooling (e.g., Jones et al., 2005), ~ 1 – 5 Myr after the oldest Ca-Al-rich inclusions (CAIs) (e.g., Kita et al., 2000; Kurahashi et al., 2008; Hutcheon et al., 2009; Villeneuve et al., 2009; Kita and Ushikubo, 2012; Ushikubo et al., 2013; Nagashima et al., 2014, 2017, 2018; Schrader et al., 2017; Hertwig et al., 2019a; Tenner et al., 2019; Siron et al., 2021, 2022; Fukuda et al., 2022; Piralla et al., 2023). Based on the textures, chondrules are classified into porphyritic and non-porphyritic types (Gooding and Keil, 1981). Porphyritic chondrules have been heated to near-liquidus temperatures, and nucleation sites resulting from incomplete melting of precursor materials persist: growth of crystals can occur on multiple nucleation sites as the chondrule cools. Non-porphyritic chondrules have been heated above the liquidus, and most nucleation sites have been destroyed during the melting interval (Jones, 2012). Based on the Mg# (= molar [MgO]/[MgO+FeO]×100), chondrules are classified into type I (FeO-poor; Mg# $\geq$ 90) and type II (FeO-rich; Mg# $<$ 90) (e.g., Jones et al., 2005). The Mg# of chondrules is controlled by the oxygen fugacity of the chondrule-forming environment (Ebel and Grossmann, 2000; Zanda et al., 1994), and type I chondrules formed under more reducing conditions than type II chondrules (e.g., Tenner et al., 2015; Hertwig et al., 2018), though precursor compositions of individual chondrules can also affect the Mg# of chondrules (Connolly et al., 1994). Since chondrule-like objects were observed in cometary samples such as particles returned from comet Wild 2 (Nakamura et al., 2008; Ogliore et al., 2012; Joswiak et al., 2014), it is considered that chondrules were widely distributed in the protoplanetary disk even in the Kuiper belt region. Thus, chondrules are essential for understanding of the material evolution in the early Solar System.

In-situ analyses of chondrules in Acfer 094 (ungrouped C3.0) using secondary ion mass

spectrometry (SIMS) revealed that oxygen isotope ratios of the chondrules are distributed along the slope ~ 1 line of $\delta^{17}O = (0.978 \pm 0.013) \times \delta^{18}O - (2.70 \pm 0.11)$ in the oxygen three-isotope diagram, which is called as the primitive chondrule mineral (PCM) line (Ushikubo et al., 2012). Oxygen isotope ratios of individual mineral phases in chondrules from pristine carbonaceous chondrites plot along and above the PCM line (Connolly and Huss, 2010; Russell et al., 2010; Rudraswami et al., 2011; Schrader et al., 2013, 2014, 2017; Tenner et al., 2013, 2015, 2017, 2018; Davidson et al., 2014; Chaumard et al., 2018, 2021; Hertwig et al., 2018, 2019a, 2019b; Marrocchi et al., 2018, 2019, 2021, 2022; Yamanobe et al., 2018; Ushikubo and Kimura, 2021; Fukuda et al., 2022; Zhang et al., 2022; Pinto et al., 2024). Since the PCM line represents the primary trend of the major oxygen isotope reservoirs (^{16}O-rich CAIs and ^{16}O-poor cosmic symplectites) in the protoplanetary disk, chondrules that plot around the PCM line originated from the reservoirs (Ushikubo et al., 2012). Recent high precision analyses of chondrules further revealed that there are two groups of chondrules among carbonaceous chondrites that plot slightly below and above the PCM line, some of which show correlation to nucleosynthetic anomalies of Cr and Ti (Williams et al., 2020; Zhang et al., 2022). The chondrules with Cr and Ti isotope anomalies may have come from formation regions of ordinary chondrite chondrules (Williams et al., 2020). On the other hand, Schneider et al. (2020) found no carbonaceous chondrite chondrules related to ordinary chondrite chondrules from the Cr-Ti-O isotope analyses.

Oxygen isotope ratios of the Acfer 094 chondrules are internally homogeneous, except for relict grains that have distinct oxygen isotope ratios (Ushikubo et al., 2012). The Acfer 094 chondrules show bimodal $\Delta^{17}O$ ($= \delta^{17}O - 0.52 \times \delta^{18}O$) values of ~ −5‰ and −2‰ that negatively correlate with the Mg# values of chondrule phenocrysts, suggesting the former presence of two separate isotope reservoirs with different redox states in the protoplanetary disk and that the homogeneous oxygen isotope ratios represent localized oxygen isotope reservoirs in the disk (Ushikubo et al., 2012). Other primitive carbonaceous chondrites also show similar systematic

trends between Mg# and $\Delta^{17}O$ values, though the detailed trends are specific to individual chondrite groups (Connolly and Huss, 2010; Russell et al., 2010; Rudraswami et al., 2011; Schrader et al., 2013, 2014, 2017; Tenner et al., 2013, 2015, 2017, 2018; Davidson et al., 2014; Chaumard et al., 2018, 2021; Hertwig et al., 2018, 2019a, 2019b; Marrocchi et al., 2018, 2019, 2021, 2022; Yamanobe et al., 2018; Ushikubo and Kimura, 2021; Fukuda et al., 2022; Pinto et al., 2024). Continuous negative $\Delta^{17}O$-Mg# trends have been observed from chondrules in CR chondrules that are explained by an addition of ^{16}O-poor water ice as an oxidant to the ^{16}O-rich anhydrous solid precursors (Tenner et al., 2015). An addition of ^{16}O-poor CI-like dust is also suggested, which is supported by the peculiar ^{54}Cr signature of CR chondrules (Marrocchi et al., 2022).

In metal-rich carbonaceous CH and CB chondrites, non-porphyritic chondrules such as cryptocrystalline (CC) and skeletal olivine (SO) chondrules dominate the chondrule inventory (≥ 80%), though with their huge size difference between CH chondrules and CB chondrules (0.02 – 0.09 mm and 0.5 – 5 mm; Scott and Krot, 2003). Nakashima et al. (2020) reported that $\Delta^{17}O$ values of the non-porphyritic chondrules negatively correlate with the Mg#, similar to chondrules in other carbonaceous chondrites. Porphyritic chondrules, which are minor in CH and CB chondrites (≤ 20%; Scott and Krot, 2003), have a variation in the $\Delta^{17}O$ values from ~ –4‰ to +4‰ (excluding internally heterogeneous chondrules containing relict minerals; Krot et al., 2010), though the relationship with Mg# has not been discussed.

Lithic fragments, which are olivine and pyroxene fragments and olivine-pyroxene-normative fragments, occur around chondrules and Fe-Ni metal in CH chondrites instead of fine-grained matrix in pristine chondrites (Scott, 1988; Grossman et al., 1988). Nakashima et al. (2020) suggested that the olivine-pyroxene-normative fragments are fragments of CC chondrules in CH chondrites based on the similarity in oxygen isotope ratios. The possibility that olivine and pyroxene fragments are fragments of the porphyritic chondrules in CH chondrites (Scott, 1988)

can also be tested based on the oxygen isotope ratios.

In this study, oxygen isotope ratios and elemental compositions of porphyritic chondrules and olivine and pyroxene fragments in the Asuka (A) -881020 CH chondrite (Noguchi et al., 2004; Nakamura et al., 2006) were analyzed to understand oxygen isotope reservoirs and redox conditions in the formation environments of the porphyritic chondrules. As a result, a unique Δ^{17}O-Mg# trend is observed for the type-I chondrules and FeO-poor fragments; the Δ^{17}O values positively correlate with Mg#. We propose that the unique trend is caused by an addition of ^{16}O-poor carbon-rich organics as a reducing agent to the ^{16}O-rich precursors. The hypothesis is tested based on the mineralogy and chemistry including observation with transmission electron microscopy of the porphyritic chondrules and olivine and pyroxene fragments.

2. Analytical procedures

2.1. Electron microscopy

We used a polished thin section of the A-881020 CH chondrite (51-1; National Institute of Polar Research). Chondrules and olivine and pyroxene fragments in the section were examined using a scanning electron microscope (SEM; Hitachi S3400) at the University of Wisconsin-Madison and a field emission SEM (FE-SEM; JEOL JSM7001F) at Tohoku University. Backscattered electron (BSE) images were obtained. Elemental compositions of the chondrules and olivine and pyroxene fragments were measured using electron probe microanalyzers (EPMAs) at Ibaraki University (JEOL JXA-733), at National Institute of Polar Research (NIPR; JEOL JXA-8200), and at the University of Wisconsin-Madison (CAMECA SX-51) equipped with wavelength-dispersive X-ray spectrometers (WDSs). At Ibaraki University, WDS quantitative chemical analyses of bulk chondrules were performed at 15 kV accelerating voltage and 6 nA beam current with a defocused beam of 5 - 40 μm. After correction by the Bence-Albee method, the chondrule data were recalculated by the method of Ikeda (1980) to reduce the polyphase effect. Quantitative

chemical analyses of olivine and pyroxene fragments and individual silicate phases in chondrules were performed with a focused beam (10 nA) at Ibaraki University, NIPR, and University of Wisconsin-Madison (other analytical settings are the same as those for bulk chondrule analyses). Natural and synthetic standards were chosen based on the compositions of the minerals being analyzed (e.g., Tenner et al., 2015). Detection limits of oxide concentrations are shown in the Supplementary Tables A1.

2.2. Raman spectroscopy

The structural nature of chondrule silica was determined by laser micro-Raman spectroscopy, using a JASCO NRS-3100 spectrometer at Kyushu University. A microscope was used to focus the excitation laser beam (532 nm). The acquisition time was 30 s. For each region analyzed a Raman spectrum was acquired in the spectral region of 240 to 1340 cm^{-1}. Raman spectra were also acquired on the regions where tiny vesicles are dispersed in olivine phenocrysts of chondrules for the identification of gaseous compounds that may be trapped in the vesicles. The spectral region is from 1200 to 2200 cm^{-1}. Other analytical conditions are the same as those for chondrule silica.

2.3. Oxygen isotope analyses

Oxygen isotope ratios of porphyritic chondrules and olivine and pyroxene fragments in A-881020 were analyzed with the CAMECA IMS-1280 ion microprobe at the WiscSIMS laboratory (Kita et al., 2009). For the oxygen three-isotope analyses, two sizes of focused Cs^+ primary beam (10 × 15 μm at the intensity of ~ 3 nA and 2 × 4 μm at ~ 30 pA) were applied. The analytical conditions and measurement procedures were similar to those in Kita et al. (2010) and Nakashima et al. (2011). The secondary $^{16}O^-$, $^{17}O^-$, and $^{18}O^-$ ions were detected simultaneously by Faraday cups (FC) or electron multipliers (EM) on the multicollection system; three FCs for $^{16}O^-$, $^{17}O^-$, and $^{18}O^-$ for 15 μm spot analyses and a FC for $^{16}O^-$ and two EMs for $^{17}O^-$, and $^{18}O^-$ for 4 μm spot

analyses. Intensities of $^{16}O^-$ were ~ 3 × 10^9 cps and ~ 2 × 10^7 cps with 15 μm and 4 μm primary beams, respectively. The baselines of the FCs were measured during the presputtering (100 s for 15 μm spots and 360 s for 4 μm spots) in respective analyses and used for data correction. The contribution of the tailing of $^{16}O^1H^-$ interference to $^{17}O^-$ signal was corrected by the method described in Heck et al. (2010), though the contribution was negligibly small (typically < 0.1‰).

One to six analyses were performed for individual chondrules and olivine and pyroxene fragments, bracketed by eight to nine analyses (four or five analyses before and after the unknown sample analyses) on the San Carlos olivine standard grain in a separated mount (Supplementary Table A2). The external reproducibility of the running standard was 0.19 – 0.54‰ for $\delta^{18}O$, 0.35 – 0.66‰ for $\delta^{17}O$, and 0.21 – 0.68‰ for $\Delta^{17}O$ for 15 μm spot analyses, and that for 4 μm spot analyses was 0.73 – 1.18‰ for $\delta^{18}O$, 0.97 – 1.82‰ for $\delta^{17}O$, and 1.09 – 2.04‰ for $\Delta^{17}O$ (2SD; standard deviation). The external reproducibility was assigned as analytical uncertainties of unknown samples (see Kita et al., 2009, 2010 for detailed explanations). We used two olivine (Fo_{100} and Fo_{60}), three low-Ca pyroxene (En_{97}, En_{90}, and En_{85}), diopside, plagioclase (An_{95}), quartz, and four glass (50.9 – 76.0 wt% SiO_2) standards (Valley and Kita, 2009; Kita et al., 2010) in the same sessions for correction of instrumental bias of olivine, pyroxene, plagioclase, silica, and glass (Supplementary Table A3).

Porphyritic chondrules and mineral fragments of olivine and pyroxene were selected for oxygen isotope analysis are located within the radius of 5 mm of the center of the 1-inch round thin section of A-881020 in the same manner as that for the non-porphyritic chondrules (Nakashima et al., 2020) to avoid instrumental mass fractionation due to the X-Y effect (Kita et al., 2009). In each porphyritic chondrule, 1 to 6 spot analyses were made. The 15 μm beam was used for olivine and low-Ca pyroxene phenocrysts larger than 15 μm, and the 4 μm beam was used for those smaller than 15 μm, high-Ca pyroxene, glass, plagioclase, and silica (Supplementary Fig. A1).

2.4. Sample sectioning using focused ion beam and transmitted electron microscopy

For the observation of Fe-particles smaller than 1 μm in olivine phenocrysts in chondrules using a transmitted electron microscope (TEM), thin sections (~ 180 nm) of olivine phenocrysts containing Fe-particles were cut out using a focused ion beam (FIB) on a JEOL JIB-4501 FIB-SEM at Kyushu University. A 30 kV Ga^+ ion beam set to 50 pA – 100 nA was used. The FIB marks of 1 μm × 1 μm were made at both ends of the FIB sectioning area by removing carbon coating on the sample surface (e.g., Nakashima et al., 2012), as the Fe-particles are tiny and hidden from view after deposition of a W-layer. NanoMill TEM specimen preparation system (Model 1050) was used for removing amorphous layers on the surfaces of the thin sections formed during FIB sectioning. Two settings of Ar^+ ion beam (900 V and 500 V; intensity of 35 pA) were used. The FIB sections with a thickness of ~ 80 nm were observed using JEOL JEM-3200FSK TEM equipped with the JED-2200 energy-dispersive X-ray spectrometer (EDS) at Kyushu University. The accelerating voltage was 300 kV. Quantitative analysis was performed using the Cliff-Lorimer correction with the TEM-EDS, and the element concentrations were corrected using k factors obtained by measuring mineral standards (Noguchi et al., 2015).

3. Results

Search for porphyritic chondrules and olivine and pyroxene fragments large enough for 15 μm and 4 μm spot SIMS analysis and electron microprobe and SIMS analyses were conducted along with those of the non-porphyritic chondrules and lithic fragments in the same meteorite in the same sessions (Nakashima et al., 2020). In Nakashima et al. (2020), the non-porphyritic chondrules and lithic fragments are numbered as C1 – C37 and F1 – F40. In the present paper, the porphyritic chondrules and olivine and pyroxene fragments are sequentially numbered as C38 – C59 (n = 22) and F41 – F61 (n = 21), respectively (Supplementary Table A1).

3.1. Petrology and mineralogy of porphyritic chondrules

Porphyritic chondrules in A-881020 are 50 – 380 μm in size (170 μm on average; Fig. 1; Supplementary Fig. A1) and smaller than (or as small as) those in other chondrite groups (Friedrich et al., 2014). The porphyritic chondrules consist mainly of olivine and low-Ca pyroxene phenocrysts, Fe-Ni metal, and glass. The porphyritic chondrules contain accessory phases of high-Ca pyroxene with Wo# from 21.5 to 43.5, pyroxene with intermediate compositions ($En_{78.1-93.7}Wo_{5.0-18.5}$), plagioclase with An# from 75.6 to 91.7, and silica (Supplementary Table A1). Pyroxene with intermediate compositions is called as intermediate pyroxene (Tenner et al., 2015). Nepheline or sodalite, a product of metasomatism (e.g., Kimura and Ikeda, 1995; Krot et al., 1998), is not observed in glass and plagioclase in the porphyritic chondrules. Electron microprobe analyses of glass and plagioclase show totals higher than 98 wt% (Supplementary Table A1), indicating no replacement by phyllosilicates.

Most of the porphyritic chondrules are porphyritic olivine (PO), porphyritic olivine-pyroxene (POP), and porphyritic pyroxene (PP) types. There are two chondrules with unique textures. C46 consists of a low-Ca pyroxene core surrounded by a glassy rim. C58 consists of an olivine core surrounded by a rim composed of low-Ca pyroxene, silica, and microcrystalline mesostasis (Supplementary Fig. A1). Silica in C58 is cristobalite, as the Raman spectra showed a peak around 420 cm^{-1}. Sub-μm sized Cr-spinel particles (detected by FE-SEM-EDS) occur between the olivine core and surrounding low-Ca pyroxene (Supplementary Fig. A1).

In each chondrule, olivine and low-Ca pyroxene compositions are homogeneous with small variations in Fo#, En#, and Wo# of less than 2.6, 2.1, and 1.8 (1SD). The averaged olivine Fo# range from 73.2 to 99.1, and averaged low-Ca pyroxene En# and Wo# range from 89.8 to 97.4, and from 0.5 to 4.2, respectively. The Fo# of 73.2 is from a PO chondrule (C59; Fig. 1j), which is a type II chondrule with no Fe-Mg zoning in olivine phenocrysts. Others are type I chondrules

with Mg# of olivine and low-Ca pyroxene phenocrysts higher than 91. Mg# of individual chondrules in Table 1 are average values of Mg# of olivine and low-Ca pyroxene in the chondrules.

3.2. Bulk elemental compositions of porphyritic chondrules

Bulk elemental compositions of porphyritic chondrules were obtained by broad-beam EPMA analyses, though they may not reflect true compositions of individual chondrules (Jones, 2005). Refractory element abundances in the porphyritic chondrules in A-881020 are systematically higher than those in CC chondrules in CH and CB chondrites (Krot et al., 2010; Nakashima et al., 2011, 2020) and as high as those in chondrules in other carbonaceous chondrites (Hezel and Palme, 2010) (Fig. 2).

3.3. Fe-particles and vesicles in olivine phenocrysts in porphyritic chondrules

Olivine phenocrysts in more than a half of porphyritic chondrules contain sub-μm sized Fe-particles (detected by FE-SEM-EDS) and vesicles, which are linearly aligned (Fig. 3; Supplementary Fig. A1). No Fe-Mg zoning is observed in the olivine phenocrysts. The Fe-particles and vesicles are also observed in plagioclase in the chondrule C47 (Fig. 3d). Raman spectra were obtained in the regions where the vesicles occur, but any peak suggesting the presence of gaseous species in vesicles is not observed. Instead, the observed Raman spectra are similar to those of epoxy (e.g., Hardis et al., 2013), which is underneath the thin section.

The BSE images show Fe-particles and vesicles distribute on the cut surface of the FIB sections (Figs. 4a, 4d), which were cut out along the aligned Fe-particles and vesicles from the olivine phenocrysts. Therefore, the Fe-particles and vesicles distribute on a plane almost perpendicular to the polished surface of the chondrule olivine phenocrysts. The HAADF-STEM images of the FIB section from the chondrule C40 (grid-1) show that the Fe-particles smaller than 0.5 μm are surrounded by silica-rich glass in the host olivine (Figs. 4b, 4c). Tiny Fe-particles

surrounded by silica-rich glass are also observed in dusty olivine (Leroux et al., 2003). In the FIB section from the chondrule C41 (grid-2), vesicles occur along with Fe-particles in the host olivine with dislocations (Fig. 4e). An electron diffraction pattern of the largest Fe-particle (~ 2 μm in size) in the grid-2 shows that it is a bcc Fe-metal, i.e., kamacite (Fig. 4f). The same may be true for other tiny Fe-particles. The Fe-particles are Ni-free or contain small concentrations of Ni (Table 3). The average Ni concentration is 2.5 ± 2.3 wt% (n = 7; 1σ). Silica-rich glass surrounding the Ni-poor Fe-metal particles shows similar elemental composition to those in the Bishunpur LL3.1 chondrite (Leroux et al., 2003) and contain CaO and Al_2O_3 of ~ 19 wt% and 24 wt% (Fig. 5; Table 4).

3.4. Petrology and mineralogy of olivine and pyroxene fragments

Lithic fragments that present in interstitial spaces between chondrules and Fe-Ni metal are olivine, low- and high-Ca pyroxene, and olivine-pyroxene-normative CC fragments (including silica-bearing fragments; Fig. 6; see also Nakashima et al., 2020). Except for the olivine-pyroxene-normative CC fragments, chemical compositions of the lithic fragments are close to stoichiometric olivine and low- and high-Ca pyroxene (Supplementary Table A1). Thirteen of the 21 olivine and pyroxene fragments are FeO-poor with Mg# of 90.7 – 99.3, and others are FeO-rich with Mg# of 50.5 – 80.0 (Table 2). FeO-rich olivine fragments do not show Fe-Mg zoning (Supplementary Fig. A1).

3.5. Oxygen isotope ratios

We made a total of 110 spot analyses in 22 porphyritic chondrules and 21 olivine and pyroxene fragments. After inspection of the SIMS analysis spots by SEM, one analysis was rejected because it overlapped with an adjacent lithic fragment (F55; Supplementary Fig. A1). A summary of the 109 spot analyses taken from 22 chondrules and 20 lithic fragments is shown in

Tables 1 – 2; a more complete table is given in the Supplementary Table A4.

3.5.1. Oxygen isotope ratios of porphyritic chondrules

Oxygen isotope ratios of individual spot analyses in the porphyritic chondrules are distributed along and above the PCM line (Ushikubo et al., 2012; Zhang et al., 2022) and the Carbonaceous Chondrite Anhydrous Mineral (CCAM) line (Clayton et al., 1977) (Figs. 1b, 1e, 1h, 1k; Supplementary Fig. A1). The individual chondrules are isotopically uniform within the uncertainty, except for four chondrules with isotopically distinct relict grains and one chondrule (C43) containing olivine phenocrysts with heterogeneous oxygen isotope ratios (Fig. 1; Supplementary Fig. A1). The homogeneous oxygen isotope ratios represent those of the final chondrule melt and are referred as "host" chondrule oxygen isotope ratios, and especially chondrule glass in pristine chondrites preserves the oxygen isotope ratios of the chondrule-forming melts (Ushikubo et al., 2012). The isotopically distinct relict grains, which are mostly olivine, survived the final chondrule formation event and do not reflect oxygen isotope ratios of the final chondrule melt (e.g., Ushikubo et al., 2012). In C43, any olivine phenocryst analyzed for oxygen isotopes is possibly relict.

The relict grains are defined as the grains of which $\Delta^{17}O$ values are different from the host $\Delta^{17}O$ values by more than 3SD of individual analyses in the chondrules (e.g., Ushikubo et al., 2012). The relict grains are excluded from the calculation of average oxygen isotope ratios of the individual chondrules. The oxygen isotope ratios in the individual chondrules were measured with two different beam settings, which have different uncertainties (Supplementary Table A2). Therefore, the error-weighted average oxygen isotope ratios of individual chondrules are calculated. The uncertainties of the average values in the individual chondrules were estimated from the 2 standard error (2SE) of chondrule analyses (2SD/$\sqrt{}$number of chondrule analyses), unless it is smaller than the 2SE of bracketing standard analyses (2SD/$\sqrt{}$number of chondrule analyses). The average oxygen isotope ratios of individual chondrules are distributed along and

above the PCM line with $\delta^{18}O$ values from –1.3‰ to +11‰ (Fig. 7a).

In the two chondrules (C41 and C44), isotopically distinct low-Ca pyroxene grains are observed (Supplementary Fig. A1). In C44, four spot data from olivine and low-Ca pyroxene have an average $\Delta^{17}O$ value of –6.4 ± 0.9‰ (2σ), and two spot data from glass and low-Ca pyroxene have an average $\Delta^{17}O$ value of –0.3 ± 1.2‰ (Figs. 1h and 1i; Table 1). Therefore, the host $\Delta^{17}O$ value of C44 is ~ –0.3‰, and olivine and low-Ca pyroxene with $\Delta^{17}O$ of ~ –6‰ are relict.

3.5.2. Oxygen isotope ratios of olivine and pyroxene fragments

Most of the olivine and pyroxene fragments were analyzed with a 15 μm beam (Fig. 6; Supplementary Fig. A1). The oxygen isotope ratios show a variation from –3.9‰ to +11.8‰ in $\delta^{18}O$ along and above the CCAM and PCM lines (Fig. 7b; Supplementary Fig. A1). The $\delta^{18}O$ ranges for the FeO-poor fragments and FeO-rich ones overlap each other; –3.9‰ to +9.9‰ and +3.8‰ to +11.9‰. There is no systematic difference in $\delta^{18}O$ ranges between FeO-poor olivine and pyroxene and between FeO-rich olivine and pyroxene.

4. Discussion

For carbonaceous chondrites, chondrules with lower Mg# tend to have higher $\Delta^{17}O$ values, which is attributed to an addition of ^{16}O-poor water ice as an oxidant to relatively ^{16}O-rich precursor dust (e.g., Ushikubo et al., 2012; Tenner et al., 2015) or an addition of ^{16}O-poor CI-like dust (Marrocchi et al., 2022). However, there appears to be no systematic difference in the $\Delta^{17}O$ values between type I and II chondrules in CH and CB chondrites (Krot et al., 2010). In the present study, oxygen isotope ratios of porphyritic chondrules from the A-881020 CH chondrites are obtained to see if there is a systematic trend between the $\Delta^{17}O$ values and Mg#. But, only one type II chondrule is available (C59; Mg# = 73.2). Instead, FeO-rich olivine and pyroxene fragments, which may be fragments of the type II porphyritic chondrules (e.g., Scott, 1988), are analyzed for

the oxygen isotope ratios. Before discussing the Δ^{17}O-Mg# relationship of the porphyritic chondrules, we test if the olivine and pyroxene fragments are fragments of the porphyritic chondrules based on the chemistry and oxygen isotope ratios.

4.1. Genetic link between the olivine and pyroxene fragments and porphyritic chondrules

Inter-chondrule spaces in CH chondrites are filled with lithic fragments, which comprise ~ 70 vol% (e.g., Scott, 1988; Scott and Krot, 2003). The remaining ~ 30 vol% is composed mostly of chondrules (5 vol%), Fe-Ni metal (20 vol%), and hydrous matrix lumps (5 vol%) (e.g., Scott, 1988). The lithic fragments are olivine, pyroxene, and olivine-pyroxene normative materials like CC chondrules (e.g., Scott, 1988). Nakashima et al. (2020) suggested that the CC-like lithic fragments are fragments of CC chondrules, based on their indistinguishable Δ^{17}O values and depletion in refractory elements such as Ca and Al (Fig. 2).

For the FeO-poor lithic fragments (Mg# of 90.7-99.3) with Δ^{17}O of –5.0‰ to +3.0‰ (Fig. 8a), there are two possible candidates for their origin, namely porphyritic or SO chondrules from CH and CB chondrites. The SO chondrules, which have FeO-poor compositions, contain pyroxene and olivine (e.g., Krot et al., 2007). The Δ^{17}O variation of the SO chondrules is very limited (–2.4 ± 1.3‰ on average; 2SD; Krot and Nagashima, 2017). On the other hand, the Δ^{17}O variation of the type I porphyritic chondrules (–4.7‰ to +4.1‰; Fig. 8a) is as large as those of the FeO-poor fragments. FeO-poor fragments analyzed for oxygen isotopes are larger than olivine and pyroxene in SO chondrules (Krot et al., 2007; Nakashima et al., 2020) and as large as those in the porphyritic chondrules (Figs. 1 and 6; Supplementary Fig. A1). For the FeO-rich fragments (Mg# of 50.5 – 80.0) with Δ^{17}O of –3.2‰ to +1.5‰ (Fig. 8a), there are two possible candidates for their origin, porphyritic or silica-bearing chondrules with immiscibility textures (SB-I chondrules; Mg# of 66.3 – 92.3; Nakashima et al., 2020) in CH and CB chondrites. The latter contains pyroxene but no olivine (e.g., Nakashima et al., 2020). The Δ^{17}O variation of the SB-I chondrules is very limited

(+1.5 ± 1.1‰ on average; Nakashima et al., 2020). On the other hand, the $\Delta^{17}O$ variation of the type II porphyritic chondrules (–2.1‰ to +2.7‰; Krot et al., 2010; Fig. 8a) is as large as those of the FeO-poor fragments. Thus, it is likely that the olivine and pyroxene fragments analyzed for oxygen isotopes are fragments of porphyritic chondrules, though there may be olivine and pyroxene fragments from SO chondrules and SB-I chondrules.

In conjunction with the suggestion that the CC-like lithic fragments are fragments of CC chondrules (Nakashima et al., 2020), it is considered that the silicate fraction that comprises 75 vol% of CH chondrites (excluding hydrous matrix lumps) is composed mostly of chondrules and their fragments. As suggested in Nakashima et al. (2020), fragmentation of chondrules may have occurred during the accretion to the parent body and/or brecciation on the surface of the parent body. Thus, the inter-chondrule spaces in CH chondrites are filled with chondrule fragments.

4.2. Comparison of the $\Delta^{17}O$-Mg# trends

Chondrules in carbonaceous chondrites are known to show a systematic increase of $\Delta^{17}O$ values with decreasing Mg# (Figs. 8b-d; Connolly and Huss, 2010; Krot et al., 2010; Russell et al., 2010; Ushikubo et al., 2012; Schrader et al., 2013, 2014, 2017; Tenner et al., 2013, 2015, 2017, 2018; Chaumard et al., 2018, 2021; Hertwig et al., 2018, 2019a, 2019b; Marrocchi et al., 2018, 2019, 2021, 2022; Yamanobe et al., 2018; Nakashima et al., 2020; Ushikubo and Kimura, 2021; Fukuda et al., 2022; Pinto et al., 2024). The $\Delta^{17}O$-Mg# trends have been explained by an addition of ^{16}O-poor water ice as an oxidant to the ^{16}O-rich anhydrous solid precursors (e.g., Tenner et al., 2015; Hertwig et al., 2018), an addition of ^{16}O-poor CI-like dust (Marrocchi et al., 2022), or isotopically heterogeneous vapor plume resulting from a high temperature mixing of the ^{16}O-rich and ^{16}O-poor reservoirs (Libourel et al., 2023). The $\Delta^{17}O$-Mg# trends are specific to the individual carbonaceous chondrite groups (Figs. 8b-d) and are briefly described below.

For CO3.0, CV3, CM (-related), Acfer 094, and Yamato-82094 (ungrouped C3.2) chondrites,

there is mainly a bimodal distribution of $\Delta^{17}O$ at ~ –5‰ and ~ –2‰ for chondrules with Mg# > 97 and < 97 (including type II chondrules Fig. 8c; Ushikubo et al., 2012; Tenner et al., 2013, 2017; Chaumard et al., 2018, 2021; Hertwig et al., 2018, 2019b; Marrocchi et al., 2018, 2019; Hertwig et al., 2019a; Fukuda et al., 2022; Pinto et al., 2024).

Type I chondrules in CR chondrites show a monotonic increase in $\Delta^{17}O$ from –6‰ to –1‰ with decreasing Mg# from 99.2 to ~96 (Fig. 8d; Tenner et al., 2015), whereas those of type II chondrules vary from –2‰ to +1‰ (Connolly and Huss, 2010; see also Schrader et al., 2013, 2014, 2017; Marrocchi et al., 2022; Pinto et al., 2024). The $\Delta^{17}O$-Mg# trend of chondrules and chondrule fragments in the Tagish Lake-type carbonaceous chondrites is similar to that of the CR chondrite chondrules, but differ in the limited number of type I chondrules with Mg# < 98 and $\Delta^{17}O$ ~ –2‰ (Russell et al., 2010; Yamanobe et al., 2018; Ushikubo and Kimura, 2021; Marrocchi et al., 2021).

For non-porphyritic chondrules and lithic fragments with various textures in CH and CB chondrites, the $\Delta^{17}O$ values increase from –21‰ to +5‰ with decreasing Mg# from 99 to 60 (Fig. 8b; Nakashima et al., 2020; Krot et al., 2001, 2010, 2012, 2021). The non-porphyritic chondrules and lithic fragments are classified into three groups based on the $\Delta^{17}O$ values and Mg#. The first group, which is composed of SO and CC chondrules and their fragments, has indistinguishable $\Delta^{17}O$ values with an average of –2.3 ± 0.7‰ (2SD) and Mg# ranging from 91.7 to 99.6 (Table 3 in Nakashima et al., 2020). The second group, which is composed of an Al-rich chondrule, CC chondrules ± silica ± FeNi metal, and CC chondrule fragments, has positive $\Delta^{17}O$ values with an average of +1.4 ± 1.2‰ and Mg# ranging from 58.5 to 95.4. The third group, which is composed of Al-rich and CC chondrules and silica-bearing chondrules, has $\Delta^{17}O$ values with an average of –6.3 ± 0.7‰ and Mg# ranging from 91.1 to 99.3. Nakashima et al. (2020) suggested that the non-porphyritic chondrules and lithic fragments require multiple chondrule-forming environments with different redox states generated by multiple heating events, though Krot et al. (2021) suggest that FeO-poor and -rich non-porphyritic chondrules formed in an impact plume under different redox

conditions.

Most chondrules from the non-carbonaceous chondrites (LL3, E3, G, Kakangari, and R3) show fairly constant $\Delta^{17}O$ values (~ –1‰ to ~ +2‰) regardless of Mg# (Fig. 8e; Kita et al., 2010, 2015; Weisberg et al., 2011, 2015, 2021; Nagashima et al., 2015; Piralla et al., 2021; Siron et al., 2021, 2022), though recently Marrocchi et al. (2024) showed that ordinary chondrite chondrules smaller than 300 μm in diameter have negative $\Delta^{17}O$ values down to ~ –10‰. The constant $\Delta^{17}O$ values with a range of Mg# are explained by chondrule formation from precursors without large variations in $\Delta^{17}O$ values and a small amount of water ice under environments with variable dust/gas ratios (up to 10,000 times solar; Kita et al., 2010).

Unlike the chondrules in other chondrites and non-porphyritic chondrules in CH and CB chondrites, the porphyritic chondrules and fragments in CH and CB chondrites show a different $\Delta^{17}O$-Mg# trend. Fig. 8a compiles Mg# and $\Delta^{17}O$ values of the porphyritic chondrules and olivine and pyroxene fragments in A-881020 and other CH and CB chondrites (Krot et al., 2010). For the type I porphyritic chondrules and their fragments with Mg# > 96, the $\Delta^{17}O$ values increase from –4.7‰ to +4.1‰ with increasing Mg#. For the chondrules and their fragments with Mg# < 96, the $\Delta^{17}O$ values increase up to +3.2‰. Similarly, type II chondrules in CR and Tagish Lake-type chondrites have high $\Delta^{17}O$ values up to +2‰ (Fig. 8d). Their low Mg# and relatively high $\Delta^{17}O$ values are explained by an addition of ^{16}O-poor water ice to the ^{16}O-rich anhydrous precursors (e.g., Tenner et al., 2015). Therefore, the porphyritic chondrules and their fragments Mg# < 96 may have formed in the same manner. However, the positive $\Delta^{17}O$-Mg# correlation for the porphyritic chondrules and fragments with Mg# > 96 cannot be explained within this framework and can also not be linked to the formation conditions of non-carbonaceous chondrites (Fig. 8e). Instead, the positive $\Delta^{17}O$-Mg# correlation requires a different formation environment. There are two possible explanations for the positive $\Delta^{17}O$-Mg# correlation. The case (1) is the addition of a ^{16}O-rich oxidizing agent to the ^{16}O-poor precursors, and the case (2) is the addition of a ^{16}O-poor

reducing agent to the ^{16}O-rich precursors. Hereafter, we discuss these two possible cases.

4.3. Case (1): addition of ^{16}O-rich oxidizing agent to the ^{16}O-poor precursors

For case (1), chondrules with Mg# of ~ 99 and Δ^{17}O of ~ +4‰, which are the higher end of the positive Δ^{17}O-Mg# correlation (Fig. 8a), may correspond to the ^{16}O-poor precursors. But such chondrule has not been observed in any other chondrites (Figs. 8b-e). On the other hand, water ice may correspond to the oxidizing agent, as is the case of chondrules in other carbonaceous chondrites (e.g., Tenner et al., 2015). Since the Δ^{17}O value at the lower end of the positive Δ^{17}O-Mg# correlation is ~ –4‰, water ice is required to have the Δ^{17}O value lower than –4‰. Nuth et al. (2012) suggested that ^{16}O-rich water ice can be produced by the Fischer-Tropsch reaction that converts CO into hydrocarbons by releasing the enriched ^{16}O back into the gas phase as water in the protoplanetary disk. However, water reaction products with ^{16}O-rich isotope ratios have not been found, while those with ^{16}O-poor isotope ratios have been observed; magnetite with Δ^{17}O of ~ +5‰ in ordinary chondrites (e.g., Choi et al., 1998) and cosmic symplectites with Δ^{17}O of ~ +80‰ in Acfer 094 (Sakamoto et al., 2007). Thus, the addition of ^{16}O-rich water ice to the ^{16}O-poor precursors is less likely as a cause of the positive Δ^{17}O-Mg# correlation (Fig. 8a).

4.4. Case (2): addition of ^{16}O-poor reducing agent to the ^{16}O-rich precursors

For case (2), chondrules with Mg# of ~ 96 and Δ^{17}O of ~ –4‰, which are the lower end of the positive Δ^{17}O-Mg# correlation (Fig. 8a), may correspond to the ^{16}O-rich precursors. Such chondrules are observed in Acfer 094 and CR chondrites (Ushikubo et al., 2012; Schrader et al., 2013). In the oxygen isotope mass balance model of Tenner et al. (2015), insoluble organic material (IOM) was included and considered to be an ^{16}O-poor reducing agent. In fact, Connolly et al. (1994) showed by heating experiments that forsteritic olivine with Fo_{99} could be produced from olivine with Fo_{94} and graphite or diamond, and Hashizume et al. (2011) showed IOM from a CR

chondrite had ^{16}O-poor isotope ratios ($\Delta^{17}O$ up to ~ +250‰).

What is envisioned during the heating of chondrule precursors along with carbon-rich organics are oxidation of carbon and reduction of chondrule melts. In the chondrule melts, carbon is oxidized and lost as CO or CO_2, which may result in mass-dependent oxygen isotope fractionation between the chondrules and oxidized carbon. Ash et al. (1998) reported that heating experiments of chondrule analogues with $\delta^{18}O$ of +6.5‰ and +7.5‰ and 5 wt% graphite produced reduced chondrule analogues with $\delta^{18}O$ of +5.6‰ and +6.3‰, indicating mass-dependent oxygen isotope fractionation of ~ 1‰ in $\delta^{18}O$ during reduction. Kita et al. (2010) calculated fractionation of $\delta^{18}O$ values between olivine plus pyroxene and CO. The difference in the $\delta^{18}O$ values of the two components ($\delta^{18}O_{Ol+Px} - \delta^{18}O_{CO}$) increase from ~ –2‰ to ~ –7‰ with decreasing temperature from 1900 °C to 800 °C. Likewise, lowered $\delta^{18}O$ values due to mass-dependent isotope fractionation are observed for the type I chondrules and FeO-poor fragments with high $\Delta^{17}O$ values of ~ +4‰ (Fig. 9). In Fig. 9, the deviation of $\delta^{18}O$ values from the PCM line ($\Delta^{18}O_{PCM}$) for the type I chondrules and their fragments in CH and CB chondrites are plotted along with the $\Delta^{17}O$ values. While many of the chondrules and the fragments have $\Delta^{18}O_{PCM}$ values distributing near the PCM line, those with high $\Delta^{17}O$ values have $\Delta^{18}O_{PCM}$ values deviated from the PCM line towards the low-$\delta^{18}O$ side exceeding the uncertainty. Similarly, chondrules with dusty olivine in CM chondrites show the $\delta^{18}O$ shifts from the PCM line (Schrader et al., 2020), which might also be due to mass-dependent oxygen isotope fractionation during reduction. Zhang et al. (2022) suggested that chondrules with oxygen isotope ratios plotting on or above the PCM line (i.e., negative $\Delta^{18}O_{PCM}$ values) are likely linked to ordinary chondrite-like materials. However, chondrules with negative $\Delta^{18}O_{PCM}$ values in CH and CB chondrites have higher $\Delta^{17}O$ values than the ordinary chondrite chondrules (Figs. 8 and 9) and are unlikely linked to ordinary chondrites. Thus, oxygen isotope ratios of the ^{16}O-poor chondrules and fragments are deviated from the PCM line towards low $\delta^{18}O$, which are likely to be the result of the mass-dependent oxygen isotope

fractionation between the chondrule melts and CO or CO_2. Estimation of $\delta^{18}O$ fractionation from the PCM line for the chondrules is described in the section 4.6.

During reduction of chondrule melts, metal-silicate segregation may have occurred. Chondrules with positive $\Delta^{17}O$ values contain Fe-particles in the olivine phenocrysts (Fig. 3), though abundances of the Fe-particles are lower than those in experimentally reduced olivine and dusty olivine in chondrules (e.g., Connolly et al., 1994; Leroux et al., 2003). TEM observations suggest that the Fe-particles are kamacite (Fig. 4f). The Ni concentrations in the Fe-particles are 2.5 ± 2.3 wt% on average, which are lower than those in isolated Fe-Ni metal grains in the inter-chondrule spaces of CH and CB chondrites (~ 4 – 14 wt%; e.g., Krot et al., 2002) and as low as those in Fe-particles embedded in olivine phenocrysts in chondrules from an ordinary chondrite (0.2 – 2.1 wt%; e.g., Leroux et al., 2003). It is therefore considered that the Fe-particles are Ni-poor Fe-metal. The Ni-poor Fe-metal (kamacite) is surrounded by silica-rich glass (Figs. 4b, 4c), of which occurrence is explained by reduction of FeO-bearing olivine according to the following reactions:

$$2(Mg,Fe)_2SiO_4 + C_{\text{ in organics}} = Mg_2SiO_4 + 2Fe_{\text{ in Ni-poor metal}} + SiO_{2\text{ in glass}} + CO_{2\text{ in gas}}$$

$$2(Mg,Fe)_2SiO_4 + 2C_{\text{ in organics}} = Mg_2SiO_4 + 2Fe_{\text{ in Ni-poor metal}} + SiO_{2\text{ in glass}} + 2CO_{\text{ in gas}}$$

Although it was expected that the CO or CO_2 was trapped in the vesicles, the Raman spectra on the regions with numerous vesicles showed no peak derived from CO or CO_2 vibration. Amounts of CO or CO_2 in vesicles might be too small to show the Raman peaks.

The high concentrations of CaO and Al_2O_3 in the silica-rich glass may be explained by a supply from the olivine phenocrysts (Table 4; Leroux et al., 2003). Unlike the grid-1 (Figs. 4b, 4c), silica-rich glass is not observed in the grid-2 though with vesicles and olivine dislocations (Fig. 4e), which is explained by short-circuit diffusion of silicon and oxygen through the dislocations

(Leroux et al., 2003).

The Fe-particle abundances in the olivine phenocrysts (Fig. 3; Supplementary Fig. A1) are lower than those in experimentally reduced olivine (Connolly et al., 1994; Leroux et al., 2003). Nevertheless, it is important that the hypothesis of an addition of carbon-rich organics as a ^{16}O-poor reducing agent can explain qualitatively multiple features observed in the porphyritic chondrules.

4.5. Approximate estimation of oxygen isotope ratios of the ^{16}O-poor organics

As discussed in the previous sections, the positive Δ^{17}O-Mg# correlation of the chondrules and fragments with Mg# > 96 in CH and CB chondrites (Fig. 8a) is likely to be explained by addition of ^{16}O-poor carbon-rich organics to the ^{16}O-rich precursors with Mg# of ~ 96 and Δ^{17}O of ~ –4‰. According to the mass balance model of Tenner et al. (2015), oxygen is also supplied from water ice with positive Δ^{17}O values and from ambient gas of solar composition with Δ^{17}O of –28.4‰. Water ice facilitates an increase of the Δ^{17}O values but serves as an oxidizing agent, and therefore the anhydrous precursor is preferable. The ambient gas facilitates reduction of the chondrule melt due to the high H/O ratio of ~ 2000 (Tenner et al., 2015) but suppresses an increase of the Δ^{17}O values, and therefore the low density of the ambient solar gas is preferable. In order to explain the positive Δ^{17}O-Mg# correlation, an ice-free environment with the thin ambient solar gas is required. Such a unique environment might be available in the regions with large disk heights where the gas density is low and gas temperature is high (exceeding H_2O sublimation temperature) compared to the midplane in the protoplanetary disk (e.g., Walsh et al., 2012). Chondrule formation at the large disk heights may be possible by, for instance, clumpy accretion (Boss and Graham, 1993) and magnetic winds (Salmeron and Ireland, 2012).

Assuming that the ^{16}O-poor Mg-rich chondrules with Mg# of ~ 99 and Δ^{17}O of ~ +4‰ formed from the anhydrous precursors composed of ^{16}O-rich silicate with Mg# of ~ 96 and Δ^{17}O of ~ –

4‰ and ^{16}O-poor carbon-rich organics, we briefly estimate the Δ^{17}O value of the organics based on the oxygen isotope mass balance model (Tenner et al., 2015) and results of reduction experiments of olivine (Connolly et al., 1994). Details of the estimation is described in the Supplementary text. When changing chondrule Mg# from 94 to 99, 5 – 10 wt% of carbon (graphite or diamond) may be required (Connolly et al., 1994), which corresponds to the organic fraction of 7 – 14 wt% assuming chondritic IOM with the elemental composition of ~ $C_{100}H_{75}O_{17.5}N_{3.5}S_{2.5}$ (Alexander et al., 2017). The organic fraction amounts to 6 – 11% of oxygen in the anhydrous precursors. The remaining fraction of 86 – 93 wt% is silicate, which amounts to 89 – 94% of oxygen in the anhydrous precursors. Using the fractions of oxygen from the two components, the equation (5) in Tenner et al. (2015), and the Δ^{17}O values of silicate (–4‰) and produced chondrules (+4‰), the Δ^{17}O values of organics are estimated as from ~ +90‰ to ~ +190‰ (Fig. 10a). The estimated Δ^{17}O values of organics are higher than those of IOM in CI and CM chondrites (0‰ to +10‰; Tartèse et al., 2018) but within the range of ^{16}O-poor IOM in a primitive CR chondrite (up to ~ +250‰; Hashizume et al., 2011) and therefore not impossibly high. The carbon fraction of 5 – 10 wt% from organics is higher than that from IOMs in carbonaceous chondrites (≲ 2 wt%; Alexander et al., 2017) and would be lower than that in cosmic dust such as ultracarbonaceous Antarctic micrometeorites (e.g., Dartois et al., 2013). Similar calculations with changing the elemental compositions of IOMs are carried out, and the Δ^{17}O values of organics are almost lower than the Δ^{17}O upper limit of the ^{16}O-poor IOM in a primitive CR chondrite (Hashizume et al., 2011) (Supplementary Figs. A3-4).

Without carbon-rich organics with high Δ^{17}O values like IOM in a primitive CR chondrite, the observed positive Δ^{17}O-Mg# correlation cannot be formed even if enrichment of carbon-rich organics occurred. If ^{16}O-poor IOM in a primitive CR chondrite (Hashizume et al., 2011) represents the oxygen isotopic compositions of carbon-rich organics in the outer and colder part of the protoplanetary disk, the occurrence of ^{16}O-poor Mg-rich porphyritic chondrules (Mg# ~ 99,

$\Delta^{17}O \sim +4‰$) in CH and CB chondrites suggests that these chondrules formed farther than where typical Mg-rich chondrules in carbonaceous chondrites formed.

4.6. Approximate estimation of $\delta^{18}O$ fractionation of the ^{16}O-poor chondrules

As discussed above, 7 – 14 wt% organics with $\Delta^{17}O$ of ~ +90‰ to +190‰ is required to form Mg-rich porphyritic chondrules with $\Delta^{17}O$ values of ~ +4‰ (Fig. 10a), which has $\Delta^{18}O_{PCM}$ values of ~ –4‰ as a result of mass-dependent oxygen isotope fractionation between chondrules and oxidized carbon (CO or CO_2) (Fig. 9). Here we estimate how much $\delta^{18}O$ fractionation from the PCM line occurs when adding ^{16}O-poor organics of 7 – 14 wt% (i.e., 5 – 10 wt% carbon) to ^{16}O-rich silicate.

Four assumptions are given for the estimation. (A) $\Delta^{18}O_{PCM}$ value before segregation between chondrules and oxidized carbon is 0‰. (B) $\delta^{18}O$ fractionation between chondrules and oxidized carbon (gas) ($\delta^{18}O_{Chd} - \delta^{18}O_{Gas}$) is –4‰. (C) Carriers of oxygen in chondrules are olivine and pyroxene. (D) 50% of oxygen in chondrules resides in olivine (i.e., 50% oxygen in pyroxene). As for the assumption (B), the $\delta^{18}O$ fractionation of –4‰ corresponds to that at temperatures of 1100 – 1200 °C (Kita et al., 2010). As for the assumption (C), reduced partition functions of olivine and pyroxene as well as CO are given in Kita et al. (2010) (Supplementary Table A5). Reduced partition functions of CO_2 are also calculated using the β factors in Richet et al. (1977) and procedure in Kita et al. (2010), so that $\delta^{18}O_{Chd} - \delta^{18}O_{CO}$ and $\delta^{18}O_{Chd} - \delta^{18}O_{CO2}$ are estimated. Details of assumptions and calculations are described in the Supplementary text.

With increasing the amount of ^{16}O-poor organics added to ^{16}O-rich silicate, the C/O atomic ratio increases (Fig. 10a). The C/O ratio is 0.24 – 0.49 in the range of 7 – 14 wt% organics (5 – 10 wt% carbon). Carbon combines with oxygen in chondrule melts and form CO and/or CO_2, which is isolated from chondrules or remains in vesicles. Fig. 10b estimates atomic ratios of remaining oxygen in chondrules to magnesium with variable C/O ratios in cases of CO and CO_2. In case of

oxygen loss by CO, the remaining-O/Mg ratios in the C/O range of 0.24 – 0.49 are within the range of O/Mg ratios of the bulk porphyritic chondrules in A-881020 obtained by defocused EPMA analyses. This indicates that ^{16}O-poor Mg-rich chondrules can be formed by adding ^{16}O-poor organics of 7 – 14 wt%. However, the remaining-O/Mg ratios in the C/O range of 0.24 – 0.49 are below the O/Mg range of the bulk porphyritic chondrules in case of oxygen loss by CO_2, which means chondrules may not be formed.

Oxygen isotope fractionation between chondrules and CO is shown in Fig. 10c, in which $\delta^{18}O_{Chd} - \delta^{18}O_{CO}$ is constantly –4‰ based on the assumption (B). With increasing C/O ratio, amount of oxygen residing in chondrules decreases and that in CO increases. Therefore, the $\Delta^{18}O_{Chd\text{-}CO}$ value shifts in a negative direction from 0‰ and $\Delta^{18}O_{CO\text{-}Chd}$ value shifts towards 0‰ with increasing C/O ratio. The $\Delta^{18}O_{Chd\text{-}CO}$ values in the C/O range of 0.24 – 0.49 are ~ –1‰ to ~ –2‰, which is smaller than the observed $\Delta^{18}O_{PCM}$ values of ~ –4‰ (Fig. 9). In case of fractionation between chondrules and CO_2, the slopes are steeper than those in case of CO (Fig. 10c). Even with the same C/O ratio, amount of oxygen residing in CO_2 is twice larger than that in CO, and amount of oxygen residing in chondrules is lower. The shift of $\Delta^{18}O_{Chd\text{-}CO2}$ is about twice larger than that in case of CO. The $\Delta^{18}O_{Chd\text{-}CO2}$ values in the C/O range of 0.24 – 0.49 are ~ –2‰ to ~ –4‰. The lower end is comparable to the observed $\Delta^{18}O_{PCM}$ values (Fig. 9). However, chondrules may not be formed due to the low remaining-O/Mg ratios (Fig. 10b). Thus, ^{16}O-poor Mg-rich chondrules with negative $\Delta^{18}O_{PCM}$ values can be formed by oxygen isotope fractionation with CO, though the $\Delta^{18}O_{Chd\text{-}CO}$ values are smaller than the observed $\Delta^{18}O_{PCM}$ values (Fig. 9). Additional fractionation could be caused by kinetic fractionation during chondrule formation (e.g., Richter, 2004). Similar results are obtained with changing the elemental compositions of IOMs (Supplementary Figs. A3-4).

In summary, the porphyritic chondrules in CH and CB chondrites are characterized by smaller sizes (Fig. 1) than those in other chondrite chondrules and similar bulk chemistry (Fig. 2) and

textures to those in other chondrite chondrules. In terms of oxygen isotope systematics, the Mg-rich porphyritic chondrules in CH and CB chondrites require a unique formation environment. The Mg-rich porphyritic chondrules formed from anhydrous precursors composed of ^{16}O-rich silicate and ^{16}O-poor carbon-rich organics in the regions with large disk heights where the gas density is low and gas temperature is high. This is a new environment for chondrule formation and cannot be applicable to chondrules in other chondrites and even to non-porphyritic chondrules in CH and CB chondrites, as the chondrules show negative Δ^{17}O-Mg# trends (Fig. 8). Thus, CH and CB chondrites sampled chondrules that formed in entirely different formation environments.

4.7. Non-porphyritic chondrules and lithic fragments that may have formed along with the porphyritic chondrules

In CH and CB chondrites, there are non-porphyritic chondrules and lithic fragments that are not classified into the three groups in Δ^{17}O values (+1.4‰, –2.3‰, and –6.3‰), and Nakashima et al. (2020) suggested that several of the ungrouped objects formed along with the porphyritic chondrules. The magnesian CC chondrule (Ch01; Nakashima et al., 2011) has the Δ^{17}O value of +2.2 ± 0.1‰, Mg# of 98.7 (Fig. 8a), and the negative $\Delta^{18}O_{PCM}$ value (Fig. 9). The silica-bearing lithic fragment (F37; Nakashima et al., 2020) has the Δ^{17}O value of –3.4 ± 0.2‰, Mg# of 95.1, and the $\Delta^{18}O_{PCM}$ value close to 0‰ (Figs. 8a and 9). Therefore, it is likely that the two FeO-poor objects formed along with the type I porphyritic chondrules in the same event. The FeO-rich radial pyroxene chondrule (C32; Nakashima et al., 2020) has the Δ^{17}O value of –1.1 ± 0.3‰, which is within the Δ^{17}O range of type II chondrules and FeO-rich fragments (Fig. 8a). On the other hand, two FeO-rich silica-bearing lithic fragments (F38 and F39; Nakashima et al., 2020) have the Δ^{17}O values outside of the Δ^{17}O range of type II chondrules and FeO-rich fragments (Fig. 8a). Therefore, it is likely that the FeO-rich radial pyroxene chondrule formed along with type II porphyritic chondrules, but the two FeO-rich silica-bearing lithic fragments may have formed in distinct

environments.

5. Conclusions

We analyzed oxygen isotope ratios and elemental compositions of porphyritic chondrules and olivine and pyroxene fragments in the A-881020 CH chondrite to investigate the oxygen isotope systematics of the porphyritic chondrules in CH and CB chondrites. The oxygen isotope ratios are homogeneous within the uncertainty inside the porphyritic chondrules, except for relict grains of olivine and low-Ca pyroxene with distinct oxygen isotope ratios. The average oxygen isotope ratios of the individual chondrules plot along and above the PCM line with $\Delta^{17}O$ values from –4.7‰ to +4.1‰. The olivine and pyroxene fragments, of which $\Delta^{17}O$ values range from –2.1‰ to +3.2‰, are likely to be fragments of the porphyritic chondrules.

Type I and II chondrules including FeO-poor and -rich fragments do not show a systematic difference in the $\Delta^{17}O$ values, unlike the non-porphyritic chondrules in CH and CB chondrites and chondrules in other carbonaceous chondrites. For the chondrules and their fragments with Mg# < 96, the $\Delta^{17}O$ values increase with decreasing Mg#, similarly to the type II chondrules in CR and Tagish Lake-type chondrites. The type II chondrules in CH and CB chondrites may have formed in a similar environment to that for type II chondrules in CR and Tagish Lake-type chondrites (e.g., Tenner et al., 2015). The $\Delta^{17}O$ values of the type I chondrules and fragments increase from –4.7‰ to +4.1‰ with increasing Mg# from 96 to 99. The positive $\Delta^{17}O$-Mg# correlation may be explained by an addition of ^{16}O-poor organics as a reducing agent to the relatively ^{16}O-rich silicate in the regions with large disk heights where the gas density is low and gas temperature is high. This is a new environment for chondrule formation. This hypothesis is supported by the two lines of evidence. (1) Oxygen isotope ratios of the ^{16}O-poor chondrules and fragments deviate from the PCM line towards low $\delta^{18}O$, while those of the relatively ^{16}O-rich chondrules and fragments are distributed around the PCM line. The $\delta^{18}O$ deviations are likely to be the result of the oxygen

isotope mass fractionation between the chondrules and CO or CO_2. (2) The porphyritic chondrules contain Ni-poor Fe-metal particles surrounded by silica-rich glass in the olivine phenocrysts, which are likely to be reduction products during the chondrule formation. Thus, the Mg-rich porphyritic chondrules in CH and CB chondrites may have formed in the different formation environment from any other chondrite chondrules including non-porphyritic chondrules in CH and CB chondrites.

Data Availability

Data are available through Mendeley Data at https://doi.org/10.17632/4bpgnwmxh5.1.

Acknowledgements

The authors thank NIPR for use of A-881020 thin section for this study, J. Kern and T. J. Tenner for SIMS support, J. Fournelle for EPMA support at UW-Madison, and Sasha Krot for kindly providing oxygen isotope data of SO chondrules in metal-rich carbonaceous chondrites. K. Yamada helped to conduct EPMA analyses at Ibaraki University. A. Yamaguchi helped to conduct EPMA analyses at NIPR. Reviews of E. van Kooten and two anonymous reviewers significantly improved the manuscript. This work was supported by JSPS KAKENHI grant number 18H01263 (D.N.) and the NASA Cosmochemistry program (NNX11AG62G). WiscSIMS is partly supported by NSF (EAR10-53466, EAR-1658823).

Appendix A. Supplementary material

This supplementary material consists of an excel file and two PDF files. The excel file contains table A1 (elemental compositions of porphyritic chondrules and olivine and pyroxene fragments), table A2 (raw SIMS measured oxygen isotope data), table A3 (instrumental bias of SIMS analysis), and table A4 (oxygen isotope ratios and Mg# of individual spots in porphyritic chondrules). One of the two PDF files contains figure A1 (oxygen isotope ratios of individual spots

in porphyritic chondrules and BSE images of porphyritic chondrules and olivine and pyroxene fragments). Another PDF file contains a text describing details of estimations of $\Delta^{17}O$ values in organics and $\delta^{18}O$ fractionation of ^{16}O-poor chondrules, table A5 (oxygen isotope fractionation between chondrules and CO_2 and CO), figure A2 (comparison of $\delta^{18}O$ values between olivine, low-Ca pyroxene, and glass in the same chondrules), figure A3 ($\Delta^{17}O$ values of organics, remaining-O/Mg ratios, and $\Delta^{18}O_{PCM}$ values of chondrules in case of Orgueil IOM), and figure A4 ($\Delta^{17}O$ values of organics, remaining-O/Mg ratios, and $\Delta^{18}O_{PCM}$ values of chondrules in case of CHON particles).

References

Alexander C. M. O'D., Cody G. D., De Gregorio B. T., Nittler L. R., and Stroud R. M. (2017) The nature, origin and modification of insoluble organic matter in chondrites, the major source of Earth's C and N. *Chem. Erde* **77**, 227–256.

Anders E. and Gerevesse N. (1989) Abundances of the elements: Meteoritic and solar. *Geochim. Cosmochim. Acta* **53**, 197–214.

Ash R. D., Connolly, Jr., H. C., Alexander C. M. O'D., MacPherson G. J., and Rumble, III, D. (1998) Oxygen isotope ratios of natural and synthetic chondrules: evidence for in situ reduction by carbon. *Meteorit. Planet. Sci.* **33**(Suppl.), A11 (abstr.).

Boss A. P. and Graham J. A. (1993) Clumpy disk accretion and chondrule formation. *Icarus* **106**, 168-178.

Chaumard N., Defouilloy C., and Kita N. T. (2018) Oxygen isotope systematics of chondrules in the Murchison CM2 chondrite and implications for the CO–CM relationship. *Geochim. Cosmochim. Acta* **228**, 220–242.

Chaumard N., Defouilloy C., Hertwig A. T., and Kita N. T. (2021) Oxygen isotope systematics of chondrules in the Paris CM2 chondrite: Indication for a single large formation region across

snow line. *Geochim. Cosmochim. Acta* **299**, 199–218.

Choi B. G., McKeegan K. D., Leshin L. A., and Wasson J. T. (1998) Extreme oxygen-isotope compositions in magnetite from unequilibrated ordinary chondrites. *Nature* **392**, 577–579.

Clayton R. N., Onuma N., Grossman L., and Mayeda T. K. (1977) Distribution of the pre-solar component in Allende and other carbonaceous chondrites. *Earth Planet. Sci. Lett.* **34**, 209–224.

Connolly, Jr., H. C. and Huss G. R. (2010) Compositional evolution of the protoplanetary disk: Oxygen isotopes of type-II chondrules from CR2 chondrites. *Geochim. Cosmochim. Acta* **74**, 2473–2483.

Connolly, Jr., H. C., Hewins R. H., Ash R. D., Zanda B., Lofgren G. E., and Bourot-Denise M. (1994) Carbon and the formation of reduced chondrules. *Nature* **371**, 136-139.

Dartois E., Engrand C., Brunetto R., Duprat J., Pino T., Quirico E., Remusat L., Bardin N., Briani G., Mostefaoui S., Morinaud G., Crane B., Szwec N., Delauche L., Jamme F., Sandt Ch., and Dumas P. (2013) UltraCarbonaceous Antarctic micrometeorites, probing the Solar System beyond the nitrogen snow-line. *Icarus* **224**, 243-252.

Davidson J., Krot A. N., Nagashima K., Hellebrand E., and Lauretta D. S. (2014) Oxygen isotope and chemical compositions of magnetite and olivine in the anomalous CK3 Watson 002 and ungrouped Asuka-881595 carbonaceous chondrites: Effects of parent body metamorphism. *Meteorit. Planet. Sci.* **49**, 1456–1474.

Ebel D. S. and Grossman L. (2000) Condensation in dust-enriched systems. *Geochim. Cosmochim. Acta* **64**, 339–366.

Friedrich J.M., Weisberg M. K., Ebel D. S., Biltz A. E., Corbett B. M., Iotzov I. V., Khan W. S., and Wolman M. D. (2014) Chondrule size and related physical properties: A compilation and evaluation of current data across all meteorite groups. *Chem. Erde* **75**, 419–443.

Fukuda K., Tenner T. J., Kimura M., Tomioka N., Siron G., Ushikubo T., Chaumard N., Hertwig A. T., and Kita N. T. (2022) A temporal shift of chondrule generation from the inner to outer

Solar System inferred from oxygen isotopes and Al-Mg chronology of chondrules from primitive CM and CO chondrites. *Geochim. Cosmochim. Acta* **322**, 194–229.

Gardinier A., Derenne S., Robert F., Behar F., Largeau C., and Maquet, J. (2000) Solid state CP/MAS ^{13}C NMR of the insoluble matter of the Orgueil and Murchison meteorites: quantitative study. *Earth Planet. Sci. Lett.* **184**, 9–21.

Gooding J. L. and Keil K. (1981) Relative abundances of chondrule primary textural types in ordinary chondrites and their bearing on conditions of chondrule formation. *Meteoritics* **16**, 17–42.

Grossman J. N., Rubin A. E., and MacPherson G. J. (1988) ALH85085: a unique volatile-poor carbonaceous chondrite with possible implications for nebular fractionation processes. *Earth Planet. Sci. Lett.* **91**, 33–54.

Hardis R., Jessop J. L. P., Peters F. E., and Kessler R. (2013) Cure kinetics characterization and monitoring of an epoxy resin using DSC, Raman spectroscopy, and DEA. *Compos. Part A* **49**, 100-108.

Hashizume K., Takahata N., Naraoka H., and Sano Y. (2011) Extreme oxygen isotope anomaly with a solar origin detected in meteoritic organics. *Nat. Geosci.* **4**, 165–168.

Heck P. R., Ushikubo T., Schmitz B., Kita N. T., Spicuzza M. J., and Valley J. W. (2010) A single asteroidal source for extraterrestrial Ordovician chromite grains from Sweden and China: High-precision oxygen three-isotope SIMS analysis. *Geochim. Cosmochim. Acta* **74**, 497–509.

Hertwig A. T., Defouilloy C., and Kita N. T. (2018) Formation of chondrules in a moderately high dust enriched disk: Evidence from oxygen isotopes of chondrules from the Kaba CV3 chondrite. *Geochim. Cosmochim. Acta* **224**, 116–131.

Hertwig A. T., Kimura M., Ushikubo T., Defouilloy C., and Kita N. T. (2019a) The ^{26}Al-^{26}Mg systematics of FeO-rich chondrules from Acfer 094: two chondrule generations distinct in age and oxygen isotope ratios. *Geochim. Cosmochim. Acta* **253**, 111–126.

Hertwig A. T., Kimura M., Defouilloy C., and Kita N. T. (2019b) Oxygen isotope systematics of chondrule olivine, pyroxene, and plagioclase in one of the most pristine $CV3_{Red}$ chondrites (Northwest Africa 8613). *Metorit. Planet. Sci.* **54**, 2666–2685.

Hezel D. C. and Palme H. (2010) The chemical relationship between chondrules and matrix and the chondrule matrix complementarity. *Earth Planet. Sci. Lett.* **294**, 85–93.

Hutcheon I. D., Marhas K. K., Krot A. N., Goswami J. N., and Jones R. H. (2009) ^{26}Al in plagioclase-rich chondrules in carbonaceous chondrites: evidence for an extended duration of chondrule formation. *Geochim. Cosmochim. Acta* **73**, 5080–5099.

Ikeda Y. (1980) Petrology of Allan Hills-764 chondrite (LL3). *Mem. Natl. Inst. Polar Res. Spec.* **17**, 50-82.

Jones R. H., Grossman J. N., and Rubin A. E. (2005) Chemical, mineralogical and isotopic properties of chondrules: Clues to their origin. In *Chondrules and the Protoplanetary Disk* (eds. A. N. Krot, E. R. D. Scott, and B. Reipurth). ASP Conference Series 341, Astronomical Society of the Pacific, San Francisco. pp. 251–285.

Jones R. H. (2012) Petrographic constraints on the diversity of chondrule reservoirs in the protoplanetary disk. *Meteorit. Planet. Sci.* **47**, 1176–1190.

Joswiak D. J., Nakashima D., Brownlee D. E., Matrajt G., Ushikubo T., Kita N. T., Messenger S., and Ito M. (2014) Terminal particle from Stardust track 130: Probable Al-rich chondrule fragment from comet Wild 2. *Geochim. Cosmochim. Acta* **144**, 277–298.

Kimura M. and Ikeda Y. (1995) Anhydrous alteration of Allende chondrules in the solar nebula II: Alkali-Ca exchange reactions and formation of nepheline, sodalite and Ca-rich phases in chondrules. *Proc. NIPR Symp. Antarc. Meteorites* **8**, 123-138.

Kissel J. and Krueger F. R. (1987) The organic component in dust from comet Halley as measured by the PUMA mass spectrometer on board Vega 1. *Nature* **326**, 755–760.

Kita N. T., Nagahara H., Togashi S., and Morishita Y. (2000) A short duration of chondrule

formation in the solar nebula: Evidence from ^{26}Al in Semarkona ferromagnesian chondrules. *Geochim. Cosmochim. Acta* **64**, 3913–3922.

Kita N. T., Ushikubo T., Fu B., and Valley J. W. (2009) High precision SIMS oxygen isotope analysis and the effect of sample topography. *Chem. Geol.* **264**, 43–57.

Kita N. T., Nagahara H., Tachibana S., Tomomura S., Spicuzza M. J., Fournelle J. H., and Valley J. W. (2010) High precision SIMS oxygen three isotope study of chondrules in LL3 chondrites: Role of ambient gas during chondrule formation. *Geochim. Cosmochim. Acta* **74**, 6610–6635.

Kita N. T. and Ushikubo T. (2012) Evolution of protoplanetary disk inferred from ^{26}Al chronology of individual chondrules. *Meteorit. Planet. Sci.* **47**, 1108–1119.

Kita N. T., Tenner T. J., Defouilloy C., Nakashima D., Ushikubo T., and Bischoff A. (2015) Oxygen isotope systematics of chondrules in R3 clasts: a genetic link to ordinary chondrites. *Lunar Planet. Sci. Conf.* **46**, 2053.

Krot A. N., Petaev M. I., Scott E. R. D., Choi B.-G., Zolensky M. E., and Keil K. (1998) Progressive alteration in CV3 chondrites: more evidence for asteroidal alteration. *Meteorit. Planet. Sci.* **33**, 1065–1085.

Krot A. N., McKeegan K. D., Russell S. S., Meibom A., Weisberg M. K., Zipfel J., Krot T. V., Fagan T. J., and Keil K. (2001) Refractory Ca, Al-rich inclusions and Al-diopside-rich chondrules in the metal-rich chondrites Hammadah al Hamra 237 and QUE 94411. *Meteorit. Planet. Sci.* **36**, 1189–1217.

Krot A. N., Meibom A., Weisberg M. K., and Keil K. (2002) The CR chondrite clan: Implications for early solar system processes. *Meteorit. Planet. Sci.* **37**, 1451–1490.

Krot A. N., Ivanova M. A., and Ulyanov A. A. (2007) Chondrules in the CB/CH-like carbonaceous chondrite Isheyevo: Evidence for various chondrule-forming mechanisms and multiple chondrule generations. *Chem. Erde* **67**, 283–300.

Krot A. N., Nagashima K., Yoshitake M., and Yurimoto H. (2010) Oxygen isotopic compositions

of chondrules from the metal-rich chondrites Isheyevo (CH/CB_b), MAC 02675 (CB_b) and QUE 94627 (CB_b). *Geochim. Cosmochim. Acta* **74**, 2190–2211.

Krot A. N., Nagashima K., and Petaev M. I. (2012) Isotopically uniform, ^{16}O-depleted calcium, aluminum-rich inclusions in CH and CB carbonaceous chondrites. *Geochim. Cosmochim. Acta* **83**, 159–178.

Krot A. N. and Nagashima K. (2017) Constraints on mechanisms of chondrule formation from chondrule precursors and chronology of transient heating events in the protoplanetary disk. *Geochem. J.* **51**, 45–68.

Krot A. N., Petaev M. I., Nagashima K., Dobrică E., Johnson B. C., and Cashion M. D. (2021) Impact plume-formed and protoplanetary disk high-temperature components in CB and CH metal-rich carbonaceous chondrites. *Meteorit. Planet. Sci.* **57**, 352–380.

Kurahashi E., Kita N. T., Nagahara H., and Morishita Y. (2008) ^{26}Al–^{26}Mg systematics of chondrules in a primitive CO chondrite. *Geochim. Cosmochim. Acta* **72**, 3865–3882.

Leroux H., Libourel G., Lemelle L., and Guyot F. (2003) Experimental study and TEM characterization of dusty olivines in chondrites: Evidence for formation by in situ reduction. *Meteorit. Planet. Sci.* **38**, 81–94.

Libourel G., Nagashima K., Portail M., and Krot A. N. (2023) On the significance of oxygen-isotope variations in chondrules from carbonaceous chondrites. *Geochim. Cosmochim. Acta* **346**, 102–120.

Marrocchi Y., Villeneuve J., Batanova V., Piani L., and Jacquet E. (2018) Oxygen isotopic diversity of chondrule precursors and the nebular origin of chondrules. *Earth Planet. Sci. Lett.* **496**, 132–141.

Marrocchi Y., Euverte R., Villeneuve J., Batanova V., Welsch B., Ferrière L., and Jacquet E. (2019) Formation of CV chondrules by recycling of amoeboid olivine aggregate-like precursors. *Geochim. Cosmochim. Acta* **247**, 121–141.

Marrocchi Y., Avice G., and Barrat J.-A. (2021) The Tarda meteorite: a window into the formation of D-type asteroids. *Astrophys. J.* **913**, L9.

Marrocchi Y., Piralla M., Regnault M., Batanova V., Villeneuve J., and Jacquet E. (2022) Isotopic evidence for two chondrule generations in CR chondrites and their relationships to other carbonaceous chondrites. *Earth Planet. Sci. Lett.* **593**, 117683.

Marrocchi Y., Longeau A., Goupil R. L., Dijon V., Pinto G., Neukampf J., Villeneuve J., Jacquet E. (2024) Isotopic evolution of the inner solar system revealed by size-dependent oxygen isotopic variations in chondrules. *Geochim. Cosmochim. Acta* **371**, 52–64.

Nagashima K., Krot A. N., and Huss G. R. (2014) ^{26}Al in chondrules from CR2 chondrites. *Geochem. J.* **48**, 561–570.

Nagashima K., Krot A. N., and Huss G. R. (2015) Oxygen-isotope compositions of chondrule phenocrysts and matrix grains in Kakangari K-grouplet chondrite: Implication to a chondrule-matrix genetic relationship. *Geochim. Cosmochim. Acta* **151**, 49–67.

Nagashima K., Krot A. N., and Komatsu M. (2017) ^{26}Al–^{26}Mg systematics in chondrules from Kaba and Yamato 980145 CV3 carbonaceous chondrites. *Geochim. Cosmochim. Acta* **201**, 303–319.

Nagashima K., Kita N. T., and Luu T.-H. (2018) In *Chondrules: Records of Protoplanetary Disk Processes* (eds. S. S. Russell, H. Connolly and A. N. Krot). Cambridge University Press, Cambridge U.K, pp. 247–275.

Nakamura T., Noguchi T., and Akaki T. (2006) Mineralogy and oxygen isotope signatures of the Asuka 881020 CH chondrite. *Meteorit. Planet. Sci.* **41**(Suppl.), A128 (abstr.).

Nakamura T., Noguchi T., Tsuchiyama A., Ushikubo T., Kita N. T., Valley J. W., Zolensky M. E., Kakazu Y., Sakamoto K., Mashio E., Uesugi K., and Nakano T. (2008) Chondrulelike objects in short-period comet 81P/Wild 2. *Science* **321**, 1664–1667.

Nakashima D., Ushikubo T., Rudraswami N. G., Kita N. T., Valley J. W., and Nagao K. (2011) Ion

microprobe analyses of oxygen three-isotope ratios of chondrules from the Sayh al Uhaymir 290 CH chondrite using a multiple-hole disk. *Meteorit. Planet. Sci.* **46**, 857–874.

Nakashima D., Ushikubo T., Joswiak D. J., Brownlee D. E., Matrajt G., Weisberg M. K., Zolensky M. E., and Kita N. T. (2012) Oxygen isotopes in crystalline silicates of comet Wild 2: a comparison of oxygen isotope systematics between Wild 2 particles and chondritic materials. *Earth Planet. Sci. Lett.* **357–358**, 355–365.

Nakashima D., Kimura M., Yamada K., Noguchi T., Ushikubo T., and Kita N. (2020) Oxygen isotope study of the Asuka-881020 CH chondrite I: Non-porphyritic chondrules. *Geochim. Cosmochim. Acta* **290**, 180–200.

Noguchi T., Imae N., and Kimura M. (2004) Petrology and mineralogy of Asuka 881020: A preliminary report of the first CH chondrite found among the Japanese Antarctic meteorite collection. In *Proc. NIPR Symp. Antarct. Meteorites*, **28**, 62–63 (abstr.).

Noguchi T., Ohashi N., Tsujimoto S., Mitsunari T., Bradley J. P., Nakamura T., Toh S., Stephan T., Iwata N. and Imae N. (2015) Cometary dust in Antarctic ice and snow: past and present chondritic porous micrometeorites preserved on the Earth's surface. *Earth Planet. Sci. Lett.* **410**, 1–11.

Nuth J. A., Paquette J. A., and Farquhar A. (2012) Can lightning produce significant levels of mass-independent oxygen isotopic fractionation in nebular dust? *Meteorit. Planet. Sci.* **47**, 2056–2069.

Ogliore R. C., Huss G. R., Nagashima K., Butterworth A. I., and Gainsforsth Z. (2012) Incorporation of a late-forming chondrule into comet Wild 2. *Astrophys. J. Lett.* **745**, L19.

Pinto G. A., Jacquet E., Corgne A., Olivares F., Villeneuve J., and Marrocchi Y. (2024) Deciphering recycling processes during solar system evolution from magnesium-rich relict olivine grains in type II chondrules. *Geochim. Cosmochim. Acta* **364**, 65–78.

Piralla M., Villeneuve J., Batanova V., Jacquet E., and Marrocchi Y. (2021) Conditions of

chondrule formation in ordinary chondrites. *Geochim. Cosmochim. Acta* **313**, 295–312.

Piralla M., Villeneuve J., Schnuriger N., Bakaert D. V., and Marrocchi Y. (2023) A unified chronology of dust formation in the early solar system. *Icarus* **394**, 115427.

Richet R., Bottinga Y., and Javoy M. (1977) A review of hydrogen, carbon, nitrogen, oxygen, sulphur, and chlorine stable isotope fractionation among gaseous molecules. *Ann. Rev. Earth Planet. Sci.* **5**, 65-110.

Richter F. M. (2004) Timescales determining the degree of kinetic isotope fractionation by evaporation and condensation. *Geochim. Cosmochim. Acta* **68**, 4971–4992.

Rudraswami N. G., Ushikubo T., Nakashima D., and Kita N. T. (2011) Oxygen isotope systematics of chondrules in Allende CV3 chondrite: High precision ion microprobe studies. *Geochim. Cosmochim. Acta* **75**, 7596–7611.

Russell S. D. J., Longstaffe F. J., King P. L., and Larson T. E. (2010) The oxygen-isotope composition of chondrules and isolated forsterite and olivine grains from the Tagish Lake carbonaceous chondrite. *Geochim. Cosmochim. Acta* **74**, 2428–2499.

Sakamoto N., Seto Y., Itoh S., Kuramoto K., Fujino K., Nagashima K., Krot A. N., and Yurimoto H. (2007) Remnants of the early solar system water enriched in heavy oxygen isotopes. *Science* **317**, 231–233.

Salmeron R. and Ireland T. R. (2012) Formation of chondrules in magnetic winds blowing through the proto-asteroid belt. *Earth Planet. Sci. Lett.* **327-328**, 61–67.

Schrader D. L., Connolly, Jr., H. C., Lauretta D. S., Nagashima K., Huss G. R., Davidson J., and Domanik K. J. (2013) The formation and alteration of the Renazzo-like carbonaceous chondrites II: linking O-isotope composition and oxidation state of chondrule olivine. *Geochim. Cosmochim. Acta* **101**, 302–327.

Schrader D. L., Nagashima K., Krot A. N., Ogliore R. C., and Hellebrand E. (2014) Variations in the O-isotope compositions of gas during the formation of chondrules from the CR chondrites.

Geochim. Cosmochim. Acta **132**, 50–74.

Schrader D. L., Nagashima K., Krot A. N., Ogliore R. C., Yin Q.-Z., Amelin Y. A., Stirling C. H., and Kaltenbach A. (2017) Distribution of ^{26}Al in the CR chondrite chondrule-forming region of the protoplanetary disk. *Geochim. Cosmochim. Acta* **201**, 275–302.

Scott E. R. D. (1988) A new kind of primitive chondrite, Allan Hills 85085. *Earth Planet. Sci. Lett.* **91**, 1–18.

Scott E. R. D. and Krot A. N. (2003) Chondrites and their components. In *Meteorites, Comets, and Planets,* vol. 1, edited by A. M. Davis, pp. 143-200. Treatise on Geochemistry, edited by H. D. Holland and K. K. Turekian. Elsevier B. V., Amsterdam.

Simon J. I., Hutcheon I. D., Simon S. B., Matzel J. E. P., Ramon E. C., Weber P. K., Grossman L., and Depaolo D. J. (2011) Oxygen isotope variations at the margin of a CAI records circulation within the solar nebula. *Science* **331**, 1175–1178.

Siron G., Fukuda K., Kimura M., and Kita N. T. (2021) New constraints from ^{26}Al–^{26}Mg chronology of anorthite-bearing chondrules in unequilibrated ordinary chondrites. *Geochim. Cosmochim. Acta* **293**, 103–126.

Siron G., Fukuda K., Kimura M., and Kita N. T. (2022) High precision ^{26}Al-^{26}Mg chronology of chondrules in unequilibrated ordinary chondrites: Evidence for restricted formation ages. *Geochim. Cosmochim. Acta* **324**, 312–345.

Tartèsea R., Chaussidon M., Gurenko A., Delarue F., and Robert F. (2018) Insights into the origin of carbonaceous chondrite organics from their triple oxygen isotope composition. *Proc. Natl. Acad. Sci. USA* **115**, 8535–8540.

Tenner T. J., Ushikubo T., Kurahashi E., Nagahara H., and Kita N. T. (2013) Oxygen isotope systematics of chondrule phenocrysts from the CO3.0 chondrite Yamato 81020: evidence for two distinct oxygen isotope reservoirs. *Geochim. Cosmochim. Acta* **102**, 226–245.

Tenner T. J., Nakashima D., Ushikubo T., Kita N. T., and Weisberg M. K. (2015) Oxygen isotope

ratios of FeO-poor chondrules in CR3 chondrites: Influence of dust enrichment and H_2O during chondrule formation. *Geochim. Cosmochim. Acta* **148**, 228–250.

Tenner T. J., Kimura M., and Kita N. T. (2017) Oxygen isotope characteristics of chondrules from the Yamato-82094 ungrouped carbonaceous chondrite: Further evidence for common O-isotope environments sampled among carbonaceous chondrites. *Meteorit. Planet. Sci.* **52**, 268–294.

Tenner T. J., Ushikubo T., Nakashima D., Schrader D. L., Weisberg M. K., Kimura M., and Kita N. T. (2018) Oxygen isotope characteristics of chondrules from recent studies by secondary ion mass spectrometry. In *Chondrules: Records of Protoplanetary Disk Processes,* edited by S. S. Russell, H. C. Connolly Jr., and A. N. Krot, pp. 196 – 246. Cambridge Planetary Science, edited by F. Bagenal, D. Jewitt, C. Murray, J. Bell, R. Lorenz, F. Nimmo, S. Russell. Cambridge University Press.

Tenner T. J., Nakashima D., Ushikubo T., Tomioka N., Kimura M., Weisberg M. K., and Kita N. T. (2019) Extended chondrule formation intervals in distinct physicochemical environments: Evidence from Al-Mg isotope systematics of CR chondrite chondrules with unaltered plagioclase. *Geochim. Cosmochim. Acta* **260**, 133–160.

Ushikubo T., Kimura M., Kita N. T., and Valley J. W. (2012) Primordial oxygen isotope reservoirs of the solar nebula recorded in chondrules in Acfer 094 carbonaceous chondrite. *Geochim. Cosmochim. Acta* **90**, 242–264.

Ushikubo T., Nakashima D., Kimura M., Tenner T. J., and Kita N. T. (2013) Contemporaneous formation of chondrules in distinct oxygen isotope reservoirs. *Geochim. Cosmochim. Acta* **109**, 280–295.

Ushikubo T. and Kimura M. (2021) Oxygen-isotope systematics of chondrules and olivine fragments from Tagish Lake C2 chondrite: Implications of chondrule-forming regions in protoplanetary disk. *Geochim. Cosmochim. Acta* **293**, 328–343.

Valley J. W. and Kita N. T. (2009) In situ Oxygen Isotope Geochemistry by Ion Microprobe.

Mineralogical Association of Canada Short Course vol. **41**, 19–63.

Villeneuve J., Chaussidon M., and Libourel G. (2009) Homogeneous distribution of ^{26}Al in the solar system from the Mg isotopic composition of chondrules. Science 325, 985-988.

Walsh C., Nomura H., Millar T. J., and Aikawa Y. (2012) Chemical processes in protoplanetary disks. II. On the importance of photochemistry and X-ray ionization. *Astrophys. J.* **74**, 114.

Weisberg M. K., Ebel D. S., Connolly, Jr., H. C., Kita N. T. and Ushikubo T. (2011) Petrology and oxygen isotope compositions of chondrules in E3 chondrites. *Geochim. Cosmochim. Acta* **75**, 6556–6569.

Weisberg M. K., Ebel D. S., Nakashima D., Kita N. T., and Humayun M. (2015) Petrology and geochemistry of chondrules and metal in NWA 5492 and GRO 95551: A new type of metal-rich chondrite. *Geochim. Cosmochim. Acta* **167**, 256–285.

Weisberg M. K., Kita N. T., Fukuda K., Siron G., and Ebel D. S. (2021) Micro-distribution of oxygen isotopes in unequilibrated enstatite chondrites. *Geochim. Cosmochim. Acta* **300**, 279–295.

Williams C. D., Sanborn M. E., Defouilloy C., Yin Q.-Z., Kita N. T., Ebel D. S., Yamakawa A., and Yamashita K. (2020) Chondrules reveal large-scale outward transport of inner Solar System materials in the protoplanetary disk. *Proc. Natl. Acad. Sci. U. S. A.* **117**, 23426–23435.

Yamanobe M., Nakamura T., and Nakashima D. (2018) Oxygen isotope reservoirs in the outer asteroid belt inferred from oxygen isotope systematics of chondrule olivines and isolated forsterite and olivine grains in Tagish Lake-type carbonaceous chondrites, WIS 91600 and MET 00432. *Polar Sci.* **15**, 29–38.

Zanda B., Bourot-Denise M., Perron C., and Hewins R. H. (1994) Origin and metamorphic redistribution of silicon, chromium, and phosphorous in the metal of chondrites. *Science* **265**, 1846–1849.

Zhang M., Fukuda K., Spiccuza M. J., Siron G., Heimann A., Hammerstrom A. J., Kita N. T.,

Ushikubo T., and Valley J. W. (2022) SIMS matrix effects in oxygen isotope analysis of olivine and pyroxene: Application to Acfer 094 chondrite chondrules and reconsideration of the primitive chondrule minerals (PCM) line. *Chem. Geol.* **608**, 121016.

Oxygen isotope study of the Asuka-881020 CH chondrite II: Porphyritic chondrules

Daisuke Nakashima[1,2,*], Takaaki Noguchi[3,4], Takayuki Ushikubo[2,5], Makoto Kimura[6,7],and Noriko Kita[2]

[1]Department of Earth Science, Tohoku University, Aoba, Sendai, Miyagi 980-8578, Japan

[2]Department of Geoscience, University of Wisconsin-Madison, Madison, WI 53706, USA

[3]Faculty of Arts and Science, Kyushu University, 744 Motooka, Nishi-ku, Fukuoka 819-0395, Japan

[4]Division of Earth and Planetary Sciences, Kyoto University, Kyoto 606-8502, Japan.

[5]Kochi Institute for Core Sample Research, JAMSTEC, Monobe-otsu 200, Nankoku, Kochi 783-8502, Japan

[6]Faculty of Science, Ibaraki University, Mito, Ibaraki, 310-8512, Japan

[7]National Institute of Polar Research, Tokyo 190-8518, Japan

*Corresponding author, Tel/Fax: +81-22-795-5903, Email: dnaka@tohoku.ac.jp

Submitted to Geochimica Cosmochimica et Acta

Keywords: CH chondrite, chondrules, oxygen isotopes

Abstract

Oxygen isotope ratios and elemental compositions of porphyritic chondrules and olivine and pyroxene fragments in the Asuka-881020 CH chondrite were analyzed. The oxygen isotope ratios inside individual porphyritic chondrules are homogeneous within the uncertainty, except for relict grains of olivine and low-Ca pyroxene that have distinct oxygen isotope ratios. The average oxygen isotope ratios of the individual chondrules plot along and above the primitive chondrule mineral (PCM) line with $\Delta^{17}O$ (= $\delta^{17}O - 0.52 \times \delta^{18}O$) values from –4.7‰ to +4.1‰. The olivine and pyroxene fragments, which have $\Delta^{17}O$ values ranging from –2.1‰ to +3.2‰, are likely to be fragments of the porphyritic chondrules.

Unlike the non-porphyritic chondrules in CH and CB chondrites and chondrules in other carbonaceous chondrites, the type I and II chondrules do not show a systematic difference in the $\Delta^{17}O$ values. Furthermore, the $\Delta^{17}O$ values of the type I chondrules increase from –4.7‰ to +4.1‰ with increasing Mg# (= molar [MgO]/[MgO+FeO]×100) from 96 to 99. We argue that the positive $\Delta^{17}O$-Mg# trend is explained by an addition of ^{16}O-poor carbon-rich organics as a reducing agent to the relatively ^{16}O-rich precursor silicate, which is a new environment for chondrule formation. This hypothesis is supported by the two lines of evidence observed in the present study. (1) The chondrules and fragments with higher $\Delta^{17}O$ values show larger deviations from the PCM line towards low $\delta^{18}O$, suggesting oxygen isotope mass fractionation between the chondrule melt and CO or CO_2. (2) Olivine phenocrysts in the chondrules with high $\Delta^{17}O$ values contain Ni-poor Fe-metal particles surrounded by silica-rich glass, which may be reduction products during the chondrule formation. Thus, it is suggested that the porphyritic chondrules in CH and CB chondrites have different origins from chondrules in any other chondrite types, even from the non-porphyritic chondrules in CH and CB chondrites.

1. Introduction

Chondrules are igneous spherules composed mainly of olivine, pyroxene, glass, and Fe-Ni metal and are observed in most chondritic meteorites (e.g., Gooding and Keil, 1981; Scott and Krot, 2003). Chondrules have formed by transient heating and rapid cooling (e.g., Jones et al., 2005), ~ 1 – 5 Myr after the oldest Ca-Al-rich inclusions (CAIs) (e.g., Kita et al., 2000; Kurahashi et al., 2008; Hutcheon et al., 2009; Villeneuve et al., 2009; Kita and Ushikubo, 2012; Ushikubo et al., 2013; Nagashima et al., 2014, 2017, 2018; Schrader et al., 2017; Hertwig et al., 2019a; Tenner et al., 2019; Siron et al., 2021, 2022; Fukuda et al., 2022; Piralla et al., 2023). Based on the textures, chondrules are classified into porphyritic and non-porphyritic types (Gooding and Keil, 1981). Porphyritic chondrules have been heated to near-liquidus temperatures, and nucleation sites resulting from incomplete melting of precursor materials persist: growth of crystals can occur on multiple nucleation sites as the chondrule cools. Non-porphyritic chondrules have been heated above the liquidus, and most nucleation sites have been destroyed during the melting interval (Jones, 2012). Based on the Mg# (= molar [MgO]/[MgO+FeO]×100), chondrules are classified into type I (FeO-poor; Mg# ≥ 90) and type II (FeO-rich; Mg# < 90) (e.g., Jones et al., 2005). The Mg# of chondrules is controlled by the oxygen fugacity of the chondrule-forming environment (Ebel and Grossmann, 2000; Zanda et al., 1994), and type I chondrules formed under more reducing conditions than type II chondrules (e.g., Tenner et al., 2015; Hertwig et al., 2018), though precursor compositions of individual chondrules can also affect the Mg# of chondrules (Connolly et al., 1994). Since chondrule-like objects were observed in cometary samples such as particles returned from comet Wild 2 (Nakamura et al., 2008; Ogliore et al., 2012; Joswiak et al., 2014), it is considered that chondrules were widely distributed in the protoplanetary disk even in the Kuiper belt region. Thus, chondrules are essential for understanding of the material evolution in the early Solar System.

In-situ analyses of chondrules in Acfer 094 (ungrouped C3.0) using secondary ion mass

spectrometry (SIMS) revealed that oxygen isotope ratios of the chondrules are distributed along the slope ~ 1 line of $\delta^{17}O = (0.978 \pm 0.013) \times \delta^{18}O - (2.70 \pm 0.11)$ in the oxygen three-isotope diagram, which is called as the primitive chondrule mineral (PCM) line (Ushikubo et al., 2012). Oxygen isotope ratios of individual mineral phases in chondrules from pristine carbonaceous chondrites plot along and above the PCM line (Connolly and Huss, 2010; Russell et al., 2010; Rudraswami et al., 2011; Schrader et al., 2013, 2014, 2017; Tenner et al., 2013, 2015, 2017, 2018; Davidson et al., 2014; Chaumard et al., 2018, 2021; Hertwig et al., 2018, 2019a, 2019b; Marrocchi et al., 2018, 2019, 2021, 2022; Yamanobe et al., 2018; Ushikubo and Kimura, 2021; Fukuda et al., 2022; Zhang et al., 2022; Pinto et al., 2024). Since the PCM line represents the primary trend of the major oxygen isotope reservoirs (^{16}O-rich CAIs and ^{16}O-poor cosmic symplectites) in the protoplanetary disk, chondrules that plot around the PCM line originated from the reservoirs (Ushikubo et al., 2012). Recent high precision analyses of chondrules further revealed that there are two groups of chondrules among carbonaceous chondrites that plot slightly below and above the PCM line, some of which show correlation to nucleosynthetic anomalies of Cr and Ti (Williams et al., 2020; Zhang et al., 2022). The chondrules with Cr and Ti isotope anomalies may have come from formation regions of ordinary chondrite chondrules (Williams et al., 2020). On the other hand, Schneider et al. (2020) found no carbonaceous chondrite chondrules related to ordinary chondrite chondrules from the Cr-Ti-O isotope analyses.

Oxygen isotope ratios of the Acfer 094 chondrules are internally homogeneous, except for relict grains that have distinct oxygen isotope ratios (Ushikubo et al., 2012). The Acfer 094 chondrules show bimodal $\Delta^{17}O$ ($= \delta^{17}O - 0.52 \times \delta^{18}O$) values of ~ −5‰ and −2‰ that negatively correlate with the Mg# values of chondrule phenocrysts, suggesting the former presence of two separate isotope reservoirs with different redox states in the protoplanetary disk and that the homogeneous oxygen isotope ratios represent localized oxygen isotope reservoirs in the disk (Ushikubo et al., 2012). Other primitive carbonaceous chondrites also show similar systematic

trends between Mg# and $\Delta^{17}O$ values, though the detailed trends are specific to individual chondrite groups (Connolly and Huss, 2010; Russell et al., 2010; Rudraswami et al., 2011; Schrader et al., 2013, 2014, 2017; Tenner et al., 2013, 2015, 2017, 2018; Davidson et al., 2014; Chaumard et al., 2018, 2021; Hertwig et al., 2018, 2019a, 2019b; Marrocchi et al., 2018, 2019, 2021, 2022; Yamanobe et al., 2018; Ushikubo and Kimura, 2021; Fukuda et al., 2022; Pinto et al., 2024). Continuous negative $\Delta^{17}O$-Mg# trends have been observed from chondrules in CR chondrules that are explained by an addition of ^{16}O-poor water ice as an oxidant to the ^{16}O-rich anhydrous solid precursors (Tenner et al., 2015). An addition of ^{16}O-poor CI-like dust is also suggested, which is supported by the peculiar ^{54}Cr signature of CR chondrules (Marrocchi et al., 2022).

In metal-rich carbonaceous CH and CB chondrites, non-porphyritic chondrules such as cryptocrystalline (CC) and skeletal olivine (SO) chondrules dominate the chondrule inventory (≥ 80%), though with their huge size difference between CH chondrules and CB chondrules (0.02 – 0.09 mm and 0.5 – 5 mm; Scott and Krot, 2003). Nakashima et al. (2020) reported that $\Delta^{17}O$ values of the non-porphyritic chondrules negatively correlate with the Mg#, similar to chondrules in other carbonaceous chondrites. Porphyritic chondrules, which are minor in CH and CB chondrites (≤ 20%; Scott and Krot, 2003), have a variation in the $\Delta^{17}O$ values from ~ –4‰ to +4‰ (excluding internally heterogeneous chondrules containing relict minerals; Krot et al., 2010), though the relationship with Mg# has not been discussed.

Lithic fragments, which are olivine and pyroxene fragments and olivine-pyroxene-normative fragments, occur around chondrules and Fe-Ni metal in CH chondrites instead of fine-grained matrix in pristine chondrites (Scott, 1988; Grossman et al., 1988). Nakashima et al. (2020) suggested that the olivine-pyroxene-normative fragments are fragments of CC chondrules in CH chondrites based on the similarity in oxygen isotope ratios. The possibility that olivine and pyroxene fragments are fragments of the porphyritic chondrules in CH chondrites (Scott, 1988)

can also be tested based on the oxygen isotope ratios.

In this study, oxygen isotope ratios and elemental compositions of porphyritic chondrules and olivine and pyroxene fragments in the Asuka (A) -881020 CH chondrite (Noguchi et al., 2004; Nakamura et al., 2006) were analyzed to understand oxygen isotope reservoirs and redox conditions in the formation environments of the porphyritic chondrules. As a result, a unique Δ^{17}O-Mg# trend is observed for the type-I chondrules and FeO-poor fragments; the Δ^{17}O values positively correlate with Mg#. We propose that the unique trend is caused by an addition of ^{16}O-poor carbon-rich organics as a reducing agent to the ^{16}O-rich precursors. The hypothesis is tested based on the mineralogy and chemistry including observation with transmission electron microscopy of the porphyritic chondrules and olivine and pyroxene fragments.

2. Analytical procedures

2.1. Electron microscopy

We used a polished thin section of the A-881020 CH chondrite (51-1; National Institute of Polar Research). Chondrules and olivine and pyroxene fragments in the section were examined using a scanning electron microscope (SEM; Hitachi S3400) at the University of Wisconsin-Madison and a field emission SEM (FE-SEM; JEOL JSM7001F) at Tohoku University. Backscattered electron (BSE) images were obtained. Elemental compositions of the chondrules and olivine and pyroxene fragments were measured using electron probe microanalyzers (EPMAs) at Ibaraki University (JEOL JXA-733), at National Institute of Polar Research (NIPR; JEOL JXA-8200), and at the University of Wisconsin-Madison (CAMECA SX-51) equipped with wavelength-dispersive X-ray spectrometers (WDSs). At Ibaraki University, WDS quantitative chemical analyses of bulk chondrules were performed at 15 kV accelerating voltage and 6 nA beam current with a defocused beam of 5 - 40 μm. After correction by the Bence-Albee method, the chondrule data were recalculated by the method of Ikeda (1980) to reduce the polyphase effect. Quantitative

chemical analyses of olivine and pyroxene fragments and individual silicate phases in chondrules were performed with a focused beam (10 nA) at Ibaraki University, NIPR, and University of Wisconsin-Madison (other analytical settings are the same as those for bulk chondrule analyses). Natural and synthetic standards were chosen based on the compositions of the minerals being analyzed (e.g., Tenner et al., 2015). Detection limits of oxide concentrations are shown in the Supplementary Tables A1.

2.2. Raman spectroscopy

The structural nature of chondrule silica was determined by laser micro-Raman spectroscopy, using a JASCO NRS-3100 spectrometer at Kyushu University. A microscope was used to focus the excitation laser beam (532 nm). The acquisition time was 30 s. For each region analyzed a Raman spectrum was acquired in the spectral region of 240 to 1340 cm^{-1}. Raman spectra were also acquired on the regions where tiny vesicles are dispersed in olivine phenocrysts of chondrules for the identification of gaseous compounds that may be trapped in the vesicles. The spectral region is from 1200 to 2200 cm^{-1}. Other analytical conditions are the same as those for chondrule silica.

2.3. Oxygen isotope analyses

Oxygen isotope ratios of porphyritic chondrules and olivine and pyroxene fragments in A-881020 were analyzed with the CAMECA IMS-1280 ion microprobe at the WiscSIMS laboratory (Kita et al., 2009). For the oxygen three-isotope analyses, two sizes of focused Cs^+ primary beam (10 × 15 μm at the intensity of ~ 3 nA and 2 × 4 μm at ~ 30 pA) were applied. The analytical conditions and measurement procedures were similar to those in Kita et al. (2010) and Nakashima et al. (2011). The secondary $^{16}O^-$, $^{17}O^-$, and $^{18}O^-$ ions were detected simultaneously by Faraday cups (FC) or electron multipliers (EM) on the multicollection system; three FCs for $^{16}O^-$, $^{17}O^-$, and $^{18}O^-$ for 15 μm spot analyses and a FC for $^{16}O^-$ and two EMs for $^{17}O^-$, and $^{18}O^-$ for 4 μm spot

analyses. Intensities of $^{16}O^-$ were ~ 3 × 10^9 cps and ~ 2 × 10^7 cps with 15 μm and 4 μm primary beams, respectively. The baselines of the FCs were measured during the presputtering (100 s for 15 μm spots and 360 s for 4 μm spots) in respective analyses and used for data correction. The contribution of the tailing of $^{16}O^1H^-$ interference to $^{17}O^-$ signal was corrected by the method described in Heck et al. (2010), though the contribution was negligibly small (typically < 0.1‰).

One to six analyses were performed for individual chondrules and olivine and pyroxene fragments, bracketed by eight to nine analyses (four or five analyses before and after the unknown sample analyses) on the San Carlos olivine standard grain in a separated mount (Supplementary Table A2). The external reproducibility of the running standard was 0.19 – 0.54‰ for $\delta^{18}O$, 0.35 – 0.66‰ for $\delta^{17}O$, and 0.21 – 0.68‰ for $\Delta^{17}O$ for 15 μm spot analyses, and that for 4 μm spot analyses was 0.73 – 1.18‰ for $\delta^{18}O$, 0.97 – 1.82‰ for $\delta^{17}O$, and 1.09 – 2.04‰ for $\Delta^{17}O$ (2SD; standard deviation). The external reproducibility was assigned as analytical uncertainties of unknown samples (see Kita et al., 2009, 2010 for detailed explanations). We used two olivine (Fo_{100} and Fo_{60}), three low-Ca pyroxene (En_{97}, En_{90}, and En_{85}), diopside, plagioclase (An_{95}), quartz, and four glass (50.9 – 76.0 wt% SiO_2) standards (Valley and Kita, 2009; Kita et al., 2010) in the same sessions for correction of instrumental bias of olivine, pyroxene, plagioclase, silica, and glass (Supplementary Table A3).

Porphyritic chondrules and mineral fragments of olivine and pyroxene were selected for oxygen isotope analysis are located within the radius of 5 mm of the center of the 1-inch round thin section of A-881020 in the same manner as that for the non-porphyritic chondrules (Nakashima et al., 2020) to avoid instrumental mass fractionation due to the X-Y effect (Kita et al., 2009). In each porphyritic chondrule, 1 to 6 spot analyses were made. The 15 μm beam was used for olivine and low-Ca pyroxene phenocrysts larger than 15 μm, and the 4 μm beam was used for those smaller than 15 μm, high-Ca pyroxene, glass, plagioclase, and silica (Supplementary Fig. A1).

2.4. Sample sectioning using focused ion beam and transmitted electron microscopy

For the observation of Fe-particles smaller than 1 μm in olivine phenocrysts in chondrules using a transmitted electron microscope (TEM), thin sections (~ 180 nm) of olivine phenocrysts containing Fe-particles were cut out using a focused ion beam (FIB) on a JEOL JIB-4501 FIB-SEM at Kyushu University. A 30 kV Ga^+ ion beam set to 50 pA – 100 nA was used. The FIB marks of 1 μm × 1 μm were made at both ends of the FIB sectioning area by removing carbon coating on the sample surface (e.g., Nakashima et al., 2012), as the Fe-particles are tiny and hidden from view after deposition of a W-layer. NanoMill TEM specimen preparation system (Model 1050) was used for removing amorphous layers on the surfaces of the thin sections formed during FIB sectioning. Two settings of Ar^+ ion beam (900 V and 500 V; intensity of 35 pA) were used. The FIB sections with a thickness of ~ 80 nm were observed using JEOL JEM-3200FSK TEM equipped with the JED-2200 energy-dispersive X-ray spectrometer (EDS) at Kyushu University. The accelerating voltage was 300 kV. Quantitative analysis was performed using the Cliff-Lorimer correction with the TEM-EDS, and the element concentrations were corrected using k factors obtained by measuring mineral standards (Noguchi et al., 2015).

3. Results

Search for porphyritic chondrules and olivine and pyroxene fragments large enough for 15 μm and 4 μm spot SIMS analysis and electron microprobe and SIMS analyses were conducted along with those of the non-porphyritic chondrules and lithic fragments in the same meteorite in the same sessions (Nakashima et al., 2020). In Nakashima et al. (2020), the non-porphyritic chondrules and lithic fragments are numbered as C1 – C37 and F1 – F40. In the present paper, the porphyritic chondrules and olivine and pyroxene fragments are sequentially numbered as C38 – C59 (n = 22) and F41 – F61 (n = 21), respectively (Supplementary Table A1).

3.1. Petrology and mineralogy of porphyritic chondrules

Porphyritic chondrules in A-881020 are 50 – 380 μm in size (170 μm on average; Fig. 1; Supplementary Fig. A1) and smaller than (or as small as) those in other chondrite groups (Friedrich et al., 2014). The porphyritic chondrules consist mainly of olivine and low-Ca pyroxene phenocrysts, Fe-Ni metal, and glass. The porphyritic chondrules contain accessory phases of high-Ca pyroxene with Wo# from 21.5 to 43.5, pyroxene with intermediate compositions ($En_{78.1-93.7}Wo_{5.0-18.5}$), plagioclase with An# from 75.6 to 91.7, and silica (Supplementary Table A1). Pyroxene with intermediate compositions is called as intermediate pyroxene (Tenner et al., 2015). Nepheline or sodalite, a product of metasomatism (e.g., Kimura and Ikeda, 1995; Krot et al., 1998), is not observed in glass and plagioclase in the porphyritic chondrules. Electron microprobe analyses of glass and plagioclase show totals higher than 98 wt% (Supplementary Table A1), indicating no replacement by phyllosilicates.

Most of the porphyritic chondrules are porphyritic olivine (PO), porphyritic olivine-pyroxene (POP), and porphyritic pyroxene (PP) types. There are two chondrules with unique textures. C46 consists of a low-Ca pyroxene core surrounded by a glassy rim. C58 consists of an olivine core surrounded by a rim composed of low-Ca pyroxene, silica, and microcrystalline mesostasis (Supplementary Fig. A1). Silica in C58 is cristobalite, as the Raman spectra showed a peak around 420 cm^{-1}. Sub-μm sized Cr-spinel particles (detected by FE-SEM-EDS) occur between the olivine core and surrounding low-Ca pyroxene (Supplementary Fig. A1).

In each chondrule, olivine and low-Ca pyroxene compositions are homogeneous with small variations in Fo#, En#, and Wo# of less than 2.6, 2.1, and 1.8 (1SD). The averaged olivine Fo# range from 73.2 to 99.1, and averaged low-Ca pyroxene En# and Wo# range from 89.8 to 97.4, and from 0.5 to 4.2, respectively. The Fo# of 73.2 is from a PO chondrule (C59; Fig. 1j), which is a type II chondrule with no Fe-Mg zoning in olivine phenocrysts. Others are type I chondrules

with Mg# of olivine and low-Ca pyroxene phenocrysts higher than 91. Mg# of individual chondrules in Table 1 are average values of Mg# of olivine and low-Ca pyroxene in the chondrules.

3.2. Bulk elemental compositions of porphyritic chondrules

Bulk elemental compositions of porphyritic chondrules were obtained by broad-beam EPMA analyses, though they may not reflect true compositions of individual chondrules (Jones, 2005). Refractory element abundances in the porphyritic chondrules in A-881020 are systematically higher than those in CC chondrules in CH and CB chondrites (Krot et al., 2010; Nakashima et al., 2011, 2020) and as high as those in chondrules in other carbonaceous chondrites (Hezel and Palme, 2010) (Fig. 2).

3.3. Fe-particles and vesicles in olivine phenocrysts in porphyritic chondrules

Olivine phenocrysts in more than a half of porphyritic chondrules contain sub-μm sized Fe-particles (detected by FE-SEM-EDS) and vesicles, which are linearly aligned (Fig. 3; Supplementary Fig. A1). No Fe-Mg zoning is observed in the olivine phenocrysts. The Fe-particles and vesicles are also observed in plagioclase in the chondrule C47 (Fig. 3d). Raman spectra were obtained in the regions where the vesicles occur, but any peak suggesting the presence of gaseous species in vesicles is not observed. Instead, the observed Raman spectra are similar to those of epoxy (e.g., Hardis et al., 2013), which is underneath the thin section.

The BSE images show Fe-particles and vesicles distribute on the cut surface of the FIB sections (Figs. 4a, 4d), which were cut out along the aligned Fe-particles and vesicles from the olivine phenocrysts. Therefore, the Fe-particles and vesicles distribute on a plane almost perpendicular to the polished surface of the chondrule olivine phenocrysts. The HAADF-STEM images of the FIB section from the chondrule C40 (grid-1) show that the Fe-particles smaller than 0.5 μm are surrounded by silica-rich glass in the host olivine (Figs. 4b, 4c). Tiny Fe-particles

surrounded by silica-rich glass are also observed in dusty olivine (Leroux et al., 2003). In the FIB section from the chondrule C41 (grid-2), vesicles occur along with Fe-particles in the host olivine with dislocations (Fig. 4e). An electron diffraction pattern of the largest Fe-particle (~ 2 μm in size) in the grid-2 shows that it is a bcc Fe-metal, i.e., kamacite (Fig. 4f). The same may be true for other tiny Fe-particles. The Fe-particles are Ni-free or contain small concentrations of Ni (Table 3). The average Ni concentration is 2.5 ± 2.3 wt% (n = 7; 1σ). Silica-rich glass surrounding the Ni-poor Fe-metal particles shows similar elemental composition to those in the Bishunpur LL3.1 chondrite (Leroux et al., 2003) and contain CaO and Al_2O_3 of ~ 19 wt% and 24 wt% (Fig. 5; Table 4).

3.4. Petrology and mineralogy of olivine and pyroxene fragments

Lithic fragments that present in interstitial spaces between chondrules and Fe-Ni metal are olivine, low- and high-Ca pyroxene, and olivine-pyroxene-normative CC fragments (including silica-bearing fragments; Fig. 6; see also Nakashima et al., 2020). Except for the olivine-pyroxene-normative CC fragments, chemical compositions of the lithic fragments are close to stoichiometric olivine and low- and high-Ca pyroxene (Supplementary Table A1). Thirteen of the 21 olivine and pyroxene fragments are FeO-poor with Mg# of 90.7 – 99.3, and others are FeO-rich with Mg# of 50.5 – 80.0 (Table 2). FeO-rich olivine fragments do not show Fe-Mg zoning (Supplementary Fig. A1).

3.5. Oxygen isotope ratios

We made a total of 110 spot analyses in 22 porphyritic chondrules and 21 olivine and pyroxene fragments. After inspection of the SIMS analysis spots by SEM, one analysis was rejected because it overlapped with an adjacent lithic fragment (F55; Supplementary Fig. A1). A summary of the 109 spot analyses taken from 22 chondrules and 20 lithic fragments is shown in

Tables 1 – 2; a more complete table is given in the Supplementary Table A4.

3.5.1. Oxygen isotope ratios of porphyritic chondrules

Oxygen isotope ratios of individual spot analyses in the porphyritic chondrules are distributed along and above the PCM line (Ushikubo et al., 2012; Zhang et al., 2022) and the Carbonaceous Chondrite Anhydrous Mineral (CCAM) line (Clayton et al., 1977) (Figs. 1b, 1e, 1h, 1k; Supplementary Fig. A1). The individual chondrules are isotopically uniform within the uncertainty, except for four chondrules with isotopically distinct relict grains and one chondrule (C43) containing olivine phenocrysts with heterogeneous oxygen isotope ratios (Fig. 1; Supplementary Fig. A1). The homogeneous oxygen isotope ratios represent those of the final chondrule melt and are referred as "host" chondrule oxygen isotope ratios, and especially chondrule glass in pristine chondrites preserves the oxygen isotope ratios of the chondrule-forming melts (Ushikubo et al., 2012). The isotopically distinct relict grains, which are mostly olivine, survived the final chondrule formation event and do not reflect oxygen isotope ratios of the final chondrule melt (e.g., Ushikubo et al., 2012). In C43, any olivine phenocryst analyzed for oxygen isotopes is possibly relict.

The relict grains are defined as the grains of which $\Delta^{17}O$ values are different from the host $\Delta^{17}O$ values by more than 3SD of individual analyses in the chondrules (e.g., Ushikubo et al., 2012). The relict grains are excluded from the calculation of average oxygen isotope ratios of the individual chondrules. The oxygen isotope ratios in the individual chondrules were measured with two different beam settings, which have different uncertainties (Supplementary Table A2). Therefore, the error-weighted average oxygen isotope ratios of individual chondrules are calculated. The uncertainties of the average values in the individual chondrules were estimated from the 2 standard error (2SE) of chondrule analyses (2SD/$\sqrt{}$number of chondrule analyses), unless it is smaller than the 2SE of bracketing standard analyses (2SD/$\sqrt{}$number of chondrule analyses). The average oxygen isotope ratios of individual chondrules are distributed along and

above the PCM line with $\delta^{18}O$ values from –1.3‰ to +11‰ (Fig. 7a).

In the two chondrules (C41 and C44), isotopically distinct low-Ca pyroxene grains are observed (Supplementary Fig. A1). In C44, four spot data from olivine and low-Ca pyroxene have an average $\Delta^{17}O$ value of –6.4 ± 0.9‰ (2σ), and two spot data from glass and low-Ca pyroxene have an average $\Delta^{17}O$ value of –0.3 ± 1.2‰ (Figs. 1h and 1i; Table 1). Therefore, the host $\Delta^{17}O$ value of C44 is ~ –0.3‰, and olivine and low-Ca pyroxene with $\Delta^{17}O$ of ~ –6‰ are relict.

3.5.2. Oxygen isotope ratios of olivine and pyroxene fragments

Most of the olivine and pyroxene fragments were analyzed with a 15 μm beam (Fig. 6; Supplementary Fig. A1). The oxygen isotope ratios show a variation from –3.9‰ to +11.8‰ in $\delta^{18}O$ along and above the CCAM and PCM lines (Fig. 7b; Supplementary Fig. A1). The $\delta^{18}O$ ranges for the FeO-poor fragments and FeO-rich ones overlap each other; –3.9‰ to +9.9‰ and +3.8‰ to +11.9‰. There is no systematic difference in $\delta^{18}O$ ranges between FeO-poor olivine and pyroxene and between FeO-rich olivine and pyroxene.

4. Discussion

For carbonaceous chondrites, chondrules with lower Mg# tend to have higher $\Delta^{17}O$ values, which is attributed to an addition of ^{16}O-poor water ice as an oxidant to relatively ^{16}O-rich precursor dust (e.g., Ushikubo et al., 2012; Tenner et al., 2015) or an addition of ^{16}O-poor CI-like dust (Marrocchi et al., 2022). However, there appears to be no systematic difference in the $\Delta^{17}O$ values between type I and II chondrules in CH and CB chondrites (Krot et al., 2010). In the present study, oxygen isotope ratios of porphyritic chondrules from the A-881020 CH chondrites are obtained to see if there is a systematic trend between the $\Delta^{17}O$ values and Mg#. But, only one type II chondrule is available (C59; Mg# = 73.2). Instead, FeO-rich olivine and pyroxene fragments, which may be fragments of the type II porphyritic chondrules (e.g., Scott, 1988), are analyzed for

the oxygen isotope ratios. Before discussing the Δ^{17}O-Mg# relationship of the porphyritic chondrules, we test if the olivine and pyroxene fragments are fragments of the porphyritic chondrules based on the chemistry and oxygen isotope ratios.

4.1. Genetic link between the olivine and pyroxene fragments and porphyritic chondrules

Inter-chondrule spaces in CH chondrites are filled with lithic fragments, which comprise ~ 70 vol% (e.g., Scott, 1988; Scott and Krot, 2003). The remaining ~ 30 vol% is composed mostly of chondrules (5 vol%), Fe-Ni metal (20 vol%), and hydrous matrix lumps (5 vol%) (e.g., Scott, 1988). The lithic fragments are olivine, pyroxene, and olivine-pyroxene normative materials like CC chondrules (e.g., Scott, 1988). Nakashima et al. (2020) suggested that the CC-like lithic fragments are fragments of CC chondrules, based on their indistinguishable Δ^{17}O values and depletion in refractory elements such as Ca and Al (Fig. 2).

For the FeO-poor lithic fragments (Mg# of 90.7-99.3) with Δ^{17}O of –5.0‰ to +3.0‰ (Fig. 8a), there are two possible candidates for their origin, namely porphyritic or SO chondrules from CH and CB chondrites. The SO chondrules, which have FeO-poor compositions, contain pyroxene and olivine (e.g., Krot et al., 2007). The Δ^{17}O variation of the SO chondrules is very limited (–2.4 ± 1.3‰ on average; 2SD; Krot and Nagashima, 2017). On the other hand, the Δ^{17}O variation of the type I porphyritic chondrules (–4.7‰ to +4.1‰; Fig. 8a) is as large as those of the FeO-poor fragments. FeO-poor fragments analyzed for oxygen isotopes are larger than olivine and pyroxene in SO chondrules (Krot et al., 2007; Nakashima et al., 2020) and as large as those in the porphyritic chondrules (Figs. 1 and 6; Supplementary Fig. A1). For the FeO-rich fragments (Mg# of 50.5 – 80.0) with Δ^{17}O of –3.2‰ to +1.5‰ (Fig. 8a), there are two possible candidates for their origin, porphyritic or silica-bearing chondrules with immiscibility textures (SB-I chondrules; Mg# of 66.3 – 92.3; Nakashima et al., 2020) in CH and CB chondrites. The latter contains pyroxene but no olivine (e.g., Nakashima et al., 2020). The Δ^{17}O variation of the SB-I chondrules is very limited

(+1.5 ± 1.1‰ on average; Nakashima et al., 2020). On the other hand, the $\Delta^{17}O$ variation of the type II porphyritic chondrules (–2.1‰ to +2.7‰; Krot et al., 2010; Fig. 8a) is as large as those of the FeO-poor fragments. Thus, it is likely that the olivine and pyroxene fragments analyzed for oxygen isotopes are fragments of porphyritic chondrules, though there may be olivine and pyroxene fragments from SO chondrules and SB-I chondrules.

In conjunction with the suggestion that the CC-like lithic fragments are fragments of CC chondrules (Nakashima et al., 2020), it is considered that the silicate fraction that comprises 75 vol% of CH chondrites (excluding hydrous matrix lumps) is composed mostly of chondrules and their fragments. As suggested in Nakashima et al. (2020), fragmentation of chondrules may have occurred during the accretion to the parent body and/or brecciation on the surface of the parent body. Thus, the inter-chondrule spaces in CH chondrites are filled with chondrule fragments.

4.2. Comparison of the $\Delta^{17}O$-Mg# trends

Chondrules in carbonaceous chondrites are known to show a systematic increase of $\Delta^{17}O$ values with decreasing Mg# (Figs. 8b-d; Connolly and Huss, 2010; Krot et al., 2010; Russell et al., 2010; Ushikubo et al., 2012; Schrader et al., 2013, 2014, 2017; Tenner et al., 2013, 2015, 2017, 2018; Chaumard et al., 2018, 2021; Hertwig et al., 2018, 2019a, 2019b; Marrocchi et al., 2018, 2019, 2021, 2022; Yamanobe et al., 2018; Nakashima et al., 2020; Ushikubo and Kimura, 2021; Fukuda et al., 2022; Pinto et al., 2024). The $\Delta^{17}O$-Mg# trends have been explained by an addition of ^{16}O-poor water ice as an oxidant to the ^{16}O-rich anhydrous solid precursors (e.g., Tenner et al., 2015; Hertwig et al., 2018), an addition of ^{16}O-poor CI-like dust (Marrocchi et al., 2022), or isotopically heterogeneous vapor plume resulting from a high temperature mixing of the ^{16}O-rich and ^{16}O-poor reservoirs (Libourel et al., 2023). The $\Delta^{17}O$-Mg# trends are specific to the individual carbonaceous chondrite groups (Figs. 8b-d) and are briefly described below.

For CO3.0, CV3, CM (-related), Acfer 094, and Yamato-82094 (ungrouped C3.2) chondrites,

there is mainly a bimodal distribution of $\Delta^{17}O$ at ~ –5‰ and ~ –2‰ for chondrules with Mg# > 97 and < 97 (including type II chondrules Fig. 8c; Ushikubo et al., 2012; Tenner et al., 2013, 2017; Chaumard et al., 2018, 2021; Hertwig et al., 2018, 2019b; Marrocchi et al., 2018, 2019; Hertwig et al., 2019a; Fukuda et al., 2022; Pinto et al., 2024).

Type I chondrules in CR chondrites show a monotonic increase in $\Delta^{17}O$ from –6‰ to –1‰ with decreasing Mg# from 99.2 to ~96 (Fig. 8d; Tenner et al., 2015), whereas those of type II chondrules vary from –2‰ to +1‰ (Connolly and Huss, 2010; see also Schrader et al., 2013, 2014, 2017; Marrocchi et al., 2022; Pinto et al., 2024). The $\Delta^{17}O$-Mg# trend of chondrules and chondrule fragments in the Tagish Lake-type carbonaceous chondrites is similar to that of the CR chondrite chondrules, but differ in the limited number of type I chondrules with Mg# < 98 and $\Delta^{17}O$ ~ –2‰ (Russell et al., 2010; Yamanobe et al., 2018; Ushikubo and Kimura, 2021; Marrocchi et al., 2021).

For non-porphyritic chondrules and lithic fragments with various textures in CH and CB chondrites, the $\Delta^{17}O$ values increase from –21‰ to +5‰ with decreasing Mg# from 99 to 60 (Fig. 8b; Nakashima et al., 2020; Krot et al., 2001, 2010, 2012, 2021). The non-porphyritic chondrules and lithic fragments are classified into three groups based on the $\Delta^{17}O$ values and Mg#. The first group, which is composed of SO and CC chondrules and their fragments, has indistinguishable $\Delta^{17}O$ values with an average of –2.3 ± 0.7‰ (2SD) and Mg# ranging from 91.7 to 99.6 (Table 3 in Nakashima et al., 2020). The second group, which is composed of an Al-rich chondrule, CC chondrules ± silica ± FeNi metal, and CC chondrule fragments, has positive $\Delta^{17}O$ values with an average of +1.4 ± 1.2‰ and Mg# ranging from 58.5 to 95.4. The third group, which is composed of Al-rich and CC chondrules and silica-bearing chondrules, has $\Delta^{17}O$ values with an average of –6.3 ± 0.7‰ and Mg# ranging from 91.1 to 99.3. Nakashima et al. (2020) suggested that the non-porphyritic chondrules and lithic fragments require multiple chondrule-forming environments with different redox states generated by multiple heating events, though Krot et al. (2021) suggest that FeO-poor and -rich non-porphyritic chondrules formed in an impact plume under different redox

conditions.

Most chondrules from the non-carbonaceous chondrites (LL3, E3, G, Kakangari, and R3) show fairly constant $\Delta^{17}O$ values (~ –1‰ to ~ +2‰) regardless of Mg# (Fig. 8e; Kita et al., 2010, 2015; Weisberg et al., 2011, 2015, 2021; Nagashima et al., 2015; Piralla et al., 2021; Siron et al., 2021, 2022), though recently Marrocchi et al. (2024) showed that ordinary chondrite chondrules smaller than 300 μm in diameter have negative $\Delta^{17}O$ values down to ~ –10‰. The constant $\Delta^{17}O$ values with a range of Mg# are explained by chondrule formation from precursors without large variations in $\Delta^{17}O$ values and a small amount of water ice under environments with variable dust/gas ratios (up to 10,000 times solar; Kita et al., 2010).

Unlike the chondrules in other chondrites and non-porphyritic chondrules in CH and CB chondrites, the porphyritic chondrules and fragments in CH and CB chondrites show a different $\Delta^{17}O$-Mg# trend. Fig. 8a compiles Mg# and $\Delta^{17}O$ values of the porphyritic chondrules and olivine and pyroxene fragments in A-881020 and other CH and CB chondrites (Krot et al., 2010). For the type I porphyritic chondrules and their fragments with Mg# > 96, the $\Delta^{17}O$ values increase from –4.7‰ to +4.1‰ with increasing Mg#. For the chondrules and their fragments with Mg# < 96, the $\Delta^{17}O$ values increase up to +3.2‰. Similarly, type II chondrules in CR and Tagish Lake-type chondrites have high $\Delta^{17}O$ values up to +2‰ (Fig. 8d). Their low Mg# and relatively high $\Delta^{17}O$ values are explained by an addition of ^{16}O-poor water ice to the ^{16}O-rich anhydrous precursors (e.g., Tenner et al., 2015). Therefore, the porphyritic chondrules and their fragments Mg# < 96 may have formed in the same manner. However, the positive $\Delta^{17}O$-Mg# correlation for the porphyritic chondrules and fragments with Mg# > 96 cannot be explained within this framework and can also not be linked to the formation conditions of non-carbonaceous chondrites (Fig. 8e). Instead, the positive $\Delta^{17}O$-Mg# correlation requires a different formation environment. There are two possible explanations for the positive $\Delta^{17}O$-Mg# correlation. The case (1) is the addition of a ^{16}O-rich oxidizing agent to the ^{16}O-poor precursors, and the case (2) is the addition of a ^{16}O-poor

reducing agent to the ^{16}O-rich precursors. Hereafter, we discuss these two possible cases.

4.3. Case (1): addition of ^{16}O-rich oxidizing agent to the ^{16}O-poor precursors

For case (1), chondrules with Mg# of ~ 99 and Δ^{17}O of ~ +4‰, which are the higher end of the positive Δ^{17}O-Mg# correlation (Fig. 8a), may correspond to the ^{16}O-poor precursors. But such chondrule has not been observed in any other chondrites (Figs. 8b-e). On the other hand, water ice may correspond to the oxidizing agent, as is the case of chondrules in other carbonaceous chondrites (e.g., Tenner et al., 2015). Since the Δ^{17}O value at the lower end of the positive Δ^{17}O-Mg# correlation is ~ –4‰, water ice is required to have the Δ^{17}O value lower than –4‰. Nuth et al. (2012) suggested that ^{16}O-rich water ice can be produced by the Fischer-Tropsch reaction that converts CO into hydrocarbons by releasing the enriched ^{16}O back into the gas phase as water in the protoplanetary disk. However, water reaction products with ^{16}O-rich isotope ratios have not been found, while those with ^{16}O-poor isotope ratios have been observed; magnetite with Δ^{17}O of ~ +5‰ in ordinary chondrites (e.g., Choi et al., 1998) and cosmic symplectites with Δ^{17}O of ~ +80‰ in Acfer 094 (Sakamoto et al., 2007). Thus, the addition of ^{16}O-rich water ice to the ^{16}O-poor precursors is less likely as a cause of the positive Δ^{17}O-Mg# correlation (Fig. 8a).

4.4. Case (2): addition of ^{16}O-poor reducing agent to the ^{16}O-rich precursors

For case (2), chondrules with Mg# of ~ 96 and Δ^{17}O of ~ –4‰, which are the lower end of the positive Δ^{17}O-Mg# correlation (Fig. 8a), may correspond to the ^{16}O-rich precursors. Such chondrules are observed in Acfer 094 and CR chondrites (Ushikubo et al., 2012; Schrader et al., 2013). In the oxygen isotope mass balance model of Tenner et al. (2015), insoluble organic material (IOM) was included and considered to be an ^{16}O-poor reducing agent. In fact, Connolly et al. (1994) showed by heating experiments that forsteritic olivine with Fo_{99} could be produced from olivine with Fo_{94} and graphite or diamond, and Hashizume et al. (2011) showed IOM from a CR

chondrite had ^{16}O-poor isotope ratios ($\Delta^{17}O$ up to ~ +250‰).

What is envisioned during the heating of chondrule precursors along with carbon-rich organics are oxidation of carbon and reduction of chondrule melts. In the chondrule melts, carbon is oxidized and lost as CO or CO_2, which may result in mass-dependent oxygen isotope fractionation between the chondrules and oxidized carbon. Ash et al. (1998) reported that heating experiments of chondrule analogues with $\delta^{18}O$ of +6.5‰ and +7.5‰ and 5 wt% graphite produced reduced chondrule analogues with $\delta^{18}O$ of +5.6‰ and +6.3‰, indicating mass-dependent oxygen isotope fractionation of ~ 1‰ in $\delta^{18}O$ during reduction. Kita et al. (2010) calculated fractionation of $\delta^{18}O$ values between olivine plus pyroxene and CO. The difference in the $\delta^{18}O$ values of the two components ($\delta^{18}O_{Ol+Px} - \delta^{18}O_{CO}$) increase from ~ –2‰ to ~ –7‰ with decreasing temperature from 1900 °C to 800 °C. Likewise, lowered $\delta^{18}O$ values due to mass-dependent isotope fractionation are observed for the type I chondrules and FeO-poor fragments with high $\Delta^{17}O$ values of ~ +4‰ (Fig. 9). In Fig. 9, the deviation of $\delta^{18}O$ values from the PCM line ($\Delta^{18}O_{PCM}$) for the type I chondrules and their fragments in CH and CB chondrites are plotted along with the $\Delta^{17}O$ values. While many of the chondrules and the fragments have $\Delta^{18}O_{PCM}$ values distributing near the PCM line, those with high $\Delta^{17}O$ values have $\Delta^{18}O_{PCM}$ values deviated from the PCM line towards the low-$\delta^{18}O$ side exceeding the uncertainty. Similarly, chondrules with dusty olivine in CM chondrites show the $\delta^{18}O$ shifts from the PCM line (Schrader et al., 2020), which might also be due to mass-dependent oxygen isotope fractionation during reduction. Zhang et al. (2022) suggested that chondrules with oxygen isotope ratios plotting on or above the PCM line (i.e., negative $\Delta^{18}O_{PCM}$ values) are likely linked to ordinary chondrite-like materials. However, chondrules with negative $\Delta^{18}O_{PCM}$ values in CH and CB chondrites have higher $\Delta^{17}O$ values than the ordinary chondrite chondrules (Figs. 8 and 9) and are unlikely linked to ordinary chondrites. Thus, oxygen isotope ratios of the ^{16}O-poor chondrules and fragments are deviated from the PCM line towards low $\delta^{18}O$, which are likely to be the result of the mass-dependent oxygen isotope

fractionation between the chondrule melts and CO or CO_2. Estimation of $\delta^{18}O$ fractionation from the PCM line for the chondrules is described in the section 4.6.

During reduction of chondrule melts, metal-silicate segregation may have occurred. Chondrules with positive $\Delta^{17}O$ values contain Fe-particles in the olivine phenocrysts (Fig. 3), though abundances of the Fe-particles are lower than those in experimentally reduced olivine and dusty olivine in chondrules (e.g., Connolly et al., 1994; Leroux et al., 2003). TEM observations suggest that the Fe-particles are kamacite (Fig. 4f). The Ni concentrations in the Fe-particles are 2.5 ± 2.3 wt% on average, which are lower than those in isolated Fe-Ni metal grains in the inter-chondrule spaces of CH and CB chondrites (~ 4 – 14 wt%; e.g., Krot et al., 2002) and as low as those in Fe-particles embedded in olivine phenocrysts in chondrules from an ordinary chondrite (0.2 – 2.1 wt%; e.g., Leroux et al., 2003). It is therefore considered that the Fe-particles are Ni-poor Fe-metal. The Ni-poor Fe-metal (kamacite) is surrounded by silica-rich glass (Figs. 4b, 4c), of which occurrence is explained by reduction of FeO-bearing olivine according to the following reactions:

$$2(Mg,Fe)_2SiO_4 + C_{\text{ in organics}} = Mg_2SiO_4 + 2Fe_{\text{ in Ni-poor metal}} + SiO_{2\text{ in glass}} + CO_{2\text{ in gas}}$$

$$2(Mg,Fe)_2SiO_4 + 2C_{\text{ in organics}} = Mg_2SiO_4 + 2Fe_{\text{ in Ni-poor metal}} + SiO_{2\text{ in glass}} + 2CO_{\text{ in gas}}$$

Although it was expected that the CO or CO_2 was trapped in the vesicles, the Raman spectra on the regions with numerous vesicles showed no peak derived from CO or CO_2 vibration. Amounts of CO or CO_2 in vesicles might be too small to show the Raman peaks.

The high concentrations of CaO and Al_2O_3 in the silica-rich glass may be explained by a supply from the olivine phenocrysts (Table 4; Leroux et al., 2003). Unlike the grid-1 (Figs. 4b, 4c), silica-rich glass is not observed in the grid-2 though with vesicles and olivine dislocations (Fig. 4e), which is explained by short-circuit diffusion of silicon and oxygen through the dislocations

(Leroux et al., 2003).

The Fe-particle abundances in the olivine phenocrysts (Fig. 3; Supplementary Fig. A1) are lower than those in experimentally reduced olivine (Connolly et al., 1994; Leroux et al., 2003). Nevertheless, it is important that the hypothesis of an addition of carbon-rich organics as a ^{16}O-poor reducing agent can explain qualitatively multiple features observed in the porphyritic chondrules.

4.5. Approximate estimation of oxygen isotope ratios of the ^{16}O-poor organics

As discussed in the previous sections, the positive Δ^{17}O-Mg# correlation of the chondrules and fragments with Mg# > 96 in CH and CB chondrites (Fig. 8a) is likely to be explained by addition of ^{16}O-poor carbon-rich organics to the ^{16}O-rich precursors with Mg# of ~ 96 and Δ^{17}O of ~ –4‰. According to the mass balance model of Tenner et al. (2015), oxygen is also supplied from water ice with positive Δ^{17}O values and from ambient gas of solar composition with Δ^{17}O of –28.4‰. Water ice facilitates an increase of the Δ^{17}O values but serves as an oxidizing agent, and therefore the anhydrous precursor is preferable. The ambient gas facilitates reduction of the chondrule melt due to the high H/O ratio of ~ 2000 (Tenner et al., 2015) but suppresses an increase of the Δ^{17}O values, and therefore the low density of the ambient solar gas is preferable. In order to explain the positive Δ^{17}O-Mg# correlation, an ice-free environment with the thin ambient solar gas is required. Such a unique environment might be available in the regions with large disk heights where the gas density is low and gas temperature is high (exceeding H_2O sublimation temperature) compared to the midplane in the protoplanetary disk (e.g., Walsh et al., 2012). Chondrule formation at the large disk heights may be possible by, for instance, clumpy accretion (Boss and Graham, 1993) and magnetic winds (Salmeron and Ireland, 2012).

Assuming that the ^{16}O-poor Mg-rich chondrules with Mg# of ~ 99 and Δ^{17}O of ~ +4‰ formed from the anhydrous precursors composed of ^{16}O-rich silicate with Mg# of ~ 96 and Δ^{17}O of ~ –

4‰ and ^{16}O-poor carbon-rich organics, we briefly estimate the Δ^{17}O value of the organics based on the oxygen isotope mass balance model (Tenner et al., 2015) and results of reduction experiments of olivine (Connolly et al., 1994). Details of the estimation is described in the Supplementary text. When changing chondrule Mg# from 94 to 99, 5 – 10 wt% of carbon (graphite or diamond) may be required (Connolly et al., 1994), which corresponds to the organic fraction of 7 – 14 wt% assuming chondritic IOM with the elemental composition of ~ $C_{100}H_{75}O_{17.5}N_{3.5}S_{2.5}$ (Alexander et al., 2017). The organic fraction amounts to 6 – 11% of oxygen in the anhydrous precursors. The remaining fraction of 86 – 93 wt% is silicate, which amounts to 89 – 94% of oxygen in the anhydrous precursors. Using the fractions of oxygen from the two components, the equation (5) in Tenner et al. (2015), and the Δ^{17}O values of silicate (–4‰) and produced chondrules (+4‰), the Δ^{17}O values of organics are estimated as from ~ +90‰ to ~ +190‰ (Fig. 10a). The estimated Δ^{17}O values of organics are higher than those of IOM in CI and CM chondrites (0‰ to +10‰; Tartèse et al., 2018) but within the range of ^{16}O-poor IOM in a primitive CR chondrite (up to ~ +250‰; Hashizume et al., 2011) and therefore not impossibly high. The carbon fraction of 5 – 10 wt% from organics is higher than that from IOMs in carbonaceous chondrites (≲ 2 wt%; Alexander et al., 2017) and would be lower than that in cosmic dust such as ultracarbonaceous Antarctic micrometeorites (e.g., Dartois et al., 2013). Similar calculations with changing the elemental compositions of IOMs are carried out, and the Δ^{17}O values of organics are almost lower than the Δ^{17}O upper limit of the ^{16}O-poor IOM in a primitive CR chondrite (Hashizume et al., 2011) (Supplementary Figs. A3-4).

Without carbon-rich organics with high Δ^{17}O values like IOM in a primitive CR chondrite, the observed positive Δ^{17}O-Mg# correlation cannot be formed even if enrichment of carbon-rich organics occurred. If ^{16}O-poor IOM in a primitive CR chondrite (Hashizume et al., 2011) represents the oxygen isotopic compositions of carbon-rich organics in the outer and colder part of the protoplanetary disk, the occurrence of ^{16}O-poor Mg-rich porphyritic chondrules (Mg# ~ 99,

$\Delta^{17}O \sim +4‰$) in CH and CB chondrites suggests that these chondrules formed farther than where typical Mg-rich chondrules in carbonaceous chondrites formed.

4.6. Approximate estimation of $\delta^{18}O$ fractionation of the ^{16}O-poor chondrules

As discussed above, 7 – 14 wt% organics with $\Delta^{17}O$ of ~ +90‰ to +190‰ is required to form Mg-rich porphyritic chondrules with $\Delta^{17}O$ values of ~ +4‰ (Fig. 10a), which has $\Delta^{18}O_{PCM}$ values of ~ –4‰ as a result of mass-dependent oxygen isotope fractionation between chondrules and oxidized carbon (CO or CO_2) (Fig. 9). Here we estimate how much $\delta^{18}O$ fractionation from the PCM line occurs when adding ^{16}O-poor organics of 7 – 14 wt% (i.e., 5 – 10 wt% carbon) to ^{16}O-rich silicate.

Four assumptions are given for the estimation. (A) $\Delta^{18}O_{PCM}$ value before segregation between chondrules and oxidized carbon is 0‰. (B) $\delta^{18}O$ fractionation between chondrules and oxidized carbon (gas) ($\delta^{18}O_{Chd} - \delta^{18}O_{Gas}$) is –4‰. (C) Carriers of oxygen in chondrules are olivine and pyroxene. (D) 50% of oxygen in chondrules resides in olivine (i.e., 50% oxygen in pyroxene). As for the assumption (B), the $\delta^{18}O$ fractionation of –4‰ corresponds to that at temperatures of 1100 – 1200 °C (Kita et al., 2010). As for the assumption (C), reduced partition functions of olivine and pyroxene as well as CO are given in Kita et al. (2010) (Supplementary Table A5). Reduced partition functions of CO_2 are also calculated using the β factors in Richet et al. (1977) and procedure in Kita et al. (2010), so that $\delta^{18}O_{Chd} - \delta^{18}O_{CO}$ and $\delta^{18}O_{Chd} - \delta^{18}O_{CO2}$ are estimated. Details of assumptions and calculations are described in the Supplementary text.

With increasing the amount of ^{16}O-poor organics added to ^{16}O-rich silicate, the C/O atomic ratio increases (Fig. 10a). The C/O ratio is 0.24 – 0.49 in the range of 7 – 14 wt% organics (5 – 10 wt% carbon). Carbon combines with oxygen in chondrule melts and form CO and/or CO_2, which is isolated from chondrules or remains in vesicles. Fig. 10b estimates atomic ratios of remaining oxygen in chondrules to magnesium with variable C/O ratios in cases of CO and CO_2. In case of

oxygen loss by CO, the remaining-O/Mg ratios in the C/O range of 0.24 – 0.49 are within the range of O/Mg ratios of the bulk porphyritic chondrules in A-881020 obtained by defocused EPMA analyses. This indicates that ^{16}O-poor Mg-rich chondrules can be formed by adding ^{16}O-poor organics of 7 – 14 wt%. However, the remaining-O/Mg ratios in the C/O range of 0.24 – 0.49 are below the O/Mg range of the bulk porphyritic chondrules in case of oxygen loss by CO_2, which means chondrules may not be formed.

Oxygen isotope fractionation between chondrules and CO is shown in Fig. 10c, in which $\delta^{18}O_{Chd} - \delta^{18}O_{CO}$ is constantly –4‰ based on the assumption (B). With increasing C/O ratio, amount of oxygen residing in chondrules decreases and that in CO increases. Therefore, the $\Delta^{18}O_{Chd\text{-}CO}$ value shifts in a negative direction from 0‰ and $\Delta^{18}O_{CO\text{-}Chd}$ value shifts towards 0‰ with increasing C/O ratio. The $\Delta^{18}O_{Chd\text{-}CO}$ values in the C/O range of 0.24 – 0.49 are ~ –1‰ to ~ –2‰, which is smaller than the observed $\Delta^{18}O_{PCM}$ values of ~ –4‰ (Fig. 9). In case of fractionation between chondrules and CO_2, the slopes are steeper than those in case of CO (Fig. 10c). Even with the same C/O ratio, amount of oxygen residing in CO_2 is twice larger than that in CO, and amount of oxygen residing in chondrules is lower. The shift of $\Delta^{18}O_{Chd\text{-}CO2}$ is about twice larger than that in case of CO. The $\Delta^{18}O_{Chd\text{-}CO2}$ values in the C/O range of 0.24 – 0.49 are ~ –2‰ to ~ –4‰. The lower end is comparable to the observed $\Delta^{18}O_{PCM}$ values (Fig. 9). However, chondrules may not be formed due to the low remaining-O/Mg ratios (Fig. 10b). Thus, ^{16}O-poor Mg-rich chondrules with negative $\Delta^{18}O_{PCM}$ values can be formed by oxygen isotope fractionation with CO, though the $\Delta^{18}O_{Chd\text{-}CO}$ values are smaller than the observed $\Delta^{18}O_{PCM}$ values (Fig. 9). Additional fractionation could be caused by kinetic fractionation during chondrule formation (e.g., Richter, 2004). Similar results are obtained with changing the elemental compositions of IOMs (Supplementary Figs. A3-4).

In summary, the porphyritic chondrules in CH and CB chondrites are characterized by smaller sizes (Fig. 1) than those in other chondrite chondrules and similar bulk chemistry (Fig. 2) and

textures to those in other chondrite chondrules. In terms of oxygen isotope systematics, the Mg-rich porphyritic chondrules in CH and CB chondrites require a unique formation environment. The Mg-rich porphyritic chondrules formed from anhydrous precursors composed of ^{16}O-rich silicate and ^{16}O-poor carbon-rich organics in the regions with large disk heights where the gas density is low and gas temperature is high. This is a new environment for chondrule formation and cannot be applicable to chondrules in other chondrites and even to non-porphyritic chondrules in CH and CB chondrites, as the chondrules show negative Δ^{17}O-Mg# trends (Fig. 8). Thus, CH and CB chondrites sampled chondrules that formed in entirely different formation environments.

4.7. Non-porphyritic chondrules and lithic fragments that may have formed along with the porphyritic chondrules

In CH and CB chondrites, there are non-porphyritic chondrules and lithic fragments that are not classified into the three groups in Δ^{17}O values (+1.4‰, –2.3‰, and –6.3‰), and Nakashima et al. (2020) suggested that several of the ungrouped objects formed along with the porphyritic chondrules. The magnesian CC chondrule (Ch01; Nakashima et al., 2011) has the Δ^{17}O value of +2.2 ± 0.1‰, Mg# of 98.7 (Fig. 8a), and the negative $\Delta^{18}O_{PCM}$ value (Fig. 9). The silica-bearing lithic fragment (F37; Nakashima et al., 2020) has the Δ^{17}O value of –3.4 ± 0.2‰, Mg# of 95.1, and the $\Delta^{18}O_{PCM}$ value close to 0‰ (Figs. 8a and 9). Therefore, it is likely that the two FeO-poor objects formed along with the type I porphyritic chondrules in the same event. The FeO-rich radial pyroxene chondrule (C32; Nakashima et al., 2020) has the Δ^{17}O value of –1.1 ± 0.3‰, which is within the Δ^{17}O range of type II chondrules and FeO-rich fragments (Fig. 8a). On the other hand, two FeO-rich silica-bearing lithic fragments (F38 and F39; Nakashima et al., 2020) have the Δ^{17}O values outside of the Δ^{17}O range of type II chondrules and FeO-rich fragments (Fig. 8a). Therefore, it is likely that the FeO-rich radial pyroxene chondrule formed along with type II porphyritic chondrules, but the two FeO-rich silica-bearing lithic fragments may have formed in distinct

environments.

5. Conclusions

We analyzed oxygen isotope ratios and elemental compositions of porphyritic chondrules and olivine and pyroxene fragments in the A-881020 CH chondrite to investigate the oxygen isotope systematics of the porphyritic chondrules in CH and CB chondrites. The oxygen isotope ratios are homogeneous within the uncertainty inside the porphyritic chondrules, except for relict grains of olivine and low-Ca pyroxene with distinct oxygen isotope ratios. The average oxygen isotope ratios of the individual chondrules plot along and above the PCM line with $\Delta^{17}O$ values from –4.7‰ to +4.1‰. The olivine and pyroxene fragments, of which $\Delta^{17}O$ values range from –2.1‰ to +3.2‰, are likely to be fragments of the porphyritic chondrules.

Type I and II chondrules including FeO-poor and -rich fragments do not show a systematic difference in the $\Delta^{17}O$ values, unlike the non-porphyritic chondrules in CH and CB chondrites and chondrules in other carbonaceous chondrites. For the chondrules and their fragments with Mg# < 96, the $\Delta^{17}O$ values increase with decreasing Mg#, similarly to the type II chondrules in CR and Tagish Lake-type chondrites. The type II chondrules in CH and CB chondrites may have formed in a similar environment to that for type II chondrules in CR and Tagish Lake-type chondrites (e.g., Tenner et al., 2015). The $\Delta^{17}O$ values of the type I chondrules and fragments increase from –4.7‰ to +4.1‰ with increasing Mg# from 96 to 99. The positive $\Delta^{17}O$-Mg# correlation may be explained by an addition of ^{16}O-poor organics as a reducing agent to the relatively ^{16}O-rich silicate in the regions with large disk heights where the gas density is low and gas temperature is high. This is a new environment for chondrule formation. This hypothesis is supported by the two lines of evidence. (1) Oxygen isotope ratios of the ^{16}O-poor chondrules and fragments deviate from the PCM line towards low $\delta^{18}O$, while those of the relatively ^{16}O-rich chondrules and fragments are distributed around the PCM line. The $\delta^{18}O$ deviations are likely to be the result of the oxygen

isotope mass fractionation between the chondrules and CO or CO_2. (2) The porphyritic chondrules contain Ni-poor Fe-metal particles surrounded by silica-rich glass in the olivine phenocrysts, which are likely to be reduction products during the chondrule formation. Thus, the Mg-rich porphyritic chondrules in CH and CB chondrites may have formed in the different formation environment from any other chondrite chondrules including non-porphyritic chondrules in CH and CB chondrites.

Data Availability

Data are available through Mendeley Data at https://doi.org/10.17632/4bpgnwmxh5.1.

Acknowledgements

The authors thank NIPR for use of A-881020 thin section for this study, J. Kern and T. J. Tenner for SIMS support, J. Fournelle for EPMA support at UW-Madison, and Sasha Krot for kindly providing oxygen isotope data of SO chondrules in metal-rich carbonaceous chondrites. K. Yamada helped to conduct EPMA analyses at Ibaraki University. A. Yamaguchi helped to conduct EPMA analyses at NIPR. Reviews of E. van Kooten and two anonymous reviewers significantly improved the manuscript. This work was supported by JSPS KAKENHI grant number 18H01263 (D.N.) and the NASA Cosmochemistry program (NNX11AG62G). WiscSIMS is partly supported by NSF (EAR10-53466, EAR-1658823).

Appendix A. Supplementary material

This supplementary material consists of an excel file and two PDF files. The excel file contains table A1 (elemental compositions of porphyritic chondrules and olivine and pyroxene fragments), table A2 (raw SIMS measured oxygen isotope data), table A3 (instrumental bias of SIMS analysis), and table A4 (oxygen isotope ratios and Mg# of individual spots in porphyritic chondrules). One of the two PDF files contains figure A1 (oxygen isotope ratios of individual spots

in porphyritic chondrules and BSE images of porphyritic chondrules and olivine and pyroxene fragments). Another PDF file contains a text describing details of estimations of $\Delta^{17}O$ values in organics and $\delta^{18}O$ fractionation of ^{16}O-poor chondrules, table A5 (oxygen isotope fractionation between chondrules and CO_2 and CO), figure A2 (comparison of $\delta^{18}O$ values between olivine, low-Ca pyroxene, and glass in the same chondrules), figure A3 ($\Delta^{17}O$ values of organics, remaining-O/Mg ratios, and $\Delta^{18}O_{PCM}$ values of chondrules in case of Orgueil IOM), and figure A4 ($\Delta^{17}O$ values of organics, remaining-O/Mg ratios, and $\Delta^{18}O_{PCM}$ values of chondrules in case of CHON particles).

References

Alexander C. M. O'D., Cody G. D., De Gregorio B. T., Nittler L. R., and Stroud R. M. (2017) The nature, origin and modification of insoluble organic matter in chondrites, the major source of Earth's C and N. *Chem. Erde* **77**, 227–256.

Anders E. and Gerevesse N. (1989) Abundances of the elements: Meteoritic and solar. *Geochim. Cosmochim. Acta* **53**, 197–214.

Ash R. D., Connolly, Jr., H. C., Alexander C. M. O'D., MacPherson G. J., and Rumble, III, D. (1998) Oxygen isotope ratios of natural and synthetic chondrules: evidence for in situ reduction by carbon. *Meteorit. Planet. Sci.* **33**(Suppl.), A11 (abstr.).

Boss A. P. and Graham J. A. (1993) Clumpy disk accretion and chondrule formation. *Icarus* **106**, 168-178.

Chaumard N., Defouilloy C., and Kita N. T. (2018) Oxygen isotope systematics of chondrules in the Murchison CM2 chondrite and implications for the CO–CM relationship. *Geochim. Cosmochim. Acta* **228**, 220–242.

Chaumard N., Defouilloy C., Hertwig A. T., and Kita N. T. (2021) Oxygen isotope systematics of chondrules in the Paris CM2 chondrite: Indication for a single large formation region across

snow line. *Geochim. Cosmochim. Acta* **299**, 199–218.

Choi B. G., McKeegan K. D., Leshin L. A., and Wasson J. T. (1998) Extreme oxygen-isotope compositions in magnetite from unequilibrated ordinary chondrites. *Nature* **392**, 577–579.

Clayton R. N., Onuma N., Grossman L., and Mayeda T. K. (1977) Distribution of the pre-solar component in Allende and other carbonaceous chondrites. *Earth Planet. Sci. Lett.* **34**, 209–224.

Connolly, Jr., H. C. and Huss G. R. (2010) Compositional evolution of the protoplanetary disk: Oxygen isotopes of type-II chondrules from CR2 chondrites. *Geochim. Cosmochim. Acta* **74**, 2473–2483.

Connolly, Jr., H. C., Hewins R. H., Ash R. D., Zanda B., Lofgren G. E., and Bourot-Denise M. (1994) Carbon and the formation of reduced chondrules. *Nature* **371**, 136-139.

Dartois E., Engrand C., Brunetto R., Duprat J., Pino T., Quirico E., Remusat L., Bardin N., Briani G., Mostefaoui S., Morinaud G., Crane B., Szwec N., Delauche L., Jamme F., Sandt Ch., and Dumas P. (2013) UltraCarbonaceous Antarctic micrometeorites, probing the Solar System beyond the nitrogen snow-line. *Icarus* **224**, 243-252.

Davidson J., Krot A. N., Nagashima K., Hellebrand E., and Lauretta D. S. (2014) Oxygen isotope and chemical compositions of magnetite and olivine in the anomalous CK3 Watson 002 and ungrouped Asuka-881595 carbonaceous chondrites: Effects of parent body metamorphism. *Meteorit. Planet. Sci.* **49**, 1456–1474.

Ebel D. S. and Grossman L. (2000) Condensation in dust-enriched systems. *Geochim. Cosmochim. Acta* **64**, 339–366.

Friedrich J.M., Weisberg M. K., Ebel D. S., Biltz A. E., Corbett B. M., Iotzov I. V., Khan W. S., and Wolman M. D. (2014) Chondrule size and related physical properties: A compilation and evaluation of current data across all meteorite groups. *Chem. Erde* **75**, 419–443.

Fukuda K., Tenner T. J., Kimura M., Tomioka N., Siron G., Ushikubo T., Chaumard N., Hertwig A. T., and Kita N. T. (2022) A temporal shift of chondrule generation from the inner to outer

Solar System inferred from oxygen isotopes and Al-Mg chronology of chondrules from primitive CM and CO chondrites. *Geochim. Cosmochim. Acta* **322**, 194–229.

Gardinier A., Derenne S., Robert F., Behar F., Largeau C., and Maquet, J. (2000) Solid state CP/MAS ^{13}C NMR of the insoluble matter of the Orgueil and Murchison meteorites: quantitative study. *Earth Planet. Sci. Lett.* **184**, 9–21.

Gooding J. L. and Keil K. (1981) Relative abundances of chondrule primary textural types in ordinary chondrites and their bearing on conditions of chondrule formation. *Meteoritics* **16**, 17–42.

Grossman J. N., Rubin A. E., and MacPherson G. J. (1988) ALH85085: a unique volatile-poor carbonaceous chondrite with possible implications for nebular fractionation processes. *Earth Planet. Sci. Lett.* **91**, 33–54.

Hardis R., Jessop J. L. P., Peters F. E., and Kessler R. (2013) Cure kinetics characterization and monitoring of an epoxy resin using DSC, Raman spectroscopy, and DEA. *Compos. Part A* **49**, 100-108.

Hashizume K., Takahata N., Naraoka H., and Sano Y. (2011) Extreme oxygen isotope anomaly with a solar origin detected in meteoritic organics. *Nat. Geosci.* **4**, 165–168.

Heck P. R., Ushikubo T., Schmitz B., Kita N. T., Spicuzza M. J., and Valley J. W. (2010) A single asteroidal source for extraterrestrial Ordovician chromite grains from Sweden and China: High-precision oxygen three-isotope SIMS analysis. *Geochim. Cosmochim. Acta* **74**, 497–509.

Hertwig A. T., Defouilloy C., and Kita N. T. (2018) Formation of chondrules in a moderately high dust enriched disk: Evidence from oxygen isotopes of chondrules from the Kaba CV3 chondrite. *Geochim. Cosmochim. Acta* **224**, 116–131.

Hertwig A. T., Kimura M., Ushikubo T., Defouilloy C., and Kita N. T. (2019a) The ^{26}Al-^{26}Mg systematics of FeO-rich chondrules from Acfer 094: two chondrule generations distinct in age and oxygen isotope ratios. *Geochim. Cosmochim. Acta* **253**, 111–126.

Hertwig A. T., Kimura M., Defouilloy C., and Kita N. T. (2019b) Oxygen isotope systematics of chondrule olivine, pyroxene, and plagioclase in one of the most pristine $CV3_{Red}$ chondrites (Northwest Africa 8613). *Metorit. Planet. Sci.* **54**, 2666–2685.

Hezel D. C. and Palme H. (2010) The chemical relationship between chondrules and matrix and the chondrule matrix complementarity. *Earth Planet. Sci. Lett.* **294**, 85–93.

Hutcheon I. D., Marhas K. K., Krot A. N., Goswami J. N., and Jones R. H. (2009) ^{26}Al in plagioclase-rich chondrules in carbonaceous chondrites: evidence for an extended duration of chondrule formation. *Geochim. Cosmochim. Acta* **73**, 5080–5099.

Ikeda Y. (1980) Petrology of Allan Hills-764 chondrite (LL3). *Mem. Natl. Inst. Polar Res. Spec.* **17**, 50-82.

Jones R. H., Grossman J. N., and Rubin A. E. (2005) Chemical, mineralogical and isotopic properties of chondrules: Clues to their origin. In *Chondrules and the Protoplanetary Disk* (eds. A. N. Krot, E. R. D. Scott, and B. Reipurth). ASP Conference Series 341, Astronomical Society of the Pacific, San Francisco. pp. 251–285.

Jones R. H. (2012) Petrographic constraints on the diversity of chondrule reservoirs in the protoplanetary disk. *Meteorit. Planet. Sci.* **47**, 1176–1190.

Joswiak D. J., Nakashima D., Brownlee D. E., Matrajt G., Ushikubo T., Kita N. T., Messenger S., and Ito M. (2014) Terminal particle from Stardust track 130: Probable Al-rich chondrule fragment from comet Wild 2. *Geochim. Cosmochim. Acta* **144**, 277–298.

Kimura M. and Ikeda Y. (1995) Anhydrous alteration of Allende chondrules in the solar nebula II: Alkali-Ca exchange reactions and formation of nepheline, sodalite and Ca-rich phases in chondrules. *Proc. NIPR Symp. Antarc. Meteorites* **8**, 123-138.

Kissel J. and Krueger F. R. (1987) The organic component in dust from comet Halley as measured by the PUMA mass spectrometer on board Vega 1. *Nature* **326**, 755–760.

Kita N. T., Nagahara H., Togashi S., and Morishita Y. (2000) A short duration of chondrule

formation in the solar nebula: Evidence from ^{26}Al in Semarkona ferromagnesian chondrules. *Geochim. Cosmochim. Acta* **64**, 3913–3922.

Kita N. T., Ushikubo T., Fu B., and Valley J. W. (2009) High precision SIMS oxygen isotope analysis and the effect of sample topography. *Chem. Geol.* **264**, 43–57.

Kita N. T., Nagahara H., Tachibana S., Tomomura S., Spicuzza M. J., Fournelle J. H., and Valley J. W. (2010) High precision SIMS oxygen three isotope study of chondrules in LL3 chondrites: Role of ambient gas during chondrule formation. *Geochim. Cosmochim. Acta* **74**, 6610–6635.

Kita N. T. and Ushikubo T. (2012) Evolution of protoplanetary disk inferred from ^{26}Al chronology of individual chondrules. *Meteorit. Planet. Sci.* **47**, 1108–1119.

Kita N. T., Tenner T. J., Defouilloy C., Nakashima D., Ushikubo T., and Bischoff A. (2015) Oxygen isotope systematics of chondrules in R3 clasts: a genetic link to ordinary chondrites. *Lunar Planet. Sci. Conf.* **46**, 2053.

Krot A. N., Petaev M. I., Scott E. R. D., Choi B.-G., Zolensky M. E., and Keil K. (1998) Progressive alteration in CV3 chondrites: more evidence for asteroidal alteration. *Meteorit. Planet. Sci.* **33**, 1065–1085.

Krot A. N., McKeegan K. D., Russell S. S., Meibom A., Weisberg M. K., Zipfel J., Krot T. V., Fagan T. J., and Keil K. (2001) Refractory Ca, Al-rich inclusions and Al-diopside-rich chondrules in the metal-rich chondrites Hammadah al Hamra 237 and QUE 94411. *Meteorit. Planet. Sci.* **36**, 1189–1217.

Krot A. N., Meibom A., Weisberg M. K., and Keil K. (2002) The CR chondrite clan: Implications for early solar system processes. *Meteorit. Planet. Sci.* **37**, 1451–1490.

Krot A. N., Ivanova M. A., and Ulyanov A. A. (2007) Chondrules in the CB/CH-like carbonaceous chondrite Isheyevo: Evidence for various chondrule-forming mechanisms and multiple chondrule generations. *Chem. Erde* **67**, 283–300.

Krot A. N., Nagashima K., Yoshitake M., and Yurimoto H. (2010) Oxygen isotopic compositions

of chondrules from the metal-rich chondrites Isheyevo (CH/CB$_b$), MAC 02675 (CB$_b$) and QUE 94627 (CB$_b$). *Geochim. Cosmochim. Acta* **74**, 2190–2211.

Krot A. N., Nagashima K., and Petaev M. I. (2012) Isotopically uniform, ^{16}O-depleted calcium, aluminum-rich inclusions in CH and CB carbonaceous chondrites. *Geochim. Cosmochim. Acta* **83**, 159–178.

Krot A. N. and Nagashima K. (2017) Constraints on mechanisms of chondrule formation from chondrule precursors and chronology of transient heating events in the protoplanetary disk. *Geochem. J.* **51**, 45–68.

Krot A. N., Petaev M. I., Nagashima K., Dobrică E., Johnson B. C., and Cashion M. D. (2021) Impact plume-formed and protoplanetary disk high-temperature components in CB and CH metal-rich carbonaceous chondrites. *Meteorit. Planet. Sci.* **57**, 352–380.

Kurahashi E., Kita N. T., Nagahara H., and Morishita Y. (2008) ^{26}Al–^{26}Mg systematics of chondrules in a primitive CO chondrite. *Geochim. Cosmochim. Acta* **72**, 3865–3882.

Leroux H., Libourel G., Lemelle L., and Guyot F. (2003) Experimental study and TEM characterization of dusty olivines in chondrites: Evidence for formation by in situ reduction. *Meteorit. Planet. Sci.* **38**, 81–94.

Libourel G., Nagashima K., Portail M., and Krot A. N. (2023) On the significance of oxygen-isotope variations in chondrules from carbonaceous chondrites. *Geochim. Cosmochim. Acta* **346**, 102–120.

Marrocchi Y., Villeneuve J., Batanova V., Piani L., and Jacquet E. (2018) Oxygen isotopic diversity of chondrule precursors and the nebular origin of chondrules. *Earth Planet. Sci. Lett.* **496**, 132–141.

Marrocchi Y., Euverte R., Villeneuve J., Batanova V., Welsch B., Ferrière L., and Jacquet E. (2019) Formation of CV chondrules by recycling of amoeboid olivine aggregate-like precursors. *Geochim. Cosmochim. Acta* **247**, 121–141.

Marrocchi Y., Avice G., and Barrat J.-A. (2021) The Tarda meteorite: a window into the formation of D-type asteroids. *Astrophys. J.* **913**, L9.

Marrocchi Y., Piralla M., Regnault M., Batanova V., Villeneuve J., and Jacquet E. (2022) Isotopic evidence for two chondrule generations in CR chondrites and their relationships to other carbonaceous chondrites. *Earth Planet. Sci. Lett.* **593**, 117683.

Marrocchi Y., Longeau A., Goupil R. L., Dijon V., Pinto G., Neukampf J., Villeneuve J., Jacquet E. (2024) Isotopic evolution of the inner solar system revealed by size-dependent oxygen isotopic variations in chondrules. *Geochim. Cosmochim. Acta* **371**, 52–64.

Nagashima K., Krot A. N., and Huss G. R. (2014) ^{26}Al in chondrules from CR2 chondrites. *Geochem. J.* **48**, 561–570.

Nagashima K., Krot A. N., and Huss G. R. (2015) Oxygen-isotope compositions of chondrule phenocrysts and matrix grains in Kakangari K-grouplet chondrite: Implication to a chondrule-matrix genetic relationship. *Geochim. Cosmochim. Acta* **151**, 49–67.

Nagashima K., Krot A. N., and Komatsu M. (2017) ^{26}Al–^{26}Mg systematics in chondrules from Kaba and Yamato 980145 CV3 carbonaceous chondrites. *Geochim. Cosmochim. Acta* **201**, 303–319.

Nagashima K., Kita N. T., and Luu T.-H. (2018) In *Chondrules: Records of Protoplanetary Disk Processes* (eds. S. S. Russell, H. Connolly and A. N. Krot). Cambridge University Press, Cambridge U.K, pp. 247–275.

Nakamura T., Noguchi T., and Akaki T. (2006) Mineralogy and oxygen isotope signatures of the Asuka 881020 CH chondrite. *Meteorit. Planet. Sci.* **41**(Suppl.), A128 (abstr.).

Nakamura T., Noguchi T., Tsuchiyama A., Ushikubo T., Kita N. T., Valley J. W., Zolensky M. E., Kakazu Y., Sakamoto K., Mashio E., Uesugi K., and Nakano T. (2008) Chondrulelike objects in short-period comet 81P/Wild 2. *Science* **321**, 1664–1667.

Nakashima D., Ushikubo T., Rudraswami N. G., Kita N. T., Valley J. W., and Nagao K. (2011) Ion

microprobe analyses of oxygen three-isotope ratios of chondrules from the Sayh al Uhaymir 290 CH chondrite using a multiple-hole disk. *Meteorit. Planet. Sci.* **46**, 857–874.

Nakashima D., Ushikubo T., Joswiak D. J., Brownlee D. E., Matrajt G., Weisberg M. K., Zolensky M. E., and Kita N. T. (2012) Oxygen isotopes in crystalline silicates of comet Wild 2: a comparison of oxygen isotope systematics between Wild 2 particles and chondritic materials. *Earth Planet. Sci. Lett.* **357–358**, 355–365.

Nakashima D., Kimura M., Yamada K., Noguchi T., Ushikubo T., and Kita N. (2020) Oxygen isotope study of the Asuka-881020 CH chondrite I: Non-porphyritic chondrules. *Geochim. Cosmochim. Acta* **290**, 180–200.

Noguchi T., Imae N., and Kimura M. (2004) Petrology and mineralogy of Asuka 881020: A preliminary report of the first CH chondrite found among the Japanese Antarctic meteorite collection. In *Proc. NIPR Symp. Antarct. Meteorites*, **28**, 62–63 (abstr.).

Noguchi T., Ohashi N., Tsujimoto S., Mitsunari T., Bradley J. P., Nakamura T., Toh S., Stephan T., Iwata N. and Imae N. (2015) Cometary dust in Antarctic ice and snow: past and present chondritic porous micrometeorites preserved on the Earth's surface. *Earth Planet. Sci. Lett.* **410**, 1–11.

Nuth J. A., Paquette J. A., and Farquhar A. (2012) Can lightning produce significant levels of mass-independent oxygen isotopic fractionation in nebular dust? *Meteorit. Planet. Sci.* **47**, 2056–2069.

Ogliore R. C., Huss G. R., Nagashima K., Butterworth A. I., and Gainsforsth Z. (2012) Incorporation of a late-forming chondrule into comet Wild 2. *Astrophys. J. Lett.* **745**, L19.

Pinto G. A., Jacquet E., Corgne A., Olivares F., Villeneuve J., and Marrocchi Y. (2024) Deciphering recycling processes during solar system evolution from magnesium-rich relict olivine grains in type II chondrules. *Geochim. Cosmochim. Acta* **364**, 65–78.

Piralla M., Villeneuve J., Batanova V., Jacquet E., and Marrocchi Y. (2021) Conditions of

chondrule formation in ordinary chondrites. *Geochim. Cosmochim. Acta* **313**, 295–312.

Piralla M., Villeneuve J., Schnuriger N., Bakaert D. V., and Marrocchi Y. (2023) A unified chronology of dust formation in the early solar system. *Icarus* **394**, 115427.

Richet R., Bottinga Y., and Javoy M. (1977) A review of hydrogen, carbon, nitrogen, oxygen, sulphur, and chlorine stable isotope fractionation among gaseous molecules. *Ann. Rev. Earth Planet. Sci.* **5**, 65-110.

Richter F. M. (2004) Timescales determining the degree of kinetic isotope fractionation by evaporation and condensation. *Geochim. Cosmochim. Acta* **68**, 4971–4992.

Rudraswami N. G., Ushikubo T., Nakashima D., and Kita N. T. (2011) Oxygen isotope systematics of chondrules in Allende CV3 chondrite: High precision ion microprobe studies. *Geochim. Cosmochim. Acta* **75**, 7596–7611.

Russell S. D. J., Longstaffe F. J., King P. L., and Larson T. E. (2010) The oxygen-isotope composition of chondrules and isolated forsterite and olivine grains from the Tagish Lake carbonaceous chondrite. *Geochim. Cosmochim. Acta* **74**, 2428–2499.

Sakamoto N., Seto Y., Itoh S., Kuramoto K., Fujino K., Nagashima K., Krot A. N., and Yurimoto H. (2007) Remnants of the early solar system water enriched in heavy oxygen isotopes. *Science* **317**, 231–233.

Salmeron R. and Ireland T. R. (2012) Formation of chondrules in magnetic winds blowing through the proto-asteroid belt. *Earth Planet. Sci. Lett.* **327-328**, 61–67.

Schrader D. L., Connolly, Jr., H. C., Lauretta D. S., Nagashima K., Huss G. R., Davidson J., and Domanik K. J. (2013) The formation and alteration of the Renazzo-like carbonaceous chondrites II: linking O-isotope composition and oxidation state of chondrule olivine. *Geochim. Cosmochim. Acta* **101**, 302–327.

Schrader D. L., Nagashima K., Krot A. N., Ogliore R. C., and Hellebrand E. (2014) Variations in the O-isotope compositions of gas during the formation of chondrules from the CR chondrites.

Geochim. Cosmochim. Acta **132**, 50–74.

Schrader D. L., Nagashima K., Krot A. N., Ogliore R. C., Yin Q.-Z., Amelin Y. A., Stirling C. H., and Kaltenbach A. (2017) Distribution of ^{26}Al in the CR chondrite chondrule-forming region of the protoplanetary disk. *Geochim. Cosmochim. Acta* **201**, 275–302.

Scott E. R. D. (1988) A new kind of primitive chondrite, Allan Hills 85085. *Earth Planet. Sci. Lett.* **91**, 1–18.

Scott E. R. D. and Krot A. N. (2003) Chondrites and their components. In *Meteorites, Comets, and Planets,* vol. 1, edited by A. M. Davis, pp. 143-200. Treatise on Geochemistry, edited by H. D. Holland and K. K. Turekian. Elsevier B. V., Amsterdam.

Simon J. I., Hutcheon I. D., Simon S. B., Matzel J. E. P., Ramon E. C., Weber P. K., Grossman L., and Depaolo D. J. (2011) Oxygen isotope variations at the margin of a CAI records circulation within the solar nebula. *Science* **331**, 1175–1178.

Siron G., Fukuda K., Kimura M., and Kita N. T. (2021) New constraints from ^{26}Al–^{26}Mg chronology of anorthite-bearing chondrules in unequilibrated ordinary chondrites. *Geochim. Cosmochim. Acta* **293**, 103–126.

Siron G., Fukuda K., Kimura M., and Kita N. T. (2022) High precision ^{26}Al-^{26}Mg chronology of chondrules in unequilibrated ordinary chondrites: Evidence for restricted formation ages. *Geochim. Cosmochim. Acta* **324**, 312–345.

Tartèsea R., Chaussidon M., Gurenko A., Delarue F., and Robert F. (2018) Insights into the origin of carbonaceous chondrite organics from their triple oxygen isotope composition. *Proc. Natl. Acad. Sci. USA* **115**, 8535–8540.

Tenner T. J., Ushikubo T., Kurahashi E., Nagahara H., and Kita N. T. (2013) Oxygen isotope systematics of chondrule phenocrysts from the CO3.0 chondrite Yamato 81020: evidence for two distinct oxygen isotope reservoirs. *Geochim. Cosmochim. Acta* **102**, 226–245.

Tenner T. J., Nakashima D., Ushikubo T., Kita N. T., and Weisberg M. K. (2015) Oxygen isotope

ratios of FeO-poor chondrules in CR3 chondrites: Influence of dust enrichment and H_2O during chondrule formation. *Geochim. Cosmochim. Acta* **148**, 228–250.

Tenner T. J., Kimura M., and Kita N. T. (2017) Oxygen isotope characteristics of chondrules from the Yamato-82094 ungrouped carbonaceous chondrite: Further evidence for common O-isotope environments sampled among carbonaceous chondrites. *Meteorit. Planet. Sci.* **52**, 268–294.

Tenner T. J., Ushikubo T., Nakashima D., Schrader D. L., Weisberg M. K., Kimura M., and Kita N. T. (2018) Oxygen isotope characteristics of chondrules from recent studies by secondary ion mass spectrometry. In *Chondrules: Records of Protoplanetary Disk Processes,* edited by S. S. Russell, H. C. Connolly Jr., and A. N. Krot, pp. 196 – 246. Cambridge Planetary Science, edited by F. Bagenal, D. Jewitt, C. Murray, J. Bell, R. Lorenz, F. Nimmo, S. Russell. Cambridge University Press.

Tenner T. J., Nakashima D., Ushikubo T., Tomioka N., Kimura M., Weisberg M. K., and Kita N. T. (2019) Extended chondrule formation intervals in distinct physicochemical environments: Evidence from Al-Mg isotope systematics of CR chondrite chondrules with unaltered plagioclase. *Geochim. Cosmochim. Acta* **260**, 133–160.

Ushikubo T., Kimura M., Kita N. T., and Valley J. W. (2012) Primordial oxygen isotope reservoirs of the solar nebula recorded in chondrules in Acfer 094 carbonaceous chondrite. *Geochim. Cosmochim. Acta* **90**, 242–264.

Ushikubo T., Nakashima D., Kimura M., Tenner T. J., and Kita N. T. (2013) Contemporaneous formation of chondrules in distinct oxygen isotope reservoirs. *Geochim. Cosmochim. Acta* **109**, 280–295.

Ushikubo T. and Kimura M. (2021) Oxygen-isotope systematics of chondrules and olivine fragments from Tagish Lake C2 chondrite: Implications of chondrule-forming regions in protoplanetary disk. *Geochim. Cosmochim. Acta* **293**, 328–343.

Valley J. W. and Kita N. T. (2009) In situ Oxygen Isotope Geochemistry by Ion Microprobe.

Mineralogical Association of Canada Short Course vol. **41**, 19–63.

Villeneuve J., Chaussidon M., and Libourel G. (2009) Homogeneous distribution of ^{26}Al in the solar system from the Mg isotopic composition of chondrules. Science 325, 985-988.

Walsh C., Nomura H., Millar T. J., and Aikawa Y. (2012) Chemical processes in protoplanetary disks. II. On the importance of photochemistry and X-ray ionization. *Astrophys. J.* **74**, 114.

Weisberg M. K., Ebel D. S., Connolly, Jr., H. C., Kita N. T. and Ushikubo T. (2011) Petrology and oxygen isotope compositions of chondrules in E3 chondrites. *Geochim. Cosmochim. Acta* **75**, 6556–6569.

Weisberg M. K., Ebel D. S., Nakashima D., Kita N. T., and Humayun M. (2015) Petrology and geochemistry of chondrules and metal in NWA 5492 and GRO 95551: A new type of metal-rich chondrite. *Geochim. Cosmochim. Acta* **167**, 256–285.

Weisberg M. K., Kita N. T., Fukuda K., Siron G., and Ebel D. S. (2021) Micro-distribution of oxygen isotopes in unequilibrated enstatite chondrites. *Geochim. Cosmochim. Acta* **300**, 279–295.

Williams C. D., Sanborn M. E., Defouilloy C., Yin Q.-Z., Kita N. T., Ebel D. S., Yamakawa A., and Yamashita K. (2020) Chondrules reveal large-scale outward transport of inner Solar System materials in the protoplanetary disk. *Proc. Natl. Acad. Sci. U. S. A.* **117**, 23426–23435.

Yamanobe M., Nakamura T., and Nakashima D. (2018) Oxygen isotope reservoirs in the outer asteroid belt inferred from oxygen isotope systematics of chondrule olivines and isolated forsterite and olivine grains in Tagish Lake-type carbonaceous chondrites, WIS 91600 and MET 00432. *Polar Sci.* **15**, 29–38.

Zanda B., Bourot-Denise M., Perron C., and Hewins R. H. (1994) Origin and metamorphic redistribution of silicon, chromium, and phosphorous in the metal of chondrites. *Science* **265**, 1846–1849.

Zhang M., Fukuda K., Spiccuza M. J., Siron G., Heimann A., Hammerstrom A. J., Kita N. T.,

Ushikubo T., and Valley J. W. (2022) SIMS matrix effects in oxygen isotope analysis of olivine and pyroxene: Application to Acfer 094 chondrite chondrules and reconsideration of the primitive chondrule minerals (PCM) line. *Chem. Geol.* **608**, 121016.

Table 1. Average oxygen isotope ratios of individual porphyritic chondrules in Asuka-881020.

Chondrule		Ol[a]	Lpx	Int. px	Hpx	Pl	Sil	Gl	15 μm[b]	4 μm	$\delta^{18}O \pm 2\sigma$ (‰)		$\delta^{17}O \pm 2\sigma$ (‰)		$\Delta^{17}O \pm 2\sigma$ (‰)		Mg# ± 1SD		$\Delta^{18}O_{PCM} \pm 2\sigma$ (‰)	
C38		3	0	0	0	0	0	1	3	1	9.97	0.47	8.41	0.51	3.23	0.54	97.7	1.6	-2.72	1.33
C39		2	3	0	0	0	0	0	2	3	9.66	1.59	7.51	1.51	2.52	0.78	97.4	1.7	-1.51	2.34
C40		1	2	0	0	0	0	1	2	2	10.95	0.75	9.73	0.57	4.11	0.54	98.4	0.2	-3.64	1.46
	Relict	1	0	0	0	0	0	0	1	0	1.57	0.19	-1.43	0.35	-2.25	0.31	98.5			
C41		2	1	0	0	0	0	0	3	0	10.43	0.55	8.96	0.54	3.54	0.28	98.2	0.3	-2.92	0.92
	Relict	1	1	0	0	0	0	0	2	0	7.12	0.49	5.19	0.29	1.49	0.30	97.8			
C42		2	0	1	1	1	0	0	2	3	3.92	0.50	1.51	0.73	-0.52	0.78	93.5	0.4	-0.75	1.77
C43		4	0	0	0	0	0	0	4	0	Heterogeneous						98.7	0.1		
C44		0	1	0	0	0	0	1	0	2	4.25	0.69	1.93	1.14	-0.28	1.24	97.8	2.1	-0.93	2.76
	Relict	2	0	2	0	0	0	0	2	2	-7.46	0.68	-10.28	0.81	-6.42	0.88	98.7			
C45		2	0	0	1	0	0	1	2	2	10.36	1.29	8.49	0.96	3.11	1.02	98.5	0.2	-2.09	2.57
C46		0	1	0	0	0	0	0	1	0	0.68	0.37	-2.08	0.36	-2.43	0.41	96.7	0.0	0.09	0.99
C47		1	4	0	0	0	0	0	3	2	-1.27	0.54	-3.48	0.80	-2.82	0.91	96.2	1.8	-1.00	2.04
	Relict	1	0	0	0	0	0	0	0	1	-16.06	0.95	-17.17	1.75	-8.82	2.04	96.3			
C48		2	2	0	0	0	0	0	2	2	11.39	0.71	9.46	0.89	3.53	1.02	98.3	0.3	-1.94	2.33
C49		2	0	0	0	0	0	1	1	2	8.46	0.52	5.55	0.58	1.07	0.63	99.1	0.1	0.38	1.48
C50		2	2	0	0	0	0	0	2	2	6.23	0.56	2.77	0.89	-0.46	1.02	98.7	0.2	1.44	2.27
C51		2	2	0	0	0	0	1	3	2	9.09	0.50	5.96	0.46	1.26	0.49	97.8	0.3	0.61	1.20
C52		3	2	0	0	0	0	0	3	2	8.84	0.80	6.02	0.80	1.44	0.91	98.4	0.5	-0.02	2.13
C53		1	2	0	0	0	0	0	2	1	0.70	0.62	-1.97	1.02	-2.36	1.18	97.5	0.4	-0.03	2.60
C54		2	2	0	0	0	0	1	2	3	7.52	0.74	4.94	0.69	0.96	0.49	98.7	0.3	-0.33	1.32
C55		2	2	0	0	0	0	0	1	3	1.67	0.59	-0.41	0.81	-1.29	0.88	97.4	0.1	-1.35	1.98
C56		0	2	0	0	0	0	0	0	2	-0.87	0.65	-3.85	1.07	-3.40	1.07	95.6	1.0	0.62	2.39
C57		0	3	0	0	0	0	0	0	3	7.53	0.62	4.41	1.02	0.49	1.18	97.6	0.4	0.69	2.61
C58		1	1	0	0	0	1	1	1	2	1.88	0.74	-1.14	1.06	-2.12	1.14	94.5	1.1	0.64	2.56
C59		2	0	0	0	0	0	1	0	3	8.50	0.53	4.41	0.58	-0.01	0.63	73.2	0.4		

[a] Number of spots analyzed on individual phases.

[b] Number of spots analyzed with 15 μm beam and 4 μm beam.

Table 2. Oxygen isotope ratios of olivine and pyroxene fragments in Asuka-881020.

Fragment	Phase	$\delta^{18}O \pm 2SD$ (‰)		$\delta^{17}O \pm 2SD$ (‰)		$\Delta^{17}O \pm 2SD$ (‰)		Mg#	$\Delta^{18}O_{PCM} \pm 2\sigma$ (‰)	
F41	Ol	6.59	0.29	4.75	0.66	1.33	0.68	98.6	-2.04	1.52
F42	Lpx	8.29	0.29	7.31	0.66	3.00	0.68	97.3	-3.91	1.53
F43	Ol	3.00	0.29	1.68	0.66	0.12	0.68	99.1	-3.03	1.51
F44	Ol	0.66	0.29	-1.73	0.66	-2.08	0.68	96.8	-0.67	1.50
F45	Ol	7.61	0.29	6.84	0.66	2.88	0.68	98.3	-4.34	1.53
F46	Lpx	4.18	0.17	2.24	0.63	0.06	0.65	99.3	-1.74	1.42
F47	Lpx	9.86	0.17	7.79	0.63	2.67	0.65	98.0	-1.63	1.45
F48	Lpx	3.82	0.17	1.05	0.63	-0.93	0.65	95.9	0.04	1.42
F49	Ol	4.52	0.44	1.95	0.37	-0.40	0.21	90.7	-0.41	0.69
F50	Lpx	-3.93	0.19	-6.64	0.38	-4.60	0.34	98.9	0.14	0.79
F51	Lpx	-2.86	0.19	-6.38	0.38	-4.89	0.34	98.8	1.84	0.79
F52	Ol	-3.71	0.82	-6.94	1.49	-5.02	1.51	96.3	1.25	3.35
F53	Ol	-3.16	0.82	-5.48	1.49	-3.83	1.51	96.7	-0.74	3.35
F54	Ol	5.56	0.17	4.83	0.63	1.94	0.65	64.0		
F56	Int. px	9.19	0.29	3.95	0.66	-0.83	0.68	80.0		
F57	Hpx	4.95	0.29	1.08	0.66	-1.49	0.68	50.5		
F58	Lpx	3.77	0.29	2.03	0.66	0.07	0.68	74.8		
F59	Ol	4.83	0.17	3.55	0.63	1.04	0.65	74.7		
F60	Ol	4.86	0.17	1.90	0.63	-0.62	0.65	75.7		
F61	Ol	11.75	0.30	9.27	0.52	3.16	0.42	68.0		

Table 3. Element compositions of Fe-particles in FIB sections of olivine phenocrysts (EDS-TEM, data in wt%)

	Fe	Ni
grid-1	97.7	2.3
	100.0	b.d.
	94.2	5.8
	100.0	b.d.
	96.3	3.6
	99.1	0.9
grid-2	95.4	4.6
Average		2.5
±1σ		2.3

b.d.: below detection limit.

1

Table 4. Element compositions of olivine and silica-rich glass in FIB sections of olivine phenocrysts (EDS-TEM, data in wt%)

		SiO_2	TiO_2	Al_2O_3	FeO	MnO	MgO	CaO	Na_2O	K_2O	Cr_2O_3
olivine	grid-1	40.34	b.d.	b.d.	b.d.	b.d.	59.66	b.d.	b.d.	b.d.	b.d.
	grid-2	42.22	b.d.	b.d.	1.30	b.d.	56.48	b.d.	b.d.	b.d.	b.d.
silica-rich glass	grid-1	58.24	b.d.	23.47	b.d.	b.d.	b.d.	18.29	b.d.	b.d.	b.d.
	grid-1	54.80	b.d.	25.36	b.d.	b.d.	b.d.	19.84	b.d.	b.d.	b.d.

b.d.: below detection limit.

2

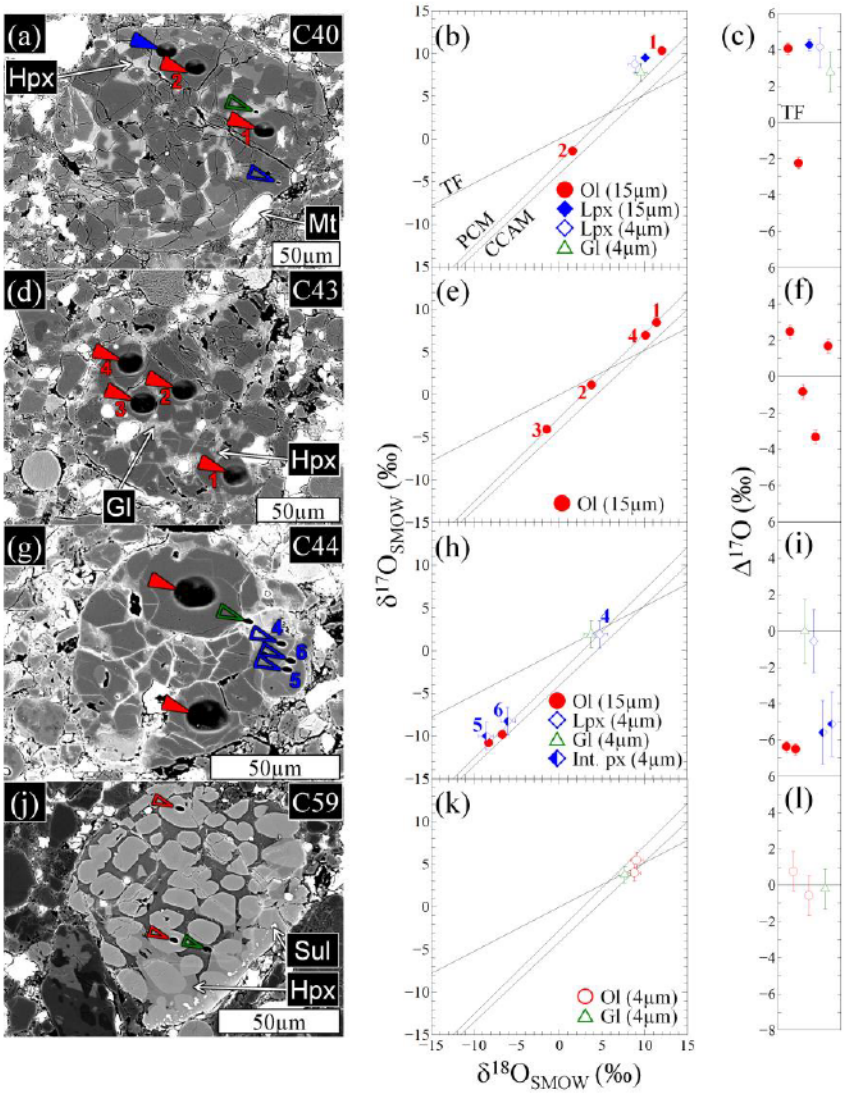

Fig. 1. BSE images after oxygen isotope analyses, oxygen three-isotope plots, and $\Delta^{17}O$ value plots of representative porphyritic chondrules in A-881020; (a, d, g, and j) BSE images of C40, C43, C44, and C59. Analysis points are shown by the vertex of a filled triangle for 15 μm spot and that of an open triangle for 4 μm spot. Colors of the symbols are the same as those of oxygen-three isotope plots. (b, e, h, and k) Oxygen three-isotope plots of data from C40, C43, C44, and C59. TF, PCM, and CCAM represent the terrestrial fractionation line, the Primitive Chondrule Mineral line, and the Carbonaceous Chondrite Anhydrous Mineral line. Numbers near the SIMS pits in the BSE images and those near the data points in the oxygen three-isotope plots indicate spot numbers of SIMS analysis, which correspond to spot numbers in Supplementary Table A4. (c, f, i, and l) The $\Delta^{17}O$ value of data from C40, C43, C44, and C59. Data are shown in ascending sequence. Symbols are the same as those in oxygen three-isotope plots. Abbreviations: Hpx, high-Ca pyroxene; Mt, Fe-Ni metal; Ol, olivine; Lpx, low-Ca pyroxene; Gl, glass; Int. px, intermediate pyroxene; Sul, Fe-sulfide.

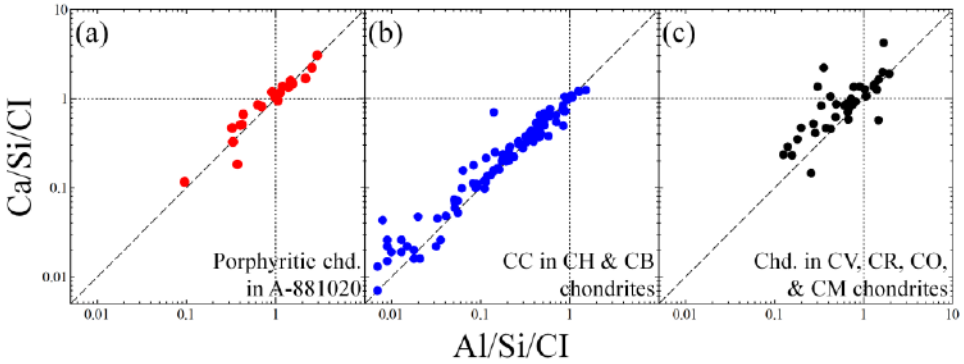

Fig. 2. Bulk refractory element compositions of chondrules normalized by Si and elemental abundance of CI chondrites (Anders and Grevesse, 1989) in a log scale; (a) porphyritic chondrules in A-881020, (b) CC chondrules and CC-like fragments in CH and CB chondrites (A-881020; Sayh al Uhaymir 290; Isheyevo; MacAlpine Hills 02675; Queen Alexandra Range 94627; Krot et al., 2010; Nakashima et al., 2011, 2020), and (c) chondrules in CV, CR, CO, and CM chondrites (Hezel and Palme, 2010).

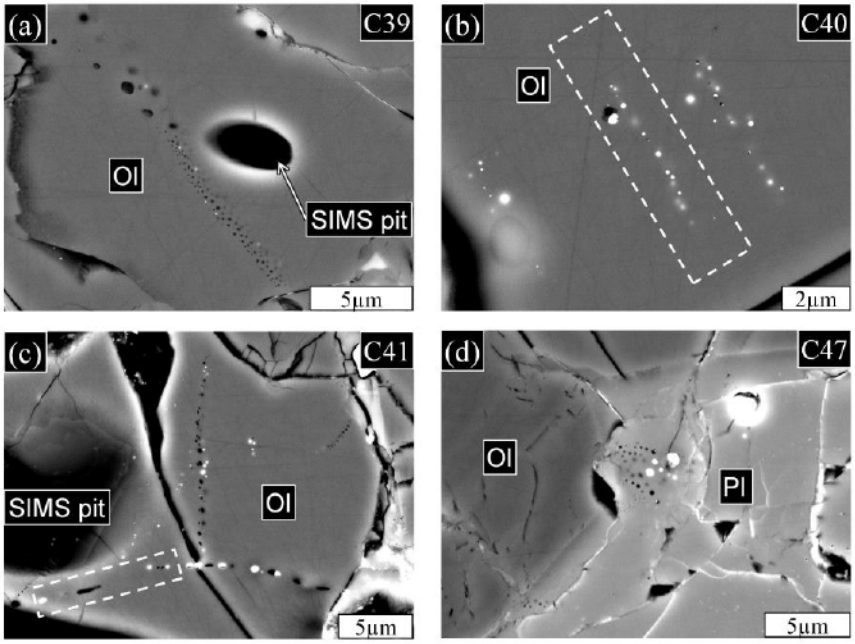

Fig. 3. BSE images of olivine phenocrysts and plagioclase with sub-μm sized Fe-particles and vesicles in porphyritic chondrules in A-881020; (a-c) olivine phenocrysts in C39, C40, and C41 and (d) plagioclase in C47. Rectangle areas surrounded by dashed lines in panels b and c were cut out using FIB for TEM observations. Abbreviations: Ol, olivine; Pl, plagioclase.

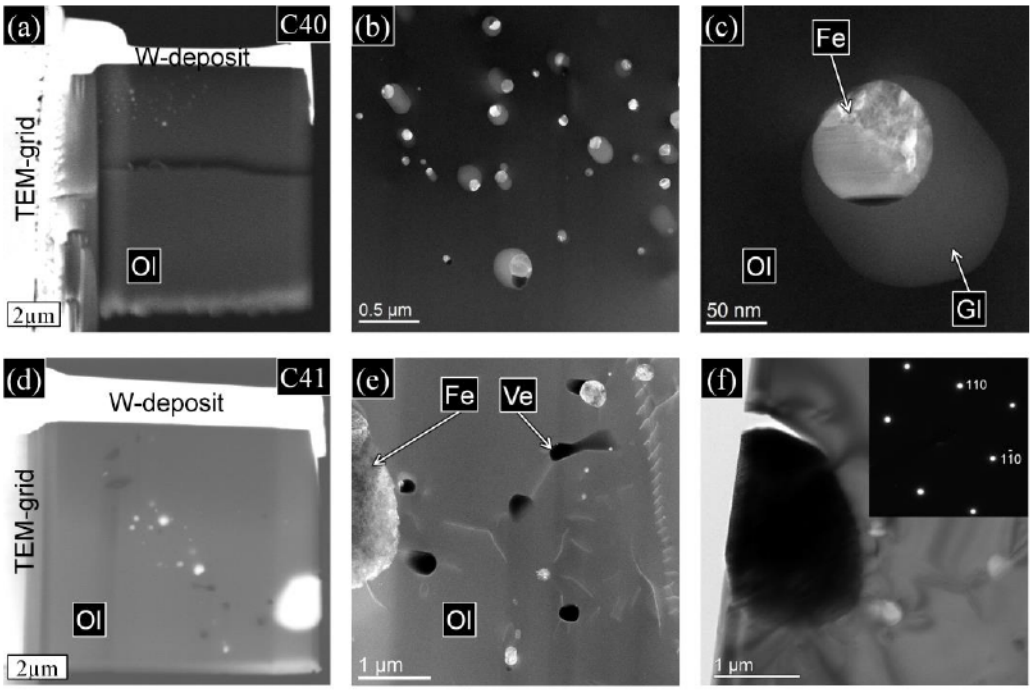

Fig. 4. Electron micrographs of the two FIB sections from olivine phenocrysts in C40 (grid-1) and C41 (grid-2); (a and d) BSE images of the two FIB sections of grid-1 and -2, (b and e) HAADF-STEM images of Fe-particles and vesicles in grid-1 and -2, (c) The Enlarged HAADF-STEM image showing Fe-particle with silica-rich glass in grid-1, and (f) The bright-field TEM image of the largest Fe-particle in grid-2 with the selected area electron diffraction pattern consistent with the bcc structure of kamacite. Fe-particles in grid-1 (panel b) are surrounded by silica-rich glass. Abbreviations: Ol, olivine; Fe, Fe-particle; Gl, glass; Ve, vesicle.

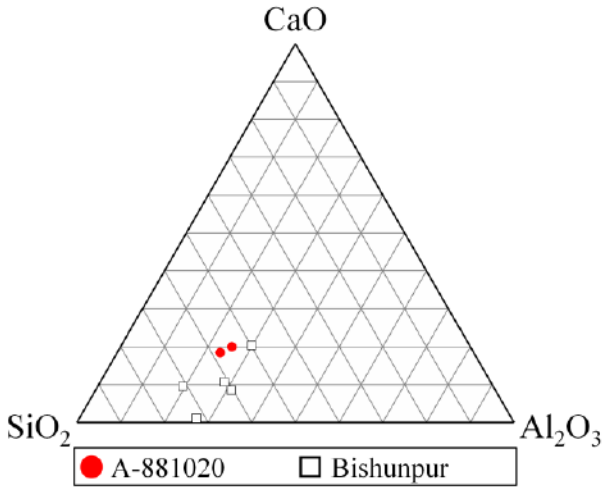

Fig. 5. Compositions of silica-rich glass in olivine phenocrysts in the C40 chondrule. Compositions of silica-rich glass in olivine phenocrysts in the Bishunpur (LL3.1) chondrules are shown for comparison (Leroux et al., 2003).

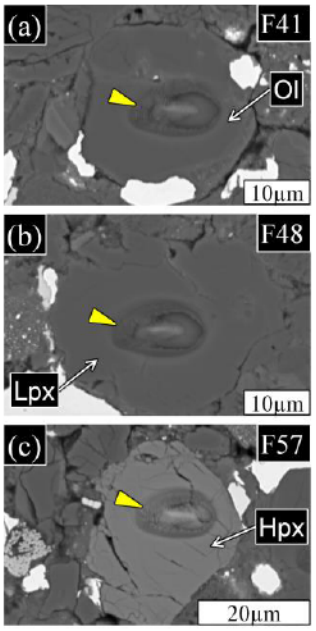

Fig. 6. BSE images of olivine and pyroxene fragments after oxygen isotope analyses; (a) F41, an olivine fragment, (b) F48, a low-Ca pyroxene fragment, and (c) F57, a high-Ca pyroxene fragment. Analysis points are shown by the vertex of a filled triangle for 15 μm spot. Abbreviations: Ol, olivine; Lpx, low-Ca pyroxene; Hpx, high-Ca pyroxene.

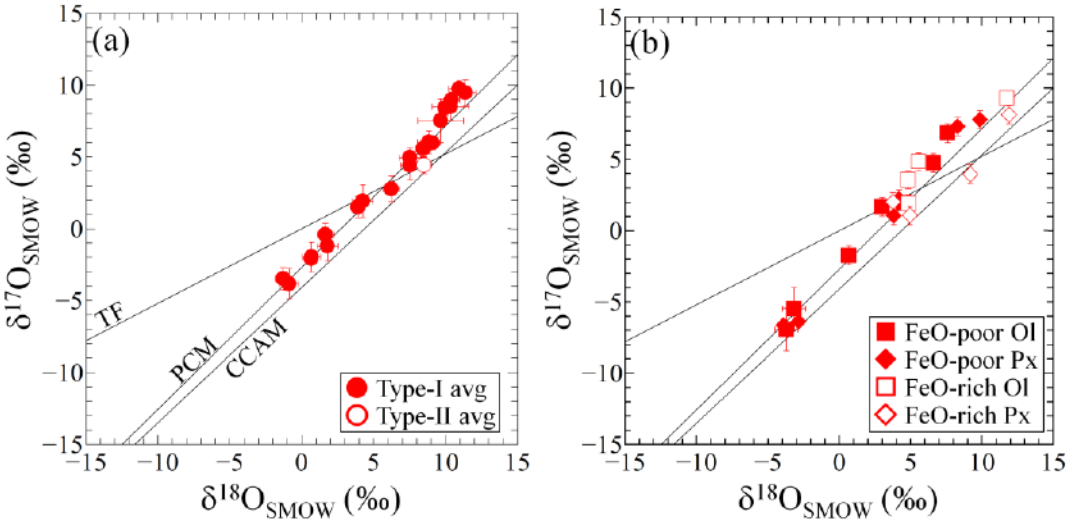

Fig. 7. Oxygen three-isotope ratios of porphyritic chondrules (a) and olivine and pyroxene fragments (b). In panel a, average oxygen isotope ratios of individual chondrules are plotted.

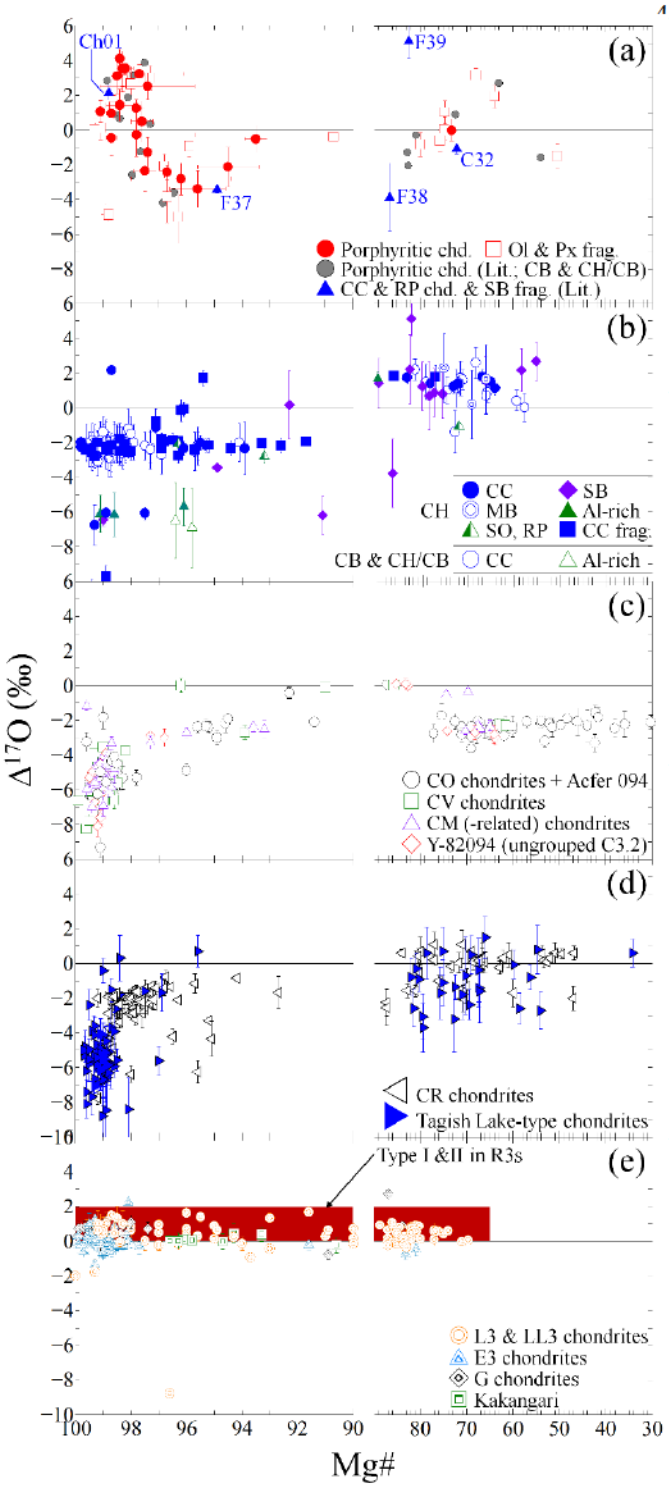

Fig. 8. Comparison between $\Delta^{17}O$ values and Mg# of the porphyritic chondrules and olivine and pyroxene fragments (a), non-porphyritic chondrules from CH and CB chondrites (b), chondrules from Acfer 094 (ungrouped C3.0), CO, CV, CM, CM-related, and Yamato-82094 (ungrouped C3.2) (c), chondrules from CR chondrites and Tagish Lake-type chondrites (d), and chondrules from L3, LL3, E3, G, Kakangari, and R3 chondrites (e). Literature data are from Krot et al. (2001, 2010, 2012, 2021), Connolly and Huss (2010), Kita et al. (2010, 2015), Russell et al. (2010), Nakashima et al. (2011, 2020), Weisberg et al. (2011, 2015, 2021), Ushikubo et al. (2012), Schrader et al. (2013, 2014, 2017), Tenner et al. (2013, 2015, 2017), Nagashima et al. (2015), Chaumard et al. (2018, 2021), Hertwig et al. (2018, 2019a, 2019b), Marrocchi et al. (2018, 2019, 2021, 2022), Yamanobe et al. (2018), Piralla et al. (2021), Siron et al. (2021, 2022), Ushikubo and Kimura (2021), Fukuda et al. (2022), and Pinto et al. (2024). Abbreviations: CC, cryptocrystalline; SB, silica-bearing; MB, Fe-Ni metal-bearing; SO, skeletal olivine; RP, radial pyroxene. CH, CH/CB, and CB chondrites used in the plots are Acfer 182, Acfer 214, A-881020, Sayh al Uhaymir 290, Isheyevo, MacAlpine Hills 02675, and Queen Alexandra Range 94627.

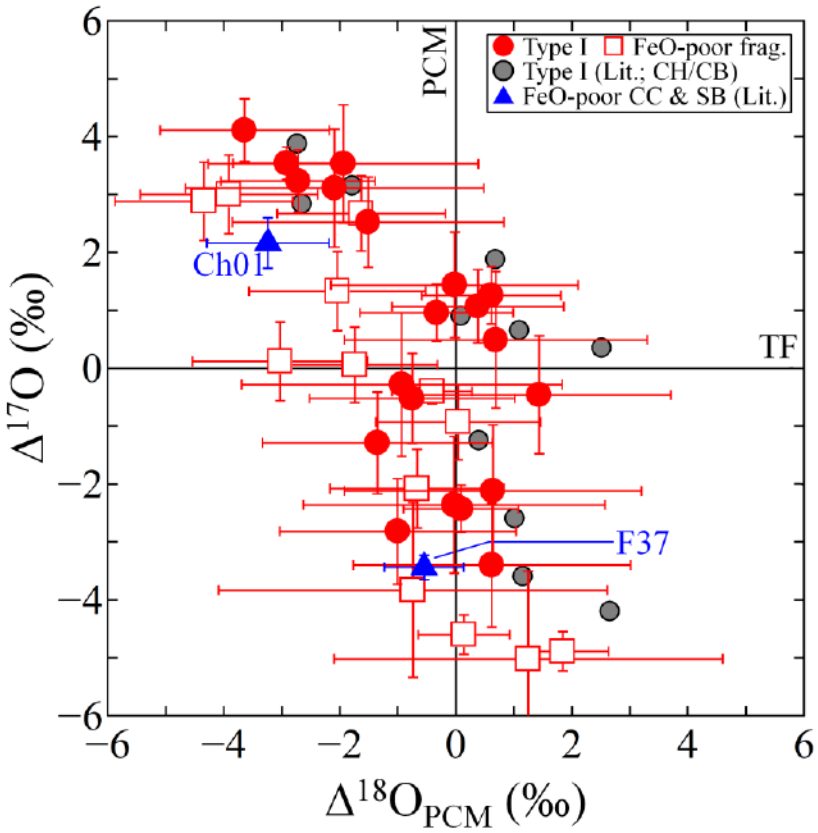

Fig. 9. Comparison between $\Delta^{17}O$ values and the deviation of $\delta^{18}O$ values from the PCM line ($\Delta^{18}O_{PCM}$) for the type I chondrules and FeO-poor olivine and pyroxene fragments in CH and CB chondrites. Literature data of the type I chondrules are from Krot et al. (2010), and those of the CC chondrule and silica-bearing (SB) fragments are from Nakashima et al. (2011, 2020). CH and CH/CB chondrites used in the plot are A-881020, Sayh al Uhaymir 290, and Isheyevo.

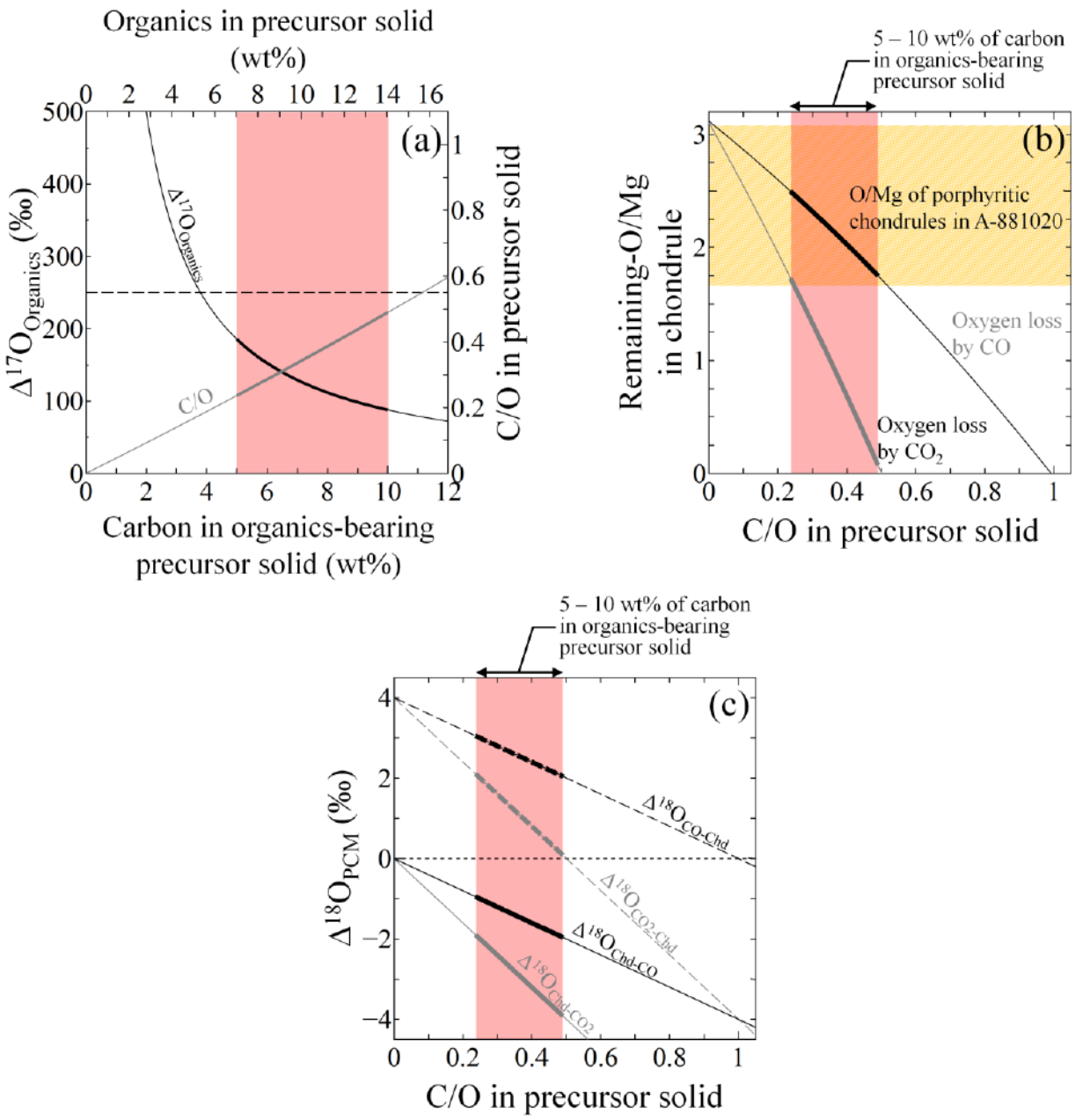

Fig. 10. $\Delta^{17}O$ value of carbon-rich organics with variable concentrations in chondrule precursor solid (a), Remaining-O/Mg ratio in chondrules as a function of C/O atomic ratio in precursor solid (b), and $\Delta^{18}O_{PCM}$ value as a function of C/O atomic ratio in precursor solid (c). The elemental composition of organics is assumed to be ~ $C_{100}H_{75}O_{17.5}N_{3.5}S_{2.5}$ (chondritic IOM; Alexander et al., 2017). Red shaded areas in the three panels are the ranges of carbon in organic-bearing precursor solid (5 – 10 wt%). The bold lines in the three panels represent the $\Delta^{17}O_{Organics}$ range, ranges of Remaining-O/Mg ratios, and $\Delta^{18}O_{PCM}$ ranges in case of 5 – 10 wt% of carbon. The horizontal dashed line in panel a represents the upper limit of $\Delta^{17}O$ values of IOMs from a CR chondrite (Hashizume et al., 2011). The orange shaded area in panel b represents the range of O/Mg ratios of the bulk porphyritic chondrules in A-881020 obtained by defocused EPMA analyses (Supplementary Table A1).

Declaration of interests

☒ The authors declare that they have no known competing financial interests or personal relationships that could have appeared to influence the work reported in this paper.

☐The authors declare the following financial interests/personal relationships which may be considered as potential competing interests:

GCA Submission Checklist

Please complete this checklist by entering an "X" for each entry once you have verified that your manuscript complies with the requirement. In some cases, the requirement may not be applicable and "NA" should instead be entered. Please upload this form in Editorial Manager when you submit your manuscript. Before completing this checklist, please review the Guide for Authors: https://www.elsevier.com/journals/geochimica-et-cosmochimica-acta/0016-7037/guide-for-authors

X The title summarizes the major scientific finding of the study rather than the study location or the methods used.

X The manuscript lists only one corresponding author.

x The first page of the manuscripts lists the names and affiliations of all authors. Affiliations are needed for identifying conflicts of interests in the review process. ***Note that manuscripts lacking author affiliation information on the first page will be returned without review.***

X The abstract is less than 500 words in length and formatted as 1 to 2 paragraphs.

x Citation of references in the abstract have been avoided to the extent possible.

x Acronyms/abbreviations have only been defined in the abstract if the term appears three or more times.

X Three or more keywords have been provided. ***Do not provide Highlights or Graphical Abstracts, these are not part of GCA format.***

X The introduction is a single section without subsections and avoids excessive review.

X The manuscript contains separate Results and Discussion sections. If this is not possible, then a request and justification for combined Results and Discussion sections have been added to the Cover Letter.

X The Discussion section (or a subsection) addresses the broader geochemical and/or cosmochemical significance and implications of the study.

X The Acknowledgments identifies the source(s) of funding that supported the study.

X *(Required only if the paper involves meteorite samples)* Meteorite nomenclature uses the approved list of names in the Meteoritical Bulletin Database and new meteorite names have been submitted for consideration by the Meteorite Nomenclature Committee.

X Acronyms/abbreviations are defined at first use in the main text. Note that the abstract is considered a separate document and all acronyms/abbreviations used in the main text must be defined in the main text.

X Equations have been submitted as editable text and not as images.

X All tables intended for publication in the main paper have been provided in a format generated using Microsoft Word, LaTeX, or similar document preparation software. ***Tables are not accepted in XLSX format and cannot contain shading or color.***

X All numbers in tables appear in decimal format (e.g., 2.873), scientific notation (e.g., 4.76×10^{-5}), or a related format. Excel-style scientific notation (e.g., 8.54E-03) is not an acceptable format.

X All figures comply with the Artwork requirements listed in the Guide for Authors.

x Maps providing geographical context for the study are based on physical geographic features and do not display national borders or other political boundaries.

x If one or more Supplementary Material files are included in the submission, a section titled "Appendix A. Supplementary Material" is inserted between the Acknowledgements and References and briefly describes the contents of all supplementary files. This text should explain to readers the information that they can find in the supplementary file(s). This should be written in paragraph format.

x Supplementary figures and their captions are embedded in a single PDF document rather than uploaded as a series of separate image or PDF files.

x Supplementary files have been combined into a single PDF document to the extent possible. This file includes a cover page indicating the article title and authors. ***Note that DOCX files are not accepted as supplements; these must be converted to PDF before submission.***

x *(Required if manuscript was prepared in Microsoft Word or similar software)* The References are in current GCA format, which includes:

- x Article titles are written in sentence case, not title case, and use correct formatting, such as subscripts in chemical formula.
- x Journal titles are abbreviated (e.g., Geochim. Cosmochim. Acta).
- x No web links are included for journal articles.
- x DOIs are used only when volume and page/article numbers are unavailable.

_____ *(Required if manuscript was prepared in LaTeX)* The manuscript was prepared using the Elsevier article class in combination with BibTeX (use elsarticle-harv.bst), as described at: https://www.elsevier.com/authors/policies-and-guidelines/latex-instructions

x Citation of conference abstracts has been avoided to the extent possible. Each citation of a conference abstract includes an individual justification in the Cover Letter and complies with the policies outlined in the Guide for Authors.

x Papers in preparation are not cited. Papers in review are either not cited or a full copy of the cited work is provided as Review-Only Material.

x The data underlying all figures in the main paper and any supplementary material have been made available in a text-based numerical format via deposition in an open-access repository. A section entitled "Data Availability" has added followed by a sentence indicating the repository and the URL for the data. An example of this section might appear as follows:

Data Availability
Data are available through Mendeley Data at https://doi.org/10.17632/cfdzx2rh8z.1.

All data appearing as a point, line, or bar plot, including spectra, diffraction patterns, and chromatograms, must be provided. All data appearing in the manuscript and any supplementary documents, figures, or tables must be made available upon submission. Images, maps, movies, and similar large datasets are excluded from this requirement. Consult the Data Availability section of the Guide for Authors for more details on complying with this requirement. Note that failure to comply with this requirement will result in the manuscript being returned without review.